

PHYSIK DEPARTMENT



IDENTIFICATION OF MUON-INDUCED SIGNALS IN THE
DEEP UNDERGROUND
NEUTRINO-SCINTILLATION-DETECTOR
BOREXINO

DISSERTATION

MAY 2005
CHRISTIAN LENDVAI



TECHNISCHE UNIVERSITÄT
MÜNCHEN

Technische Universität München
Physik Department
Lehrstuhl für Experimentalphysik-Astroteilchenphysik E15
Univ.-Prof. Dr. Franz von Feilitzsch

IDENTIFICATION OF MUON-INDUCED SIGNALS IN THE
DEEP UNDERGROUND
NEUTRINO-SCINTILLATION-DETECTOR
BOREXINO

CHRISTIAN LENDVAI

Vollständiger Abdruck der von der Fakultät für Physik der Technischen Universität München zur Erlangung des akademischen Grades eines

Doktors der Naturwissenschaften (Dr. rer. nat.)

genehmigten Dissertation.

Vorsitzender: Univ.-Prof. Dr. Andrzej J. Buras

Prüfer der Dissertation: 1. Univ.-Prof. Dr. Franz von Feilitzsch

2. Univ.-Prof. Dr. Klaus Schreckenbach

Die Dissertation wurde am 21.06.2005 bei der Technischen Universität München eingereicht und durch die Fakultät für Physik am 06.07.2005 angenommen.

Abstract

In the last decade convincing evidence for neutrinos with finite rest mass has been found. If neutrinos are massive the weak and mass eigenstates are not necessarily identical, which would allow a mixing matrix in the leptonic sector, similar to the one in the quark sector. This phenomenon of neutrino oscillations is a kind of flavor oscillation, which is already known in other particle systems. Currently we have three evidences for neutrino oscillations coming from accelerators, the atmosphere and the Sun. The Sun, reliably described by the "Solar Standard Model" is a very interesting source of neutrinos, since a measurable lack of neutrinos from the Sun was the main argument for non-vanishing neutrino masses. Several experiments were dedicated to the detection of solar neutrinos out of which Borexino is a real time detector for the low energy part of the solar neutrino flux. This work was accomplished in the frame of the Borexino experiment and aimed the setup of a water Cherenkov detector for the suppression of cosmogenic induced background.

Chapter 1 will give a brief introduction to neutrino physics. After a passage through the history from its original postulation by Pauli to the current experimental status of neutrino physics, the solar neutrino puzzle and the experiments dedicated to solar neutrino measurements are reviewed. The theoretical framework of neutrino oscillations will be explained, and finally a summary of the most interesting open questions and the purpose of future neutrino experiments, is given.

In the following Chapter 2, the solar neutrino experiment Borexino and its scientific program is presented. Borexino will perform real time spectroscopy of low energy neutrinos from the sun, but is also capable to detect supernova- and geo-neutrinos as well as reactor neutrinos. In order to manage this am-

bitious goals the intrinsic radioactive and the cosmogenic background should be significantly suppressed. In order to test the scintillator purity and to demonstrate functionality of detector hardware, a Borexino prototype, the counting test facility (CTF) was used.

In Chapter 3 cosmic rays are briefly discussed. Apart from atmospheric neutrinos, muons are the only remnants of cosmic ray showers which penetrate in detectors positioned deep underground. Since their passage through the detector target can mimic the signal of a neutrino event, the suppression of these particles must play an important role for the development of low background experiments. Furthermore the muon induced background in liquid scintillator is discussed and results from the last CTF measurement campaign are presented.

Chapter 4, deals with the steps of designing a water Cherenkov detector for the detection of cosmogenic muons. First Monte Carlo simulation results are presented and improvement of the detector in the direction of muon tracking are discussed. In the end a possible scenario for the suppression of muon induced background and the consequences for the power of Borexino in measuring pep-, CNO-neutrinos is discussed.

In Chapter 5 the main topic of this work, which was the development, test and installation of the outer water Cherenkov detector for the Borexino experiments is elucidated. From photomultiplier encapsulation to LED calibration all important aspects for the realization of a reliable and precise detection setup are summarized. The presentation of the installation and the testing of the detectors hardware and software concludes this chapter.

In Chapter 6, it is shown how the future LENA (**L**ow **E**nergy **N**eutrino **A**stronomy) detector will bring neutrino physics from merely studying neutrinos to using neutrinos as probes to solve questions in astrophysics, cosmology, geophysics and elementary particle physics.

Contents

1	Neutrino Physics and Experiments	1
1.1	From Neutrino Postulate to Neutrino Detection	2
1.2	Solar Neutrino Experiments and Neutrino Oscillations	4
1.2.1	Evidence for solar neutrino deficit	7
1.2.2	Vacuum and Matter Oscillation	12
1.3	Results of Neutrino Oscillation Experiments	17
1.4	Open Questions in Neutrino Physics and Future Neutrino Experiments	20
2	The Solar Neutrino Experiment BOREXINO	25
2.1	Motivation and Detector Design	26
2.2	Borexino after SNO and Kamland	27
2.3	Background	30
2.3.1	Schematic of the Borexino read out electronics and trigger system	32
2.4	The Counting Test Facility (CTF)	34
2.5	Status of the Detector	36
3	Muons and Muon Induced Background in Borexino	37
3.1	Muons induced by Cosmic Rays in the Atmosphere	38
3.2	Muons in Underground Experiments	41
3.3	Cosmogenic Background in Borexino and CTF	44
3.3.1	Measurement of the Muon Induced Background in the CTF III	48

CONTENTS

4	Design and Simulation of a Muon Veto for Borexino	55
4.1	Design Studies for the Outer Detector	56
4.1.1	Improvement of the Positioning	60
4.2	Muon Track Reconstruction Study	63
4.2.1	Muon Tracking Method	64
5	Achievement of the Borexino Muon Veto	67
5.1	The PMTs and the PMT's encapsulation	68
5.1.1	Motivation for a PMT Encapsulation	69
5.1.2	Design	70
5.1.3	Testing	74
5.2	Schematic of the Muon Veto Electronics and DAQ	77
5.2.1	Decoupling the Fast PM Pulse	77
5.2.2	Charge to Time Converters (QTC)	78
5.2.3	The Muon veto Trigger Board (MTB)	81
5.3	Dark Noise Measurement	82
5.3.1	Requirements	83
5.3.2	Dark Noise Scalers	84
5.4	The LED Calibration System	87
5.4.1	Motivation	88
5.4.2	The LED Electronic	89
5.4.3	The Control Software	90
5.5	The Installation of the Outer Detector	93
5.5.1	Pre-installation	94
5.5.2	PMT Installation	94
5.5.3	Tyvek Installation	95
5.5.4	Monitor System	100
5.5.5	Test Run	101
6	Outlook	103
7	Conclusion	107

Chapter 1

Neutrino Physics and Experiments

In 1930 Wolfgang Pauli proposed a solution to the missing energy in nuclear beta decays, namely that it was carried by a light, neutral, spin-1/2 particle he at first called "neutron" [PAU 78]. James Chadwick's discovery in 1932 of the heavy fermion that he also called neutron could explain the behavior of the nitrogen nucleus like a boson [CHA 32]. Enrico Fermi in 1933 named the particle the "neutrino" (italian for little neutron) and formulated his famous theory for calculating the simultaneous emission of an electron with a neutrino [FER 34]. Shortly thereafter, Hans Bethe and Rudolf Peierls used Fermi's theory to show that the interaction of neutrinos with matter was such that the neutrinos could penetrate several light years depth of ordinary matter before they would be stopped (i.e. $\sigma < 10^{-44} \text{cm}^2$ for a 2.3 MeV neutrino beam) [BET 34]. They concluded that "there is no practically possible way of observing the neutrino". Although Pauli's stunned remark "I have postulated a particle that cannot be detected" [PAU 30], the idea of the neutrino was born and it remained mostly an intriguing idea for years.

1.1 From Neutrino Postulate to Neutrino Detection

The situation changed when Fermi and collaborators successfully achieved chain nuclear reactions in 1942. The fact that nuclear reactors were expected to produce neutrino fluxes on the order of $10^{12} - 10^{13}$ neutrinos per second per cm^2 , which is far higher than any attainable flux from radioactive sources was used in an experiment in the mid 1950's by Frederick Reines and Clyde L. Cowan, Jr. in order to verify the existence of the neutrino [REI 57],[REI 60],[REI 95]. Their detector consisted of three large tanks of organic scintillator (discovered in 1947 by Broser and Kallmann [BRO 47]), and was located 12 m underground, permitting much better rejection of cosmic-ray backgrounds, and 11 m away from the Savannah River reactor. Each scintillator tank was seen by 110 photomultiplier tubes (PMT). Cadmium was loaded as a neutron absorber. The target was hydrogen in the scintillator. They used a delayed coincidence technique, identifying the reaction $\bar{\nu} + p \rightarrow e^+ + n$ by the promptly following signal of $e^+e^- \rightarrow \gamma\gamma$ and the delayed signal of gamma rays from a neutron absorbed in cadmium. In 1956 Reines and Cowan observed 3.0 ± 0.2 events per hour with the reactor operating, which was much greater than the background due to cosmic rays or accidental coincidences. Since the experiment using ^{37}Cl , which was pursued by Davis (1955) and which was not sensitive to $\bar{\nu}$ (if $\nu \neq \bar{\nu}$) failed to observe $^{37}\text{Cl} \rightarrow ^{37}\text{Ar}$ conversion, it was understood that ν and $\bar{\nu}$ are different particles.

During 1956-58, Goldhaber, Grodzins, and Sunyar performed an experiment at Brookhaven National Laboratory which showed conclusively that the neutrino is created with negative helicity [GOL 58]. The conclusion of this information was that the neutrino is always left-handed, as Lee and Yang had suggested [LEE 57]. Thus the constraint that ν and $\bar{\nu}$ are different particles had to be relaxed, since they could be one and the same particle with different helicities (i.e. Majorana particle).

With increasing activity at accelerators and the construction of more powerful accelerators high energy beams of protons were available. The Alternating Gradient Synchrotron at Brookhaven was one of these accelerators. Schwartz and his colleagues built a 10 ton spark chamber from aluminum

1.1 From Neutrino Postulate to Neutrino Detection

plates in order to detect the neutrinos with energies ranging from hundreds of MeV to several GeV produced in pion or kaon decays [SCH 89]. These neutrinos had interaction cross sections more than a hundred times greater than reactor-born neutrinos. Since the tandem neutrinos were detected through interactions where muons but not electrons were produced they were different from the neutrinos produced in β -decays. Particle physicists began calling them "muon neutrinos" to distinguish them from "electron neutrinos". There were now four distinct "leptons", or light particles: the electron, the muon and their two respective neutrinos (plus antiparticles).

By the discovery of neutral currents in 1973, by an international collaboration at CERN [PER 97], it became evident that neutrinos and all other leptons and quarks were capable of a new kind of weak interaction in which they maintained their identity instead of transforming into a partner lepton (or quark), by exchanging a neutral boson " Z^0 ". At that time the standard model of particle physics is developed. In 1972 Kobayashi and Maskawa extended the four-quark theory into a model with six quarks plus another charged lepton and his neutrino so that the CP violation phenomenon could be explained [KOB 73]. The new lepton τ was pair-produced in high-energy electron-positron collision at the SLAC-LBL detector by Perl and his colleagues in 1975 [PER 75]. It took more than two decades until the direct observation of the τ neutrino, the last piece to the standard model, at the DONUT experiment at Fermilab, where τ -decays of heavy charmed hadrons were studied [KOD 00].

Precise measurement of the properties of the Z^0 -boson the heavy, neutral partner of the W-boson and the photon during the late 1980s in experiments at new electron-positron colliders - the SLC at SLAC and LEP at CERN - have shown the evidence that the Standard Model of the electro-weak interactions (SM) works extremely well, up to energies of several hundred GeV. One of these measurements is associated with the "invisible Z-boson width" from the process $e^-e^+ \rightarrow \nu\bar{\nu}$. This width of the Z-boson decay into neutrino-antineutrino pairs $\Gamma_{\nu\bar{\nu}}$ is given by:

$$\Gamma_{\nu\bar{\nu}} = \frac{1}{12\pi} \frac{G_F}{\sqrt{2}} M_Z^3 N_\nu \quad (1.1)$$

G_F : Fermi coupling constant

1 Neutrino Physics and Experiments

M_Z : Z Mass

N_ν : Number of left-handed neutrinos

Assuming that the SM is correct, the measurement of $\Gamma_{\nu\bar{\nu}}$ can be translated into a count of the number of neutrino species [HAG 02].

$$N_\nu = 2.9841 \pm 0.0083 \quad (1.2)$$

This value is valid for neutrino masses $m_\nu < 45$ GeV and is close to the expected number of 3 from the SM, though it is two sigma low. This can be interpreted as evidence that the SM contains three and only three families of fermionic fields, meaning that there is no fourth sequential generation. If a fourth neutrino flavor would exist within this mass range it must not couple to the Z^0 -boson and to weak interaction in general. It would be a "sterile" neutrino. It is remarkable that this result is in agreement with cosmological constraints on the number of relativistic species around the time of Big Bang nucleosynthesis, which seem to indicate the existence of three very light neutrino species [BAR 03-3].

1.2 Solar Neutrino Experiments and Neutrino Oscillations

75 years after Pauli's neutrino postulate and half a century after its discovery, neutrinos still play a central role in elementary particle physics. Many questions about the role of neutrinos in astrophysics and cosmology have been solved by the resolution of the solar neutrino puzzle.

The Sun is the only hydrogen-burning star which produces neutrinos detectable on earth. Their detection is the signature that weak interaction exists in the sun. Solar models trace the evolution of the sun over the past 4.7 billion years of main-sequence burning. They predict the present temperature and composition profiles of the solar core that is mainly responsible for the neutrino production. The standard solar models (SSMs) share four basic assumptions [HAX 05]:

1.2 Solar Neutrino Experiments and Neutrino Oscillations

- The dynamical time scale of the Sun is approximately one hour, hence, during its 4.5 billion years evolution it has had enough time to establish hydrostatic equilibrium. For any volume element within the Sun the weight of the element is assumed to be exactly balanced by the sum of all pressure forces acting on the element;
- The relation between the temperature gradient and the power flux of photons is described by the radiative transport equation. While the solar envelope is convective, radiative transport dominates in the core region where thermonuclear reactions take place. The opacity depends sensitively on the solar composition, particularly the abundances of heavier elements;
- The nuclear reaction chains, which are responsible for the generation of solar energy, include the hydrogen to helium burning reactions. The standard model predicts that over 98% of this energy is produced from the pp chain conversion of four protons into ${}^4\text{He}$ (see fig. 1.1). The proton burning through the CNO-cycle, whereby ${}^{12}\text{C}$ acts like a catalyst, counts for the remaining 2% [BAH 01]. Other reactions such as helium burning are not important for the Sun;
- The model is constrained to produce today's solar radius, mass, and luminosity. An important assumption of the standard model is that the Sun was highly convective, and therefore uniform in composition, when it first entered the main sequence. It is furthermore assumed that the surface abundances of metals (nuclei with $A \geq 5$) were undisturbed by the subsequent evolution, and thus provide a record of the initial solar metallicity;

The nuclear cross sections together with other solar model parameters (e.g., abundances, the solar age), can be incorporated into solar model calculations, leading to predictions that can be verified in helioseismology or neutrino flux measurements. Table 1.1 shows the neutrino fluxes from the different solar source reactions taking into account the results from the recent cross section measurement of the ${}^{14}\text{N}(p; \gamma){}^{15}\text{O}$ reaction [LUN 04].

Fig. 1.2 shows the solar neutrino spectrum on earth, which contains mono-energetic lines from the ${}^7\text{Be}$ - and pep-neutrinos and continuous spectra from pp-, ${}^8\text{B}$ - and hep-neutrinos from the pp-chain as well as additional

1 Neutrino Physics and Experiments

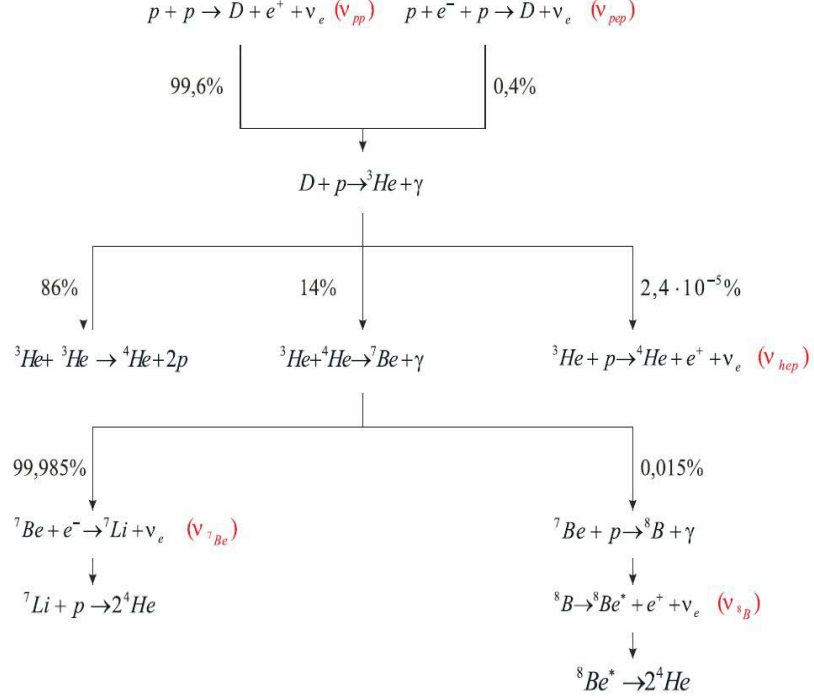


Figure 1.1: The ppchain, showing the four terminations: pp-I, pp-II, pp-III, pp-IV.

Source	BP04 ($cm^{-2}s^{-1}$)
pp	5.99 E10
pep	1.42 E8
hep	8.04 E3
${}^7\text{Be}$	4.65 E9
${}^8\text{B}$	5.26 E6
${}^{13}\text{N}$	4.06 E8
${}^{15}\text{O}$	3.54 E8
${}^{17}\text{F}$	3.97 E6

Table 1.1: Recent SSM prediction for solar neutrinos from different source reactions.[BAH 04]

1.2 Solar Neutrino Experiments and Neutrino Oscillations

continuous contributions of ^{13}N -, ^{15}O - and ^{17}F -neutrinos from the CNO-cycle.

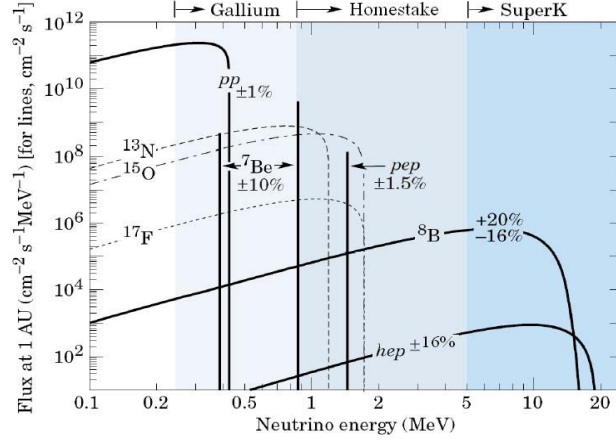


Figure 1.2: The solar neutrino spectrum at the earth, as predicted by the standard solar model. The pp-chain components are plotted with solid lines, the CNO contributions in dotted lines. The energy thresholds for the Gallium and Homestake experiments as well as the Super-Kamiokande detector are shown in the top part of the diagram [HAG 02].

1.2.1 Evidence for solar neutrino deficit

Ray Davis and his colleagues were guided by the interest in directly probing the thermonuclear reactions occurring in the solar core when they decided to run the pioneering chlorine solar neutrino experiment [DAV 68]. This radiochemical detector, which was sited nearly a mile underground in the Homestake mine in South Dakota, in order to avoid cosmic ray-induced backgrounds, operated almost continuously from its construction in 1967 until 2002. The detection reaction, which has been first suggested by Pontecorvo and Alvarez is

$$^{37}\text{Cl}(\nu_e, e^-)^{37}\text{Ar}, \quad E_{\text{threshold}} = 0.814 \text{ MeV} \quad (1.3)$$

The technique is based on the collection of the gaseous product ^{37}Ar with a half life of 35 days from a tank containing 0.61 kiloton of perchloroethylene

1 Neutrino Physics and Experiments

(C_2Cl_4). The Argon atoms produced within a run of 60 - 70 days were extracted and counted with proportional counters. The resulting efficiency for collecting the ^{37}Ar was high, typically greater than 95%. Davis radiochemical experiment determined a solar neutrino production rate of ~ 0.5 ^{37}Ar atoms/day in the tank. The final results for the experiment achieved an impressive accuracy, 2.56 ± 0.16 (stat) ± 0.16 (syst) SNU, where a Solar Neutrino Unit (SNU) is 10^{-36} captures/atom/s [CLE 98]. The Homestake experiment is primarily sensitive to (see fig. 1.2) 8B neutrinos ($\sim 76\%$), which can induce the strong superallowed transition to the 4.99 MeV state in ^{37}Ar , whereby 7Be neutrinos ($\sim 16\%$) are sufficiently energetic to overcome the 0.814 MeV threshold of the groundstate transition.

The discrepancy between the Homestake results and the SSM predictions (8.5 ± 1.8 SNU for BP04) was the genesis of the solar neutrino problem and lead to an extensive research program in the field of solar neutrinos and to the construction of bigger and more sensitive detectors [DAV 96].

SAGE and GALLEX are two similar radiochemical experiments, which began solar neutrino measurements in January 1990 and May 1991, respectively [GAV 89],[ABD 99], [ANS 92],[HAM 98],[HAM 96]. These experiments exploited the reaction $^{71}Ga(\nu_e, e^-)^{71}Ge$ which is primarily sensitive to the low-energy pp-neutrinos, because of the strength and low Q-value for the groundstate transition. The SAGE experiment, which is placed under 4700 mwe in the Baksan Neutrino Observatory and utilizes 60 tons of liquid Ga metal, continues to operate. GALLEX and its successor GNO, which used 30.3 tons of Ga as $GaCl_3$ in a hydrochloric acid solution, operated until ~ 2002 in the Gran Sasso Laboratory in Italy. In both experiments the Ge is extracted about every three weeks, concentrated, purified and finally converted into GeH_4 . Subsequently the GeH_4 is inserted into miniaturized gas proportional counters and the ^{71}Ge is counted by counting its decays back to ^{71}Ga ($\tau_{1/2} = 11.43$ d). The only signal is the energy deposited by Auger electrons and X-rays that accompany atomic rearrangement in Ga. Both K and L captures can be detected. Intense ^{51}Cr neutrino sources were used to calibrate both detectors [KIR 03].

The most recent results of SAGE give a counting rate of 66.9 ± 3.9 (stat) ~ 3.6 (syst) SNU [GAV 03], while the GALLEX/GNO result is 69.3 ± 4.1 (stat) ± 3.6 (syst) SNU [KIR 03]. The rates are in good agreement, but well below the SSM prediction of 131 ± 11 SNU [BAH 04]).

1.2 Solar Neutrino Experiments and Neutrino Oscillations

Unlike the radiochemical experiments, which can only provide an integrated neutrino detection over a period of time, two types of direct-counting experiments have been accomplished, the water Cerenkov detectors Kamiokande and its 11-times bigger successor SuperKamiokande and the heavy-water detector SNO (Sudbury Neutrino Observatory).

In Kamiokande [KOS 92] and Super-Kamiokande respectively the solar neutrinos scatter off electrons. The recoiling electrons produce Cherenkov radiation, which is then recorded in surrounding photomultipliers (PMs). Not only ν_e but also the other neutrino flavors contribute with $\sigma(\nu)_e/\sigma(\nu)_{other} \sim 7$ to the reaction:

$$\nu_x + e \rightarrow \nu'_x + e' \quad (1.4)$$

The detector is sitting a kilometer underground in a Japanese zinc mine. Kamiokande had an inner fiducial volume of 0.68 ktons. The threshold of the Kamiokande detector was initially 9.5 MeV but was ultimately lowered to 7 MeV, due to Kamiokande III improvements in electronics and the addition of wavelength shifters to improve PMT light collection. With its high PMT coverage (40%), lower threshold (~ 5 MeV), and much larger fiducial volume (22.5 ktons), SuperKamiokande collected data at a rate ~ 100 times faster than that of its predecessor, Kamiokande. SuperKamiokande had a phototube accident and is running now with about half of the original number of PMs.

Kamiokande found a 8B neutrino flux of $(2.91 \pm 0.08 \pm 0.33) \times 10^6/cm^2s$ [FUK 96], 48% of the BP04 SSM prediction of $(5.79 \pm 1.33) \times 10^6/cm^2s$.

SuperKamiokandes 8B neutrino flux result is $(2.35 \pm 0.02(stat.) \pm 0.08(sys.)) \times 10^6/cm^2s$ [FUK 02], $40.6 \pm 0.4(stat.) \pm {}^{+1.4}_{-1.3}(sys.)\%$ of the BP04 prediction.

These experiments were remarkable in several respects. They were the first to measure solar neutrinos in real time. They exploited the sharp forward peaking of the scattered electrons, in the direction of the incident neutrino, to extract solar neutrino events from a significant but isotropic background. The "pointing" of events back to the sun (see fig. 1.3) provided the first direct evidence that neutrinos originated from the sun.

Apart from having an important role in the solar neutrino detection these real time experiments had an even bigger impact on neutrino physics by

1 Neutrino Physics and Experiments

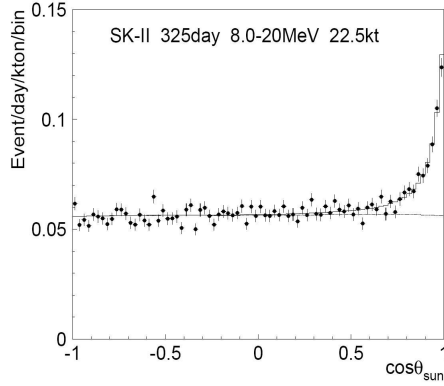


Figure 1.3: Angular distribution to the sun observed in SK.

investigating the so called atmospheric neutrino anomaly [HIR 88], [HIR 92]. The investigated neutrinos arise from the decay of pions and other mesons and also muons, which are produced in the earth's atmosphere (see chapter 3).

There is a significant zenith angle variation in the atmospheric neutrino flux, more prominent at higher energies, called "secant theta" effect. This is due to the fact, that the pions and muons which are produced by incoming cosmic rays with trajectories nearly tangential to the earth have more flight time in a less dense atmosphere and hence more chance to decay. The atmospheric-neutrino energies practically accessible in underground experiments range from a few tens of MeV to 1TeV, corresponding to flight distances from about 15 km for vertical, downward neutrinos up to 13.000 km for those traversing the earth from the far side. The atmospheric neutrino anomaly is based on the measured deficit of muon to electron neutrinos above an energy of $\sim 1\text{GeV}$ (see fig. 1.4). The observed ratio was about two-thirds of the expected value.

In 1998 the Super-Kamiokande experiment announced new evidence for muon neutrino disappearance. The MACRO [AMB 98] and the SUDAN-II [ALL 96], [ALL 99] experiments, which have also measured atmospheric neutrinos presented muon to electron neutrino ratios, which are consistent with the Super Kamiokande result.

The SNO detector [BOG 99] was built deep (4000 mwe) in the Creighton nr.9 nickel mine in Sudbury, Ontario, for the purpose of determining the flavor content of the ^8B solar neutrino flux. A central acrylic vessel containing

1.2 Solar Neutrino Experiments and Neutrino Oscillations

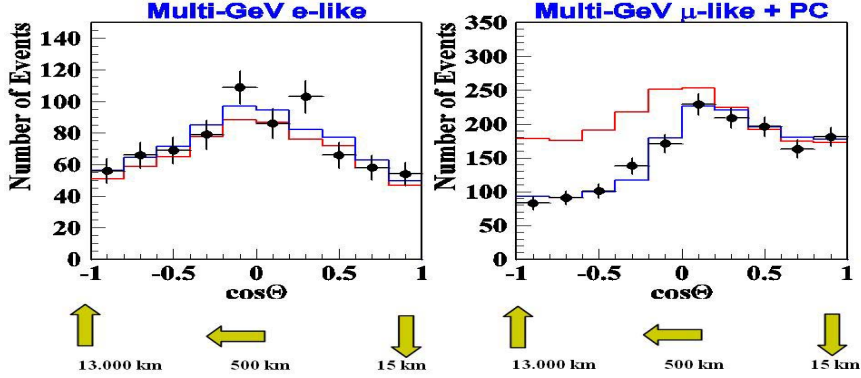


Figure 1.4: Zenith angle distributions for contained e-like and μ -like atmospheric neutrino events in Super Kamiokande [KEA 04]. $\cos\theta = 1$ corresponds to downward events with $L \sim 15$ km and $\cos\theta = -1$ corresponds to upward events with $L \sim 13,000$ km. The blue lines show the best fits without oscillations and the red lines with oscillations.

one kiloton of heavy water is surrounded by 5m (7 ktons) of light water to shield the inner volume from neutrons and γ s. The detector is viewed by 9500 8" PMTs, which provide a coverage of 56% .

The heavy water allows the experimenters to exploit three reactions with varying flavor sensitivities

$$\nu_e + D \rightarrow p + p + e \quad (1.5)$$

(CC: charged current)

$$\nu_x + D \rightarrow \nu'_x + p + n \quad (1.6)$$

(NC: neutral current)

$$\nu_x + e \rightarrow \nu'_x + e' \quad (1.7)$$

(ES: elastic scattering)

The NC reaction, which is observed through the produced neutron, provides no spectral information, but does measure the total solar neutrino flux, independent of flavor. The SNO experiment has used two techniques for measuring the neutrons. In the initial SNO pure D_2O phase the signal came

1 Neutrino Physics and Experiments

from the neutron capture on deuterium, which produces 6.25 MeV gammas. In a second phase 2.7 tons of salt were added to the heavy water so that Cl would be present to enhance the capture, producing 8.6 MeV gammas. The NC and CC events can be separated reasonably well because of the modest backward peaking ($\sim 1 - \cos(\theta)/3$) in the angular distribution of the CC events. This allows to determine the total and electron neutrino fraction of the solar neutrino flux. A third phase has begun in which direct neutron detection is provided in pure D_2O by an array of 3He -filled proportional counters.

Because the ES and CC scattered electrons are measured in the same detector, the ES reaction provides an important cross check on the consistency of the results from the CC and NC channel. The SNO results are presented in fig. 1.5. The deduced fluxes are [AHM 02]:

$$\Phi_{CC} = (1.59 \pm 0.08 \pm 0.07) \cdot 10^6 / cm^2 s \quad (1.8)$$

$$\Phi_{ES} = (2.21 \pm 0.28 \pm 0.10) \cdot 10^6 / cm^2 s \quad (1.9)$$

$$\Phi_{NC} = (5.21 \pm 0.27 \pm 0.38) \cdot 10^6 / cm^2 s \quad (1.10)$$

The total flux (NC) is in agreement with the SSM prediction [BAH 01], but the CC results indicate that almost 70% of the solar $^8B - \nu_e$ arrive on earth as neutrinos of different flavor(s). The ES results are in excellent accord with this conclusion, as fig. 1.5 shows, as well as with the Super-Kamiokande results. It should be highlighted that the experimental uncertainty on the 8B -flux is below the theoretical one.

1.2.2 Vacuum and Matter Oscillation

The conclusion that was obtained from all these experiments over the last four decades is that no SSM change can completely remove the discrepancy, first identified by Davis, between the predicted ν_e flux and the measured one. The solution is due to new particle physics, neutrino oscillations. This phenomenon lies outside the minimal standard model, requiring massive neutrinos

1.2 Solar Neutrino Experiments and Neutrino Oscillations

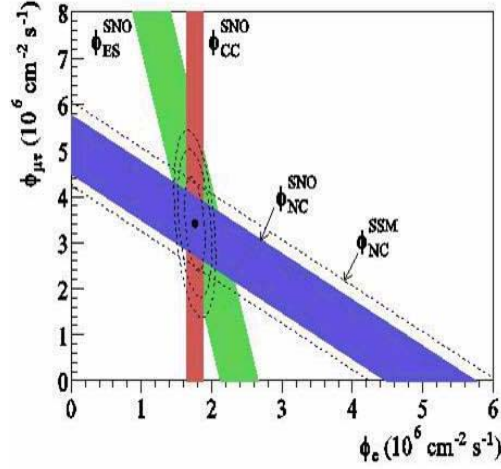


Figure 1.5: [AHM 02]

and a nontrivial relationship between mass and weak-interaction eigenstates. Neutrino oscillations were first hypothesized by Bruno Pontecorvo in 1957 [PON 68], and independently by Z. Maki, M. Nakagawa and S. Sakata from Nagoya, Japan in 1962 [MAK 62].

In the minimal Standard Model neutrinos have fixed helicity, $H(\nu)=-1$ and $H(\bar{\nu})=1$ which requires them to be massless, but the reasons for this are not fundamental. They can not possess Dirac mass terms like other fermions, since the model contains no right-handed neutrino fields. However, in an extended standard model, where lepton-violation is allowed, they can have Majorana mass terms where the neutrino and the anti-neutrino is one and the same particle with different helicity. If neutrinos have mass, it does not mean that the electron-,muon- and tau-neutrino have fixed masses. It is possible that an electron-neutrino, for example, is a composite particle made up of a superposition of different fixed massive neutrino eigenstates. This can be written as:

$$\nu_\alpha = \sum_{j=1}^n U_{lj}^* \nu_j \quad \alpha = e, \mu, \tau \quad (1.11)$$

where ν_α are the flavored neutrinos, ν_j are the neutrino eigenstates having a mass m_j , with $p \gg m_j$, and U is the PontecorvoMakiNakagawaSakata (PMNS) mixing matrix. Here ν_j is the state of a neutrino with negative

1 Neutrino Physics and Experiments

helicity, mass m_j and the energy:

$$E_j = \sqrt{p^2 + m_j^2} \simeq p + \frac{m_j^2}{2p} \quad (1.12)$$

All existing ν -oscillation data, except the data of the LSND experiment can be described assuming 3- ν mixing in vacuum. The PMNS matrix can be parameterized by 3 angles, and, depending on whether the massive neutrinos ν_j are Dirac or Majorana particles, by 1 or 3 CP-violation (CPV) phases [PAS 05].

$$U_{PMNS} = \begin{pmatrix} c_{12}c_{13} & s_{12}c_{13} & s_{13} \\ -s_{12}c_{23} - c_{12}s_{23}s_{13}e^{i\delta} & c_{12}c_{23} - s_{12}s_{23}s_{13}e^{i\delta} & s_{23}c_{13}e^{i\delta} \\ s_{12}s_{23} - c_{12}c_{23}s_{13}e^{i\delta} & -c_{12}s_{23} - s_{12}c_{23}s_{13}e^{i\delta} & c_{23}c_{13}e^{i\delta} \end{pmatrix} \cdot \begin{pmatrix} 1 & 0 & 0 \\ 0 & e^{i\frac{\alpha_{21}}{2}} & 0 \\ 0 & 0 & e^{i\frac{\alpha_{31}}{2}} \end{pmatrix} \quad (1.13)$$

where $c_{ij} = \cos\theta_{ij}$, $s_{ij} = \sin\theta_{ij}$, $\theta_{ij} = [0, \pi/2]$, $\delta = [0, 2\pi]$ is the Dirac CPV phase and α_{21}, α_{31} are two Majorana CPV phases.

At the production point (i.e. at the time $t=0$) the state of the neutrino ν_l is given by the equation 1.11. According to Schrödinger equation the mass eigenstates m_j evolve in time with the phase factor $\exp(-iE_j t)$. Since neutrinos are detected via weak interaction processes the expansion of the state of equation 1.11 in the basis of flavor neutrino states ν_β one obtains:

$$\nu_{\alpha t} = \sum_{\beta=1}^n \sum_{j=1}^n U_{\beta j} e^{-iE_j t} U_{\alpha j}^* \nu_\beta \quad (1.14)$$

The probability of the transition $\nu_\alpha \rightarrow \nu_\beta$ is given by:

$$P_{\nu_\alpha \rightarrow \nu_\beta} = \left| \sum_{j=1}^n U_{\beta j} e^{-iE_j t} U_{\alpha j}^* \right|^2 \quad (1.15)$$

Using the ultrarelativistic approximation of equation 1.12 and the unitary relation:

1.2 Solar Neutrino Experiments and Neutrino Oscillations

$$\sum_j^3 U_{\beta j} U_{\alpha j}^* = \delta_{\alpha\beta} \quad (1.16)$$

1.15 can be written as:

$$P_{\nu_\alpha \rightarrow \nu_\beta} = \left| \delta_{\alpha\beta} + \sum_{j=2}^n U_{\beta j} U_{\alpha j}^* \left[\exp - i \frac{\Delta m_{jl}^2 L}{2E} - 1 \right] \right|^2 \quad (1.17)$$

If there is no mixing (i.e. $U_{PMNS=I}$ or $\frac{\Delta m_{jl}^2 L}{E} \ll 1$ for all j, then no transitions $P_{\nu_\alpha \rightarrow \nu_\beta}$ can take place. If at least one Δm^2 satisfies the condition:

$$\Delta m^2 \geq \frac{E}{L} \quad (1.18)$$

neutrino oscillation becomes observable, whereby Δm^2 is the squared neutrino mass difference, L is the distance between neutrino production and detection and E is the neutrino energy.

Since neutrino oscillation experiments are often analyzed under the simplest assumption of oscillation between two neutrino types the U_{PMNS} mixing matrix of equation 1.13 can be written as:

$$U_{\alpha\beta} = \begin{pmatrix} \cos\theta & \sin\theta \\ -\sin\theta & \cos\theta \end{pmatrix} \quad (1.19)$$

In this case there is only one mixing angle and no CPV phase. With this assumption the transition probability of equation 1.17 becomes:

$$P_{\nu_\alpha \rightarrow \nu_\beta} = \frac{1}{2} \sin^2 2\theta \cdot \left(1 - \cos \frac{\Delta m^2 L}{2E} \right) \quad (1.20)$$

Here the amplitude of the neutrino transition probability is determined by $\sin^2 2\theta$, while the oscillation phase is determined by $\frac{\Delta m^2 L}{E}$.

L. Wolfenstein studied in 1978 [WOL 78] the effect of coherent forward scattering in matter by charged currents results in phase shifts in neutrino oscillations. Since ordinary matter consists of electrons, but no muons or taus,

1 Neutrino Physics and Experiments

the W boson exchange causes a relative phase shift of the electron neutrino flavor. This relative phase shift then translates into changes of the neutrino oscillation probabilities. In fact, he discovered that in general if there exists an interaction through which neutrinos can change flavor, this flavor change can be enhanced or even be only possible if the neutrinos travel through matter. The matter effect can be described by the potentials V_e, V_α . In usual medium a difference of the potentials for ν_e and ν_α ($\alpha = \text{other neutrino types apart from sterile neutrinos}$) due to the charged current scattering of ν_e on electrons can be written as:

$$V(x) = V_e - V_\alpha = \sqrt{2}G_F n_e(x) \quad (1.21)$$

where G_F is the Fermi coupling constant and $n_e(x)$ stands for the electron density in matter at point x. The difference of the potentials leads to an additional phase difference in the neutrino system. In the presence of matter the Hamiltonian of system changes: $H_0 \rightarrow H_0 + V$, where H_0 is the Hamiltonian in vacuum. Correspondingly, the eigenstates and the eigenvalues of H change: $\nu_1, \nu_2 \rightarrow \nu_{1m}, \nu_{2m}$. The Schrödinger equation for neutrino propagation in matter is modified with a term that contains the additional potential V :

$$i \frac{d}{dt} \begin{pmatrix} \nu_e \\ \nu_\alpha \end{pmatrix} = \begin{pmatrix} -\frac{\Delta m^2}{2E} \cos 2\theta + V & \frac{\Delta m^2}{2E} \sin 2\theta \\ \frac{\Delta m^2}{4E} \sin 2\theta & 0 \end{pmatrix} \begin{pmatrix} \nu_e \\ \nu_\alpha \end{pmatrix} \quad (1.22)$$

The solution of equation 1.22 can then be obtained by diagonalisation. By introducing new parameters Δm_m^2 and θ_m (with the subscript m for matter), the mixing angle can be obtained from:

$$\sin^2 2\theta_m = \frac{\sin^2 2\theta}{(\cos^2 2\theta - 2\sqrt{2}G_F n_e(x)E/\Delta m^2)^2 + \sin^2 2\theta} \quad (1.23)$$

In 1984, S.P. Mikheev and A. Yu. Smirnov [MIK 85],[MIK 86] noticed that for specific oscillation and matter density parameters, the enhancement could develop a resonance behavior, the so called MSW effect. For

$$\sqrt{2}G_F n_e(x) = \frac{\Delta m^2}{2E} \cos 2\theta \quad (1.24)$$

1.3 Results of Neutrino Oscillation Experiments

$\sin^2 2\theta_m = 1$ thus the mixing becomes maximal.

In the special case of a neutrino with the energy E traversing a decreasing electron density $n_e(x)$, like a neutrino produced inside the sun and traveling outwards, it has also to cross a layer, where the electron density causes the resonance case, thus locally yielding the maximal oscillation probability of 1. If a neutrino of a certain vacuum state (e.g. ν_1) traverses this resonance layer adiabatically, which means that the matter density changes slowly compared to the neutrino oscillation length, it is converted into the other vacuum state (ν_2) in any case. In order to fulfill the resonance condition an adiabatic neutrino translation and a sufficient matter density is required. The first condition puts a lower limit and the second an upper limit on the energy of the neutrino, thus allowing the MSW effect in a certain energy range only.

1.3 Results of Neutrino Oscillation Experiments

The atmospheric flux measurement at Super-Kamiokande was the first constraining evidence in favor of neutrino oscillation. The neutrino experiments described above have measured some deficiency in the expected solar neutrino flux and from these measurements all the positive evidence for non-vanishing values of neutrino masses and mixing can be deduced.

For a global analysis of solar neutrino all data from solar neutrino experiments are analyzed in a global fit. All these experiments measure the survival probability $P(\nu_\alpha \rightarrow \nu_\alpha)$. Under the assumption of CP-conservation the conclusive data from the long baseline reactor experiment KamLAND, measuring the survival probability ($P\bar{\nu}_\alpha \rightarrow \bar{\nu}_\alpha$) can be included in the global fit.

In the KamLAND [PIE 01] experiment the neutrinos originate from 16 nuclear power plants (130 GW thermal power) at distances between 80 and 800 km. The KamLAND detector consists of a one kiloton target of liquid scintillator (80% dodecane, 20% pseudocumene), and is installed in the former Kamiokande cavity at a depth of 2700 mwe. The spherical one kiloton scintillator and the surrounding 2.5 m mineral oil shielding are contained in an 18 m diameter stainless steel sphere that also supports the 2000 17" and

1 Neutrino Physics and Experiments

20" photomultipliers providing 30% coverage. KamLAND has started to take data in 2002, it has been observing neutrino oscillations by a disappearance of anti-electron neutrinos. The expected neutrino rate is calculated with the single distances and neutrino fluxes of all surrounding nuclear reactors, even varying when reactors are turned on or off [ARA 04].

Fig. 1.6 shows the results from recent analysis [BAH 04] of KamLAND $\bar{\nu}_e$ disappearance data, solar ν_e data and their combination under the hypothesis of CPT symmetry. The main features of these results are:

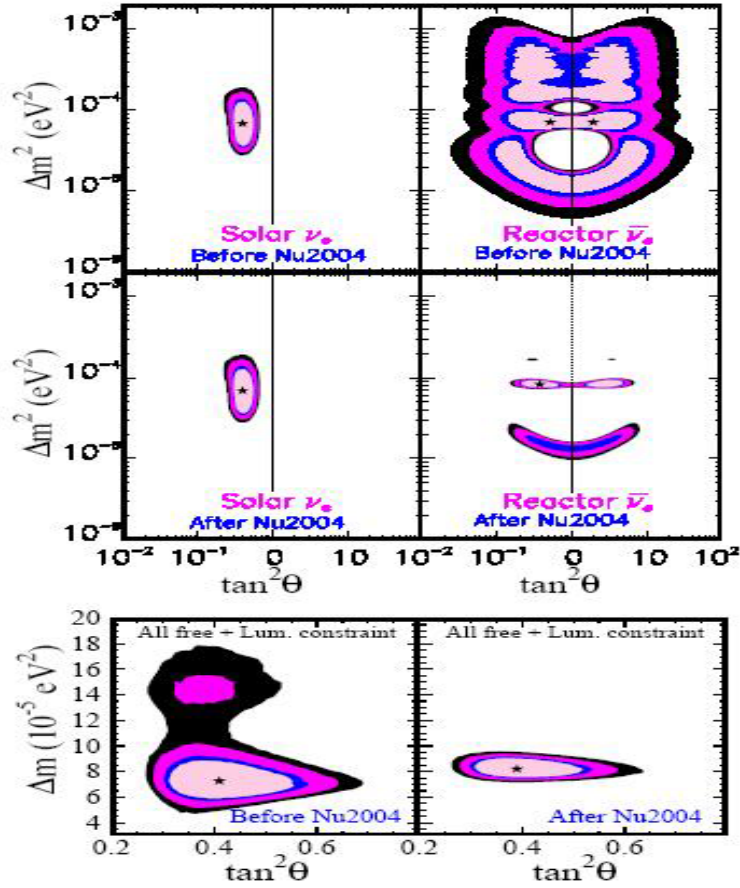


Figure 1.6: Allowed regions for 2- ν oscillations of solar ν_e and KamLAND $\bar{\nu}_e$ (upper four panels), and for the combination of KamLAND and solar data under the hypothesis of CPT conservation (lower two panels). The different contours correspond to the allowed regions at 90%, 95%, 99% and 3 σ CL.[GON 04]

1.3 Results of Neutrino Oscillation Experiments

In the analysis of solar data, only the Large Mixing Angle (LMA) solution is allowed at more than 3σ and maximal mixing is rejected by the solar analysis at more than 5σ . This result has been obtained by means of the release of the SNO salt-data (SNOII) in Sep 2003.

In the analysis of the new KamLAND data the 3σ region does not extend to mass values larger than $\Delta m_{21}^2 = 2 \times 10^{-4} eV^2$ because for larger Δm_{21}^2 values, the predicted spectral distortions are too small to fit the new KamLAND data.

The combined analysis allows only the lowest LMA region at 3σ with best-fit point and 1σ ranges [GON 04]:

$$\Delta m_{solar}^2 = [8.2_{-0.3}^{+0.3}] \times 10^{-5} eV^2, \tan^2 \theta_{solar} = 0.39_{-0.04}^{+0.05} \quad (1.25)$$

The best fit values for the atmospheric neutrino parameters are gained from the full data set of Super-Kamiokande phase I (SK1) as well as from the K2K experiment. K2K is the first accelerator long baseline neutrino experiment. The distance from the ν_μ source at K2K to the SuperKamiokande detector is about 250 km and the average energy of the ν_μ beam is about 1.3 GeV. Thus E/L corresponds to the oscillation region of the atmospheric neutrinos. The experiment is aimed at looking for the disappearance of the initial ν_μ flux, which is measured by the so-called near detector at KEK with a precision better than 8% [GON 04].

$$\Delta m_{atmo}^2 = [2.2_{-0.4}^{+0.6}] \times 10^{-3} eV^2, \tan^2 \theta_{atmo} = 1_{-0.26}^{+0.35} \quad (1.26)$$

The oscillation parameters for a three flavor analysis are two mass squared differences $\Delta m_{21}^2 = \Delta m_{solar}^2, \Delta m_{32}^2 = \Delta m_{atmo}^2, \Delta m_{31}^2 = \Delta m_{CHOOZ}^2 \simeq \Delta m_{32}^2$ and three mixing angles which are usually denoted as $\theta_{12}, \theta_{23}, \theta_{13}$ with the mixing matrix U parameterized in the standard MNS form. In the limit $\Delta m_{21}^2 \ll \Delta m_{32}^2$, which is indicated by the two generation analysis of atmospheric and solar neutrino data, the atmospheric neutrino probabilities depend on $\Delta m_{32}^2, \theta_{13}, \theta_{23}$ and solar neutrino probabilities depend on $\Delta m_{12}^2, \theta_{13}, \theta_{12}$. The CP-violation phases can be neglected in this limit. Clearly for $\theta_{13} = 0$ solar and atmospheric neutrinos decouple. The remaining mixing angle θ_{13}

1 Neutrino Physics and Experiments

has not been measured yet. The best limit comes from the Chooz reactor antineutrino experiment [CHO 98], [CHO 99], [CHO 00] and [CHO 03], whereby the probability for the Chooz experiment depends on $\Delta m_{32}^2, \theta_{13}$.

$$\sin^2 2\theta_{13} < 0.2 \quad 90\%CL \quad (1.27)$$

The above mentioned LSND accelerator neutrino experiment [ATH 96], [ATH 97], [AGU 01], which ran from 1992 - 1997 at Los Alamos National Laboratory, observed an excess of $(87.9 \pm 22.4 \pm 6.0)\bar{\nu}_e$ events in the almost pure $\bar{\nu}_\mu$ beam from π decay at rest. The statistical significance of the excess is 3.8σ . This result can be accommodated together with those from solar-, reactor-, atmospheric- and long baseline-neutrino experiments into a single neutrino oscillation framework only, if there are at least three different scales of neutrino mass-squared differences. As a first attempt to generate the required scales one can invoke the existence of a fourth light neutrino, which must be *sterile* in order not to affect the invisible Z^0 decay width, precisely measured at LEP. The allowed oscillation region of LSND has been largely suppressed by the KARMEN experiment [KAR 02] which found no evidence for $\bar{\nu}_\mu \rightarrow \bar{\nu}_e$ oscillation. The remaining region of the allowed parameter space corresponds to $\Delta m_{LSND}^2 = (0.2 - 1)eV^2$ or $7eV^2$ and a small mixing angle [BAR 03]. The MiniBooNE experiment at Fermi National Accelerator Laboratory will confirm or refuse the LSND result with higher statistics and different sources of systematic errors [BRI 05].

Neutrino oscillations are by far the best theoretical explanation of the features of all the collected data on the atmospheric, accelerator, solar and reactor neutrinos. Alternative theoretical ideas, e.g. the neutrino decay or CPT non-conservation, are not favored by the data [BAR 03].

1.4 Open Questions in Neutrino Physics and Future Neutrino Experiments

In the last few years there has been a remarkable progress in understanding the neutrino physics. Compelling evidence for the existence of neutrino mixing and oscillations has been presented in experiments using neutrinos from

1.4 Open Questions in Neutrino Physics and Future Neutrino Experiments

the atmosphere, from the sun, from reactors and from accelerators. However a large amount of open questions have to be answered in future neutrino experiments. The future experimental program can be divided into two phases: measurements done by the running and/or already accepted experiments and the further future experiments, which are now in the planing phase. The near future measurements will bring further improvements in the determination of the oscillation parameters for the dominant oscillations in the solar and atmospheric regions. The main challenge for the further future experiments is a very precise determination of the θ_{13} mixing angle with the ultimate goal of determining the CP violation in the leptonic sector. Some open questions in neutrino physics are presented in the following:

1. Running and future solar neutrino experiments

Present and future solar neutrino experiments aim to confirm the LMA solution and to detect the characteristic behavior expected from the solution (i.e. the low energy upturn of the 8B spectrum). A precise measurement of the absolute fluxes from low energy regions would intermediate energy regions where a transition from the vacuum to the matter oscillation happens. Those measurements do also provide a way to determine the oscillation parameters precisely. Small deviations from the LMA solution are important and interesting. Sterile neutrinos may mix into the active neutrinos although the admixture is known to be small even if they exist [HOL 04]. This test can be done best by the measurement of the pp-neutrinos for which the uncertainties of the prediction of the flux is very small. One of the original aims of the measurement of the solar neutrinos is to understand the current energy creation mechanism in the sun. Suppose the oscillation parameters will be determined sufficiently well, then the measured solar neutrino flux on the earth can be converted to the flux created in the sun. Then the measurements of the entire solar neutrino spectrum will provide the information of the nuclear reactions interior of the sun [BAH 03], for instance the contribution of the CNO-cycle.

2. Determination of the mass spectrum (hierarchy)

The oscillation experiments bring information about the differences of the masses squared. They cannot measure neutrino masses. Since the sign of Δm_{32}^2 is unknown yet, two possibilities of the mass ordering exist. They are called normal and inverted mass hierarchies and are depicted in fig. 1.7. If

1 Neutrino Physics and Experiments

the mass of the lightest neutrino is small, then the mass of the heaviest one is $\sqrt{\Delta m_{32}^2} \approx 40$ meV and either of these hierarchies can exist. If the lightest neutrino is heavy ($m \gg 40$ meV), the neutrino masses are quasi-degenerated.

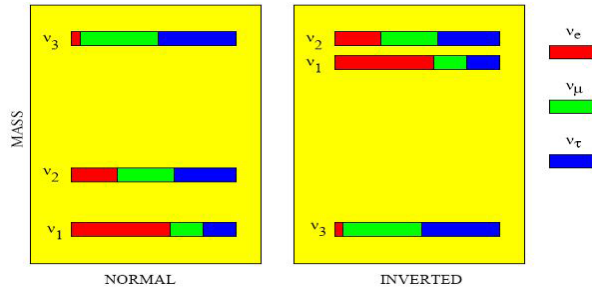


Figure 1.7: Neutrino mass and flavor spectra for the normal (left) and inverted (right) mass hierarchies. The distribution of flavors (colored parts of boxes) in the mass eigenstates corresponds to the best-fit values of mixing parameters and $\sin^2 2\theta_{13}=0.05$ [SMI 04]

3. What is the mass of the lightest neutrino?

In order to distinguish between the mass hierarchies and the case of quasi-degenerate neutrino masses the sensitivity of the mass measurements must be better than 40 meV. The effective mass determined from the end-point region of the electron spectrum in H^3 beta-decay is:

$$m_\beta^2 = \sum_j |U_{ej}|^2 m_j^2 \quad (1.28)$$

The present limit $m_\beta \leq 2.2$ eV at the 2 level comes from the Troitsk [LOB 01], [LOB 02] and Mainz [WEI 02] experiments. A big collaboration is working on the next-generation experiment KATRIN [OSI 01], which will start in 2007 and whose sensitivity should eventually reach 0.2eV.

A different way of probing the absolute neutrino mass is by measuring half lives $T^{0\nu_{1/2}}$ of the neutrinoless double beta decays ($\beta\beta 0\nu$), which can occur only if neutrinos are Majorana particles. Double Beta Decay is a rare spontaneous nuclear transition in which the charge of two isobaric nuclei changes by two units with the simultaneous emission of two electrons. The parent nucleus must be less bound than the daughter one, while it is generally required

1.4 Open Questions in Neutrino Physics and Future Neutrino Experiments

that both be more bound than the intermediate one, in order to avoid the equivalent sequence of two single beta decays. These conditions are fulfilled in nature for a number of even-even nuclei. The decay can then proceed both to the ground state or to the first excited states of the daughter nucleus. The effective mass $m_{\beta\beta}$ is related to the measured half-lives $T^{0\nu_{1/2}}$ and to a not well known nuclear matrix element. The current best upper limits on $m_{\beta\beta}$ come from the HeidelbergMoscow [GUN 97] ($m_{\beta\beta} < 0.35$ eV) and the IGEX [AAL 02-1] ($m_{\beta\beta} < (0.33 - 1.35)$ eV) experiments. Several new experiments, exploiting challenging techniques, are being prepared with a goal of reaching high sensitivity. Among them are four proposed ^{76}Ge experiments: GENIU [KLA 04], Majorana [AAL 05] and the GERDA experiment proposed for Gran Sasso [ABT 04], the cryogenic experiments CUORE [FIO 05] and the large Xe experiments EXO [HAL 03] and XMASS [MOR 03].

4. Determination of the parameter $\sin^2 2\theta_{13}$ and of the CPV phase.

The determination of θ_{13} , the third mixing angle, which describes the $\nu_\mu \rightarrow \nu_e$ oscillation in the atmospheric region, is an intriguing and extremely challenging measurement in the domain of neutrino oscillations. An upper limit on $\sin^2 2\theta_{13}$ of 0.2 comes from the Chooz experiment [CHO 03]. The near future accelerator experiments (MINOS [SAA 04], ICARUS [BUE 05], OPERA [AUT 05]) should provide further constraints. After five years of data taking MINOS should reach the sensitivity of 0.06 - 0.08 (depending on the systematic uncertainty).

The possibility to measure the CP violation in the leptonic sector depends on the value of $\sin^2 2\theta_{13}$, and the measurement of $\sin^2 2\theta_{13}$ itself depends on the other oscillation parameters (correlations) quadratically and trigonometrically (degeneracies). Thus, $\sin^2 2\theta_{13}$ has to be measured before deciding on the measurements of the CP violation and, in order to resolve the ambiguities, several measurements under different experimental conditions should be performed. One of the proposed experiments is the reactor anti-neutrino experiment Double-Chooz [LAS 04], which is based on the detection technique of the former Chooz experiment, but using two similar detectors (a near one, close to the reactor and a far one approximately one km from the reactor). The hope is to keep the systematic errors below 3%. This would set the limit of $\sin^2 2\theta_{13}$ down to 0.03 or even saddle $\sin^2 2\theta_{13}$, in case that oscillation is observed. Since only a non zero $\sin^2 2\theta_{13}$ induces CP violation

1 Neutrino Physics and Experiments

in the neutrino sector the reactor neutrino measurement is mandatory to justify the high costs of further future accelerator experiments.

5. Determination of neutrino magnetic moment. If neutrinos have mass, they may have a magnetic moment.

The couplings of neutrinos with the photons are generic consequences of finite neutrino masses, and are one of the important intrinsic neutrino properties to explore [VOG 89]. Since the mid 80s, the neutrino magnetic moment hypothesis has been widely discussed in the context of astrophysics. The solar neutrino flux measured by the Homestake experiment seemed to show a significant time variation in correlation with the solar magnetic activity as reported in [DAV 96]. It was shown that this correlation could be caused by the interaction of the neutrino magnetic moment with the magnetic field in the convective zone of the Sun. This interaction leads to a flip of the neutrino helicity converting left-handed neutrinos into right-handed ones, which are not participating in the charged current reactions in the detector. The value of the magnetic moment required for the observation of such variations with the present operating solar neutrinos detectors lies in the range of $(10^{-10}10^{-11})\mu_B$. Up to now there are no indications of any measurable/observable positive signatures in the current and future rounds of experimental efforts. Improvement in sensitivities will necessarily involve new neutrino sources as well as novel neutrino detection techniques and channels. These advances may find important potential applications in other areas of neutrino and underground physics experimentations [WON 04].

Chapter 2

The Solar Neutrino Experiment BOREXINO

The idea to realize a real time neutrino experiment for the low energy part of the solar neutrino flux was pronounced in the late 80's by R. Raghavan and collaborators. In the mid of the 90's the implementation of the experiment was started in hall C of the Gran Sasso underground laboratory at a depth of 3600 meters of water equivalent. The experiment name "Borexino" is a modification of the former name "Borex" which was correlated to the initial idea to build an experiment based on boron loaded scintillator, in order to measure the solar 8B -neutrino flux.

2.1 Motivation and Detector Design

Borexino [ALI 02] is an unsegmented liquid scintillator detector at the Gran Sasso Laboratory, which aims to measure sub-MeV solar neutrinos through neutrino-electron elastic scattering. In particular the main goal of Borexino is the measurement of the 862 keV mono-energetic ${}^7\text{Be}$ neutrinos (see fig. 1.2). ${}^7\text{Be}$ neutrinos comprise about 7% of all solar neutrinos and are the second most intense solar neutrino source, after the primary pp-neutrinos. Neutrinos of all flavors are supposed to interact by neutral current elastic scattering processes on electrons, whereby the cross section for ν_e compared to other neutrinos is enhanced by a factor of ≈ 6.5 in the considered energy range due to the additional charged current interactions. The production of μ or τ leptons via CC interactions is excluded due to the high rest-energy of the leptons and the low neutrino energy range (250keV \sim 15MeV). The electrons involved in scattering processes will deposit their kinetic energy in the liquid scintillator. The generated light signal contains enough information to determine energy, position, shape and time of the event.

The experiment has been designed with a neutrino target of 300 tons of pseudocumene (PC) solvent plus 1.5g/l of the wavelength shifter PPO, surrounded by several layers of shielding liquid. A 10 mm thick stainless steel external tank provide \approx two meter of high purity water shielding against neutrons and gammas from the surrounding rocks. An inner sphere (SSS) contains the PC and supports 2200 8" photomultipliers supplied by ETL. Two 0.125mm thick nylon vessels inside the SSS subdivide the stainless steel sphere in three regions: the innermost active region, housing 300 tons of scintillator, whereby only the innermost 100 tons are taken as fiducial volume FV, and the inner and outer buffers, which are separated by a second nylon vessel "shroud" acting as a radon barrier, containing a quenched solvent. Fig. 2.1 shows a sketch of the Borexino detector.

At the Borexino detector site in the hall C several detector facilities are used in order to assure the functioning of the detector. Fig. 2.2 shows an overview of the Borexino area in hall C of the Gran Sasso Laboratory. The scintillator can be stored in four 100 tons tanks in the storage area before being filled into the detector by means of the fluid handling system (Module-0). CTF is the prototype of Borexino (see. section 2.4). All the detector electronics, as well as the data acquisition (daq) center is placed in the "big

2.2 Borexino after SNO and Kamland

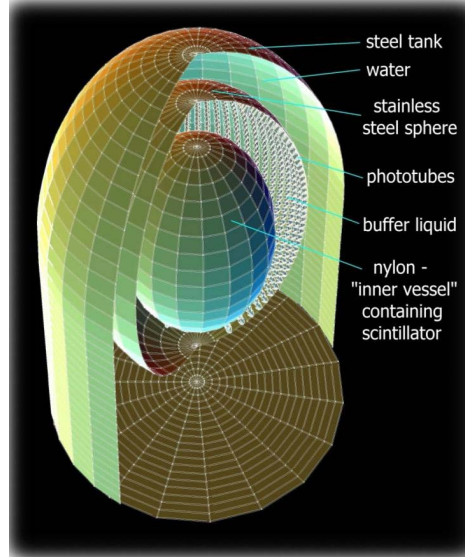


Figure 2.1: Schematic of the Borexino Detector

building west". The scintillator purification occurs in the water extraction, distillation and silica gel chromatography modules [NIE 05].

2.2 Borexino after SNO and Kamland

In the fiducial volume of the Borexino experiment solar neutrinos will produce about 33 events/day in the LMA scenario. The neutrino signal from the ${}^7\text{Be}$ -neutrinos will show a Compton-like edge at 0.667 MeV like shown in fig. 2.3.

The current experimental determination of the ${}^7\text{Be}$ -neutrino flux from other experiments, assuming the solar luminosity constraint, is $0.91^{+0.24}_{-0.61}$ of the flux expected from the SSM [BAH 03], with a very large experimental error. When the constraint on solar luminosity is removed, the ${}^7\text{Be}$ neutrino flux is essentially undetermined. A measurement of the ${}^7\text{Be}$ -neutrino flux with a 10% precision will improve the current error on the ${}^7\text{Be}$ neutrino flux significant. Together with the solar luminosity constraint it will also improve the determination of the pp-neutrinos flux from the Gallium experiments, which have significant contributions both from the pp- and the ${}^7\text{Be}$ -neutrinos. The pp-neutrino flux will be determined experimentally with a precision below 1%, thus testing the 1% theoretical prediction of the SSM.

2 The Solar Neutrino Experiment BOREXINO

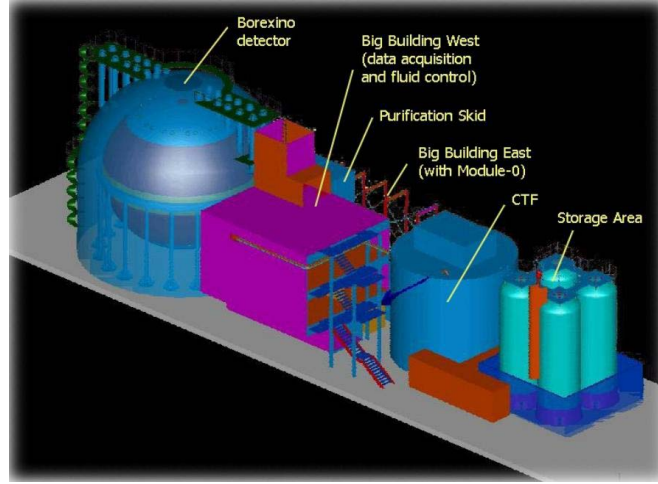


Figure 2.2: The Borexino detector site in hall C of the Gran Sasso Laboratory

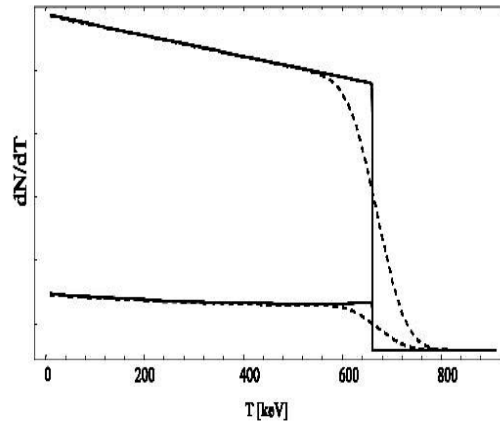


Figure 2.3: Shapes of the recoil electron spectra caused by the ${}^7\text{Be}$ solar neutrino line at 862keV (arbitrary units). The maximal recoil energy is 665 keV. The dotted lines are modified according to the detector resolution. The upper curve shows the higher cross section for ν_e (CC and NC) in contrast to ν_μ and ν_τ (lower line, only NC).

2.2 Borexino after SNO and Kamland

For the predicted LMA solution the vacuum oscillation is a dominant process for solar neutrinos with energy below ~ 1 MeV. The expected neutrino spectrum from all solar neutrino fluxes is shown in fig. 2.4. The experimental probe of the transition between matter and vacuum oscillation, a transition which is expected to happen in the 2-3 MeV range and which requires real time detection of low energy neutrinos to be experimentally demonstrated, is important. This feature is shown in fig. 2.5.

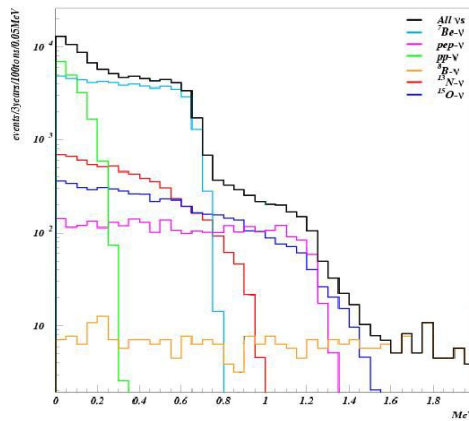


Figure 2.4: Spectrum of the expected solar neutrino events in Borexino

Apart from the measurement of solar neutrinos Borexino will provide unique measurement opportunities for Supernova neutrinos. Liquid scintillators have some unique advantages [CAD 02] as they should reveal the intensity of the three flavors as well as information on the energy spectrum. About 100 events are expected from a Supernova in the galactic center.

Borexino will be sensitive to pep-, CNO- and 8B -neutrinos, all less intense than 7Be neutrinos. The cosmogenic background exceeds the neutrino signal from these neutrino fluxes by far, thus a strong reduction of this background is needed. Methods for the suppression of the cosmogenic background are discussed in chapter 3 and 4.

Due to the fact that there are no nuclear power plants in Italy (i.e. next reactor is more than 800 km away from the Borexino detector site), reactor anti-neutrinos (2MeV-8MeV) can be separated from geophysical anti-neutrinos (≤ 2.5 MeV). Therefore the measurement of geophysical anti-neutrinos coming

2 The Solar Neutrino Experiment BOREXINO

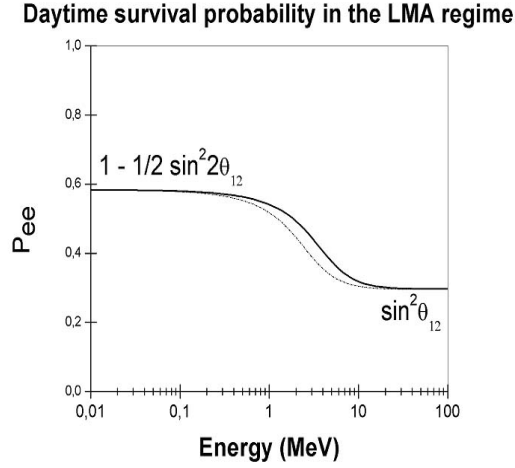


Figure 2.5: Daytime survival probability for the LMA regime. The dotted line corresponds to a higher electron density in the Sun.

from beta decays in the U and Th chains is a further goal for the Borexino experiment. The model dependent expected rate of geophysical anti-neutrinos in Borexino is between 10 and 30 events per year which is equivalent to the rate of reactor anti-neutrinos (~ 15 events per year). The measurement of reactor anti-neutrinos would probe the LMA solution restricted by KamLAND.

2.3 Background

The suppression of background events is crucial in low counting rate experiments like Borexino. Difficulties mainly arise as electrons from neutrino scattering processes do not show any different signature compared to electrons from radioactive decays. The shapes of the energy spectra, a possible signature to recognize desired event groups of solar ${}^7\text{Be}$ -, pep- and CNO-neutrinos, get smeared off by the scattering process and the detector resolution. Considering this, the total background rate should not exceed typical neutrino event rates, in case of pep- and CNO-neutrinos around one event per day. So, especially in the energy range below 1.5 MeV where solar pep- and CNO-neutrino events are expected to appear, and even more in the so-called "neutrino window" of the ${}^7\text{Be}$ neutrino signal (250-800 keV), all possible radioactive decays must be taken into account.

- ^{14}C is a long lived isotope with a mean life of $\sim 5700\text{y}$ that decays emitting an electron of 156KeV . It is produced through the reaction $^{14}\text{N}(n, p)^{14}\text{C}$, triggered by neutrons produced in cosmic rays scattering. The ^{14}C content depends among other things on the age of the oil selected for the pseudocumene production. Since the ratio $^{14}\text{C}/^{12}\text{C}$ at the surface is around 10^{-12} , the age of the oil should be very high. The oil which was used for the Borexino experiment provides an excellent $^{14}\text{C}/^{12}\text{C}$ ratio in the order of 10^{-17} and a consequent detection threshold around 250 keV .
- The natural ^{238}U and ^{232}Th chains are producing the main part of the intrinsic scintillator radioactivity. Borexino can tolerate concentrations of this elements (assuming secular equilibrium) not much greater then 10^{-16}g/g . The CTFI and CTFIII campaigns have demonstrated the ability of the available techniques to purify the scintillator to this order of magnitude.
- Another intrinsic background component of the scintillator is the ^{40}K that can decay with a half life of $1.3 \cdot 10^9\text{y}$ in two different channels:

$$89.3\% \quad ^{40}\text{K} \rightarrow ^{40}\text{Ca} + e^- + \bar{\nu} \quad (\beta^-, Q = 1.32\text{MeV}) \quad (2.1)$$

$$10.7\% \quad ^{40}\text{K} + e^- \rightarrow ^{40}\text{Ar} + \nu_e + \gamma \quad (EC, Q = 1.46\text{MeV}) \quad (2.2)$$

^{40}K has an isotopic abundance of $1.2 \cdot 10^{-4}$ with respect to K_{nat} which in turn is present in earth crust with a 2.4% concentration. The Borexino background requirements imply, that the concentration of K_{nat} in the scintillator cannot exceed a concentration of 10^{-14}g/g .

- Further radioactive isotopes are ^{39}Ar , arising from the effect of cosmic radiation on argon in the air and ^{85}Kr a man-made fission product present in the air with an activity of 1.1Bq/m^3 .
- Looking detailed at the ^{238}U chain, the ^{222}Rn activity, turns out to be one of the most serious background problem for Borexino. ^{222}Rn itself, continuously present in the air at an activity level of $\sim 30\text{Bq/m}^3$, would decay soon enough with a half-life of 3.8 days and even is well removable by nitrogen extraction. However, it forms the long lived ^{210}Pb (22 years), that indeed emits a harmless 45 keV photon only, but maintains the activity of its decay daughters ^{210}Bi and ^{210}Po over a

2 The Solar Neutrino Experiment BOREXINO

long time period. The β decay of ^{210}Bi with its end point energy of 1.16 MeV and the α decay of ^{210}Po , in the liquid scintillator quenched from 5.4 to ~ 0.4 MeV, deposit nearly their whole energy in the relevant neutrino detection window.

Any radiation source external to the inner vessel, but leading to an energy deposition in the scintillator is called external background. In table 2.6 several background contributions from different detector parts are listed.

Component	^{238}U (g/g)	^{232}Th (g/g)	^{nat}K (g/g)	Total Mass (g)	Contribution ^a (ev/day/100t)
2200 PMTs	$3 \cdot 10^{-8}$	$1 \cdot 10^{-8}$	$2 \cdot 10^{-5}$	$38 \cdot 10^6$	0.06
Buffer PC	$1 \cdot 10^{-15}$	$1 \cdot 10^{-15}$	$5 \cdot 10^{-12}$	$8.7 \cdot 10^8$	≤ 0.004
Outer Vessel	$2 \cdot 10^{-11}$	$2 \cdot 10^{-11}$	$1 \cdot 10^{-8}$	$5 \cdot 10^4$	≤ 0.04
Concentrators	$2 \cdot 10^{-10}$	$1 \cdot 10^{-9}$	$3 \cdot 10^{-7}$	$6 \cdot 10^6$	0.01
Sphere	$2 \cdot 10^{-10}$	$1 \cdot 10^{-9}$	$3 \cdot 10^{-7}$	$3.7 \cdot 10^7$	≤ 0.007
Cables	$2.1 \cdot 10^{-8}$	$2.4 \cdot 10^{-8}$	$7 \cdot 10^{-6}$	$2 \cdot 10^5$	≤ 0.003
Rock					≤ 0.005
$^{222}\text{Rn}^b$					0.03
Total					0.11 ± 0.05

^aIn the 250 – 800 KeV energy window.

^bin the buffer PC with a 1mBq/m^3 activity.

Figure 2.6: Contributions to the external background from different components of the detector.

Apart from the intrinsic background of the scintillator and the external background the cosmogenic background plays an important role. This background will be discussed in detail in chapter 3.

2.3.1 Schematic of the Borexino read out electronics and trigger system

The 8 inch photomultipliers are produced by the british company Electronic Tubes Limited (ETL). They are provided with high voltage through 55 meter long submarine cables from Huber&Suhner. High voltage and signal travel along these single cables. The electronics of the inner and outer detector are two independent systems with different designs (see also chapter 5.2) that reflect the different signal processing needs of the two detectors.

The inner detector electronics is housed in 14 identical racks, each one comprises the following electronic components (to be found more detailed in [DAN 05]):

- the patch panel on top of the rack, which accepts the PMT cable connector;
- the calibration signal fan-out;
- the low voltage power supply for the front end crate;
- the adder board and the scaler module mounted on its front;
- the front end crate;
- the vme crate with the digital electronics and the PowerPC (PPC);
- the high voltage mainframe;
- the fast waveform digitizer;

Each PMT cable is connected to a front-end channel that decouples it from the high voltage and extracts a fast linear signal for timing purposes and an integrated signal for charge evaluation. Subsequently the two signals reach the digital part of the electronic chain where they are acquired. The number of triggered channels is counted and sent to the trigger board for eventual trigger formation. Whenever a trigger is received the stored information in the digital memory is read and sent to the data acquisition system. The Borexino trigger system performs the following operations:

- it evaluates the coincidence condition, and if it is fulfilled a main trigger formation from the inner detector is set;
- it evaluates the coincidence condition and if it is fulfilled a trigger formation from the outer detector is set, which can be the number of read PMTs or the analog sum discrimination;
- it provides test and calibration service triggers;
- it provides laser systems triggers, triggering the lasers or handling their internal triggers;

2 The Solar Neutrino Experiment BOREXINO

- it couples to a GPS receiver for providing an absolute time reference;
- it distributes the trigger signals and event identifiers to all subsystems;

The Borexino trigger condition is a general condition for the whole system. All detector subsystems are receiving the trigger signal for acquiring simultaneously, independent of the subsystem, which has set the trigger. No partial detector acquisition are foreseen.

In fig. 2.7 a schematic overview of the Borexino electronics with all subsystems is shown.

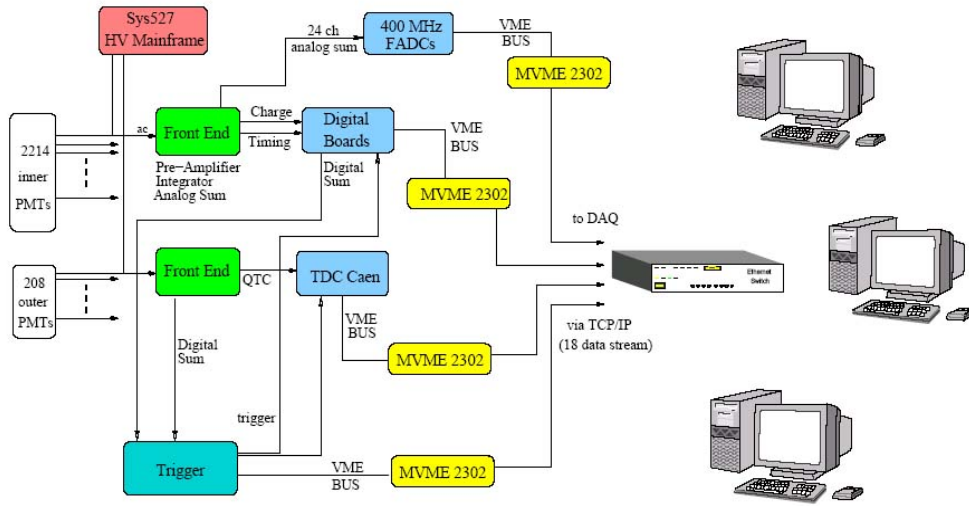


Figure 2.7: Schematic of the Borexino Electronics

2.4 The Counting Test Facility (CTF)

Before starting to setup the Borexino detector the collaboration accomplished the construction of a reduced scale prototype of the Borexino detector, named Counting Test Facility (CTF). The goal of this prototype was testing if the extremely high radiopurity levels required could be achieved. In its first data taking campaign, named CTFI, this prototype detector allowed to study the fundamental characteristics of two different scintillator mixtures, in particular the solution PC with PPO and an alternative solution of PXE (phenyl-o-xylylethane, $C_{16}H_{18}$) containing small concentrations of the wavelength

2.4 The Counting Test Facility (CTF)

shifters pTP (p-diphenylbenzene) and bis-MSB (1,4-bis-(2-methylstyryl)-benzene).

Not only scintillator purity questions determined the construction of the CTF, but also straight hardware concerns. During the CTFI campaign the collaboration has experienced the damage of half of the installed PMTs, which has led to the replacement of the submarine cables and connectors and to an improved PMT encapsulation. During the year 2000 a second campaign named CTFII was performed with the alternative scintillator PXE and the newly installed Cherenkov muon veto. During the last measuring campaign CTFIII some purification tests concerning silica gel chromatography and water extraction have been carried out in order to test various purification methods.

The CTF detector consists of a nylon Inner Vessel with a radius of one meter, containing a scintillator volume of 4.2m^3 , positioned in the center of a 1000m^3 water tank. In particular, the Inner Vessel is able to carry the buoyancy force of the pseudocumene scintillator in water. 100 photomultipliers surround the Inner Vessel, mounted on an open steel structure inside the water tank. After the CTFI phase, the Inner Vessel was replaced with an upgraded system of two nylon vessels, the inner containing scintillator and the outer - like the shroud in Borexino - acting as diffusion barrier for radon atoms. Fig. 2.8 shows an under water picture taken from the CTF during the last measuring campaign.

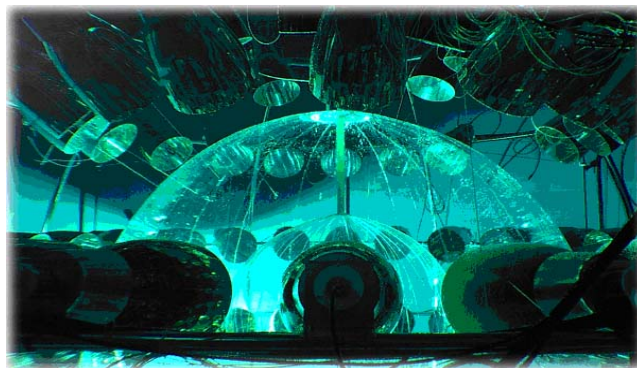


Figure 2.8: Interior of the CTF detector: Outer Vessel ("Shroud"), Inner Vessel and some of the surrounding phototubes, equipped with light concentrators.

In August 2002, during the CTFIII campaign, an accidental spill of about

2 The Solar Neutrino Experiment BOREXINO

50 liters of PC into the draining system of the underground laboratory, led to an abrupt end of all tests carried out with the CTF. All activities in hall C involving PC were immediately suspended, two months later even all systems containing PC were sealed by the responsible authorities. In May 2003 a summit of the crisis was reached by the sequestration of the whole hall C, which was then liberated again some weeks later. Since August 2002 CTF continues to take data in a "silent mode".

2.5 Status of the Detector

After a spill incident in August 2002 the operation of the experiment was only possible in a restricted mode for about one year. After the reopening of Hall C, the collaboration has managed to complete the installation of all the hardware components of the inner and outer detector. The purification plants for the removal of trace radioimpurities from the scintillator, which include a nitrogen sparging unit, a distillation unit, a silica-gel column and a water extraction unit have been completed. The inner and outer electronic parts comprising PMTs, cables, optical fibers and electronic boards have been installed, tested in detail and commissioned. The detector already works well as a spectrometer as shown in some recent air runs, where events were produced in an ampoule containing scintillator with an enriched radon contamination.

The delayed installation of the concentric nylon vessels, with a diameters of 8.5 and 11 meters respectively, was accomplished in March 2004. At that point the SSS could be closed and the installation of the outer muon detector could be finished (see chapter 5.5). The permission to handle liquids including PC was given to the collaboration at the beginning of 2005 after the completion of a retention basin in the hall C. The whole floor of the laboratory site was covered with a sealing resin to avoid any contamination of the ground water after a spill incident like the one in 2002. After an enormous effort on the sealing of the hall C and the improvement of the safety criteria the Borexino finally have gained back responsibility of the experiment. The detector is ready to be filled and to start taking data. The prospective start of the detection campaign is spring 2006.

Chapter 3

Muons and Muon Induced Background in Borexino

Cosmic rays were discovered about 90 years ago but even now their study is one of the important problems in physics and astrophysics. The existence of cosmic rays was discovered as the result of studying "dark" current in ionisation chambers (i.e. the observable current flowing in ionisation chambers without any artificial source of ionisation). In 1912 Victor Hess took a radiation counter (he used a gold leaf electroscope) on a balloon flight. He managed to observe that the amount of radiation increased as his balloon raised. This demonstrated that the radiation was from outer space and eventually it was dubbed "Cosmic Radiation". The intensity of the cosmic-ray particles hitting the earth atmosphere was measured by the first space vehicle 1959 and is given as:

- $I_{cr} \simeq 0.26 \text{ particle/cm}^2 \cdot \text{sterad} \cdot \text{sec},$
- $I_p \simeq 0.20 \text{ particle/cm}^2 \cdot \text{sterad} \cdot \text{sec},$
- $I_\alpha \simeq 0.03 \text{ particle/cm}^2 \cdot \text{sterad} \cdot \text{sec},$
- $I_{Z>2} \simeq 0.03 \text{ particle/cm}^2 \cdot \text{sterad} \cdot \text{sec},$

whereby I_p , I_α and $I_{Z>2}$ are the Intensities of the components of cosmic-rays protons, α , and particles with $Z > 2$ respectively [GIN 64]. The origin

3 Muons and Muon Induced Background in Borexino

of cosmic rays is not yet fully known, however it is clear that nearly all of the one above 1GeV come from outside the solar system, but from within the galaxy. Since the solar component of the cosmic ray spectrum dominates in the low energy area up to 1GeV it is mostly absorbed in the atmosphere thus is unimportant for the muon spectrum in the lithosphere. Unlike the solar component galactic cosmic rays can reach energies up to 10^{20} eV. The proportion of the major components of the cosmic rays are relatively constant with energy. They are well described by an inverse power law in energy, with differential flux given by:

$$\frac{dN}{dE} \propto E^{\gamma+1} \quad (3.1)$$

The spectrum continues up to $E \sim 10^6$ GeV with $\gamma \approx 1.7$. Above this energy the spectrum steepens to $\gamma \sim 2.0$ [GAI 90]. This change in the slope is called the "knee" of the spectrum. The average energy is 10 GeV. Although cosmic rays are studied for such a long time, many open questions are still present. For instance, it is not clear where and how these particles are accelerated to energies up to 10^{20} eV. The composition of cosmic rays is known with accuracy only at low and intermediate energies where the cosmic ray flux is high enough to collect directly significant statistics, taking the detectors at high altitude with balloons or satellites.

At higher energies ($E \sim 1000$ TeV) the flux is too low and one must rely on indirect measurements. In fig. 3.1 is shown the cosmic ray energy spectrum from 1 GeV up to the highest measured energies.

3.1 Muons induced by Cosmic Rays in the Atmosphere

High energy muons are the remnants of the air showers produced in the atmosphere by collisions of high energy cosmic ray nuclei with air nuclei. They were discovered by Anderson and Neddermeier in 1936 in cosmic rays. Till 1947 (year of the pion discovery) muons were considered as Yukawa particles, but their very low interaction rate was a puzzle. Since that time the muon parameters are well defined:

3.1 Muons induced by Cosmic Rays in the Atmosphere

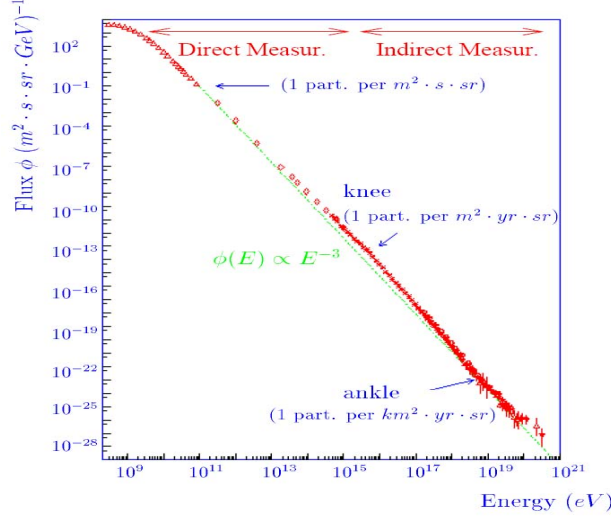


Figure 3.1: All particle cosmic ray energy spectrum. Above are approximately indicated the regions covered by direct and indirect measurements.

- Charge ± 1 , Spin $1/2$;
- Mass 105.658389 MeV;
- Lifetime 2.19703 ms;
- Decay (100%) $\mu \rightarrow e + \nu_e + \bar{\nu}_\mu$;
- No strong interaction.

The muonic component channels for the air shower decays and their branching ratios are:

$$\pi^\pm \rightarrow \mu^\pm + \nu(\bar{\nu}), \quad (\sim 100\%) \quad (3.2)$$

$$K^\pm \rightarrow \mu^\pm + \nu(\bar{\nu}), \quad (\sim 63.5\%) \quad (3.3)$$

A sketch of the secondary particle production by a cosmic ray particle in the atmosphere is shown in fig. 3.2. Apart from atmospheric neutrinos the muonic component is the only one that reaches the depths where underground detectors are placed. From the primary spectrum of cosmic ray

3 Muons and Muon Induced Background in Borexino

energies of equation 3.1, it is possible to evaluate the energy spectrum at the Earth surface of secondary uncorrelated muons, which is given, with good approximation, by [GAI 90]:

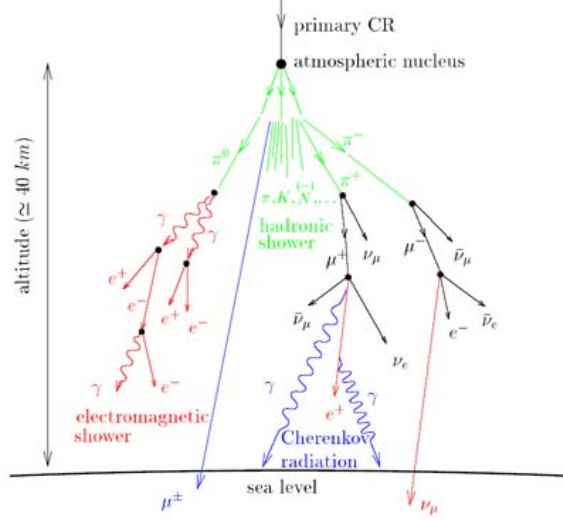


Figure 3.2: Sketch of particle generation in the collision of a cosmic ray with an atmospheric nucleus.

$$\frac{dN_\mu}{d\varepsilon d\Omega} \approx \text{const} \cdot \varepsilon^{-(\gamma+1)} \cdot \left(\frac{1}{1 + \alpha \varepsilon \cos\theta} + \frac{0.054}{1 + \beta \varepsilon \cos\theta} \right) \quad (3.4)$$

where ε is the muon energy at the surface, $\alpha = 1.1/115$ GeV and $\beta = 1.1/850$ GeV. The first and the second term in parenthesis of equation 3.4 represent the contributions of muons from π and K decays, respectively. In the limit of high energies (GeV), an approximate expression of the muon surface energy spectrum has the simple form:

$$\frac{dN_\mu}{d\varepsilon} = \text{const} \cdot \varepsilon^{-\alpha} \quad (3.5)$$

where $\alpha = \gamma + 2 \approx 3.7$. The surface muon spectral index is therefore related to the primary cosmic ray spectral index. Muons arriving in the underground Gran Sasso Laboratory have crossed at least 3100 mwe of standard rock, corresponding to a muon energy cut $E_\mu \geq 1.3$ TeV at the surface. This means that the primary cosmic ray energies range from some TeV/nucleon up to the maximum energies well beyond the "knee".

3.2 Muons in Underground Experiments

Muons are the most numerous energetic charged particles at sea level. They cannot avoid losing energy by ionization when passing through matter as they interact with the electric fields and typically knock loose some electrons. They ionize the immediate vicinity of their path due to collisions with electrons and hence lose some or all of their kinetic energy. H. A. Bethe and F. Bloch showed that a heavy particle with charge fe and of much bigger mass than the mass of an electron m_e that enters a material of number density n and ordinal number Z at a speed $\beta = v/c$ suffers a loss of kinetic energy per distance dx according to

$$\frac{dE_{kin}}{dx} = -\frac{Zf^2e^4n}{4\pi\epsilon_0^2m_e\beta^2c^2}\ln\left[\frac{2m_e\beta^2c^2}{W_{Ion}(1-\beta^2)} - \beta^2 - C\right] \quad (3.6)$$

where W_{Ion} is the mean ionization energy and C is a constant [Hae 95]. Summarizing the essence of above formula it becomes evident that the slower the particle is, the more energy it loses until it comes to rest. Minimal ionizing muons lose energy at a fairly constant rate of about 2 MeV per g/cm². The energy spectrum of underground muons can be derived taking into account the process of energy loss in the rock, which is assumed to have the form:

$$\frac{dE}{dX} = -(\lambda + \beta E) \quad (3.7)$$

where dX is a thin rock slab (usually in gcm⁻²), λ is the contribution from the ionization energy loss and βE is the contribution from radiative processes (bremsstrahlung, pair production and muon hadroproduction). The parameters λ and β are functions of the muon energy, but for practical purposes can be assumed as constants [GAI 90]. The quantity $\epsilon = \lambda/\beta$ is called the critical energy and is defined as the energy value above which the radiative processes become dominant. Fig. 3.3 shows the energy loss dE/dx of high energy muons in standard rock due to ionisation and to the radiative processes.

With the above assumptions, the general solution of equation 3.7 is:

$$E_\mu = (\varepsilon + \epsilon)e^{(-\beta h)} - \epsilon \quad (3.8)$$

3 Muons and Muon Induced Background in Borexino

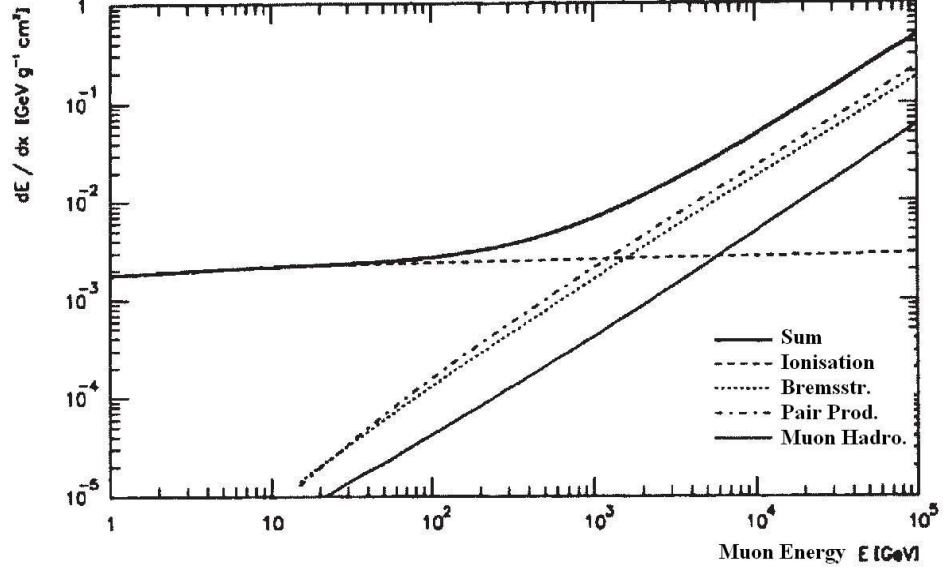


Figure 3.3: Contribution of Ionisation and radiative processes to the energy loss of high energy muons in standard rock.

where E_μ is the muon energy after crossing the rock slant depth h (g cm^{-2}). The underground muon energy spectrum can be thus obtained from equations 3.5 and 3.8 using the following relation:

$$\frac{dN}{dE_\mu} = \left[\frac{dN}{d\varepsilon} \right]_{\varepsilon=\varepsilon(E_\mu)} \cdot \frac{d\varepsilon}{dE_\mu} \quad (3.9)$$

and is given by

$$\frac{dN}{dE_\mu} = \text{const} \cdot (E_\mu + \epsilon(1 - e^{-\beta h}))^{-\alpha} \quad (3.10)$$

From eq. 3.10, the average underground muon energy at depth h is:

$$\langle dE_\mu \rangle = \frac{\epsilon(1 - e^{-\beta h})}{\alpha - 2} \quad (3.11)$$

and its asymptotic value for $h \rightarrow \text{inf}$ is $\epsilon/(\alpha - 2)$. At great depths h , the underground muon energy spectrum given by equation 3.10 is almost flat for $E \ll \langle dE_\mu \rangle$, and then decreases with energy. Fig. 3.4 shows the muon energy

3.2 Muons in Underground Experiments

spectrum at the Gran Sasso underground lab, measured by the MACRO collaboration [MIL 91]. At the depth of the Gran Sasso underground laboratory the average muon energy is (320 ± 12) GeV.

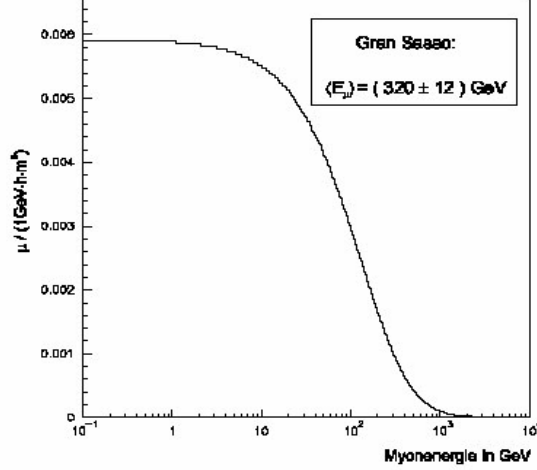


Figure 3.4: Local muon energy distribution at the Gran Sasso underground lab.[MIL 91]

To calculate the intensity of muons underground requires the intensity of muons at the surface as a function of energy and zenith angle, and the survival probability as a function of slant depth of rock traversed:

$$I_{\mu}(x, \cos\theta) = \int_0^{\infty} P(E_{\mu 0}, x) \frac{dI_{\mu 0}(E_{\mu 0} \cos\theta)}{dE_{\mu 0}} dE_{\mu 0} \quad (3.12)$$

where $P(E_{\mu 0}, x)$ is the probability of muon with an initial energy $E_{\mu 0}$ at sea level to reach the depth x and $dI_{\mu 0}(E_{\mu 0} \cos\theta)/dE_{\mu 0}$ is the muon spectrum at sea level at zenith angle θ . The intensity at the surface can be taken from [AGL 99]. Fig 3.5 shows the vertical muon intensity dependence on the depth, measured by the LVD collaboration (Large Volume Detector, a scintillator based detector measuring the same muons as Borexino will do) at Gran Sasso. The depth independent part of the muon intensity above 10 kmwe descends from neutrino induced muons.

3 Muons and Muon Induced Background in Borexino

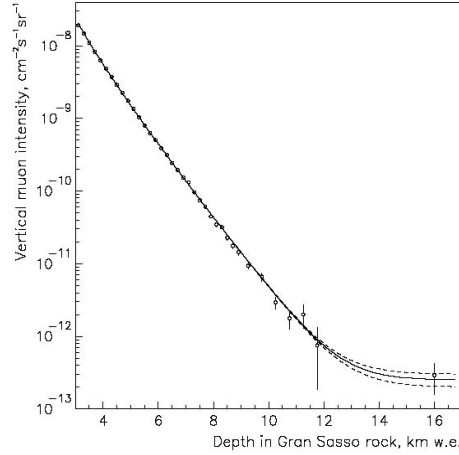


Figure 3.5: Depth vertical muon intensity relation in Gran Sasso rock measured by LVD collaboration. Solid curve is the best fit to the data. Dashed curves show the calculated intensities for maximal and minimal contributions from neutrino-induced muons.[AGL 99]

3.3 Cosmogenic Background in Borexino and CTF

The mountain structure above Gran Sasso laboratory allows the measurements of muons which traversed slant depths from 3 to more than 12 km w.e. The depths correspond to the mean muon energies at sea level from 1.5 to 40 TeV at zenith angles from 0° to 90°. In spite of the fact that the Borexino experiment is shielded by 1300 meter of Gran Sasso rock (3800 mwe), by what the muon rate is suppressed by a factor of 10⁶ compared to the sea level, the muon rate is still 1,16 $\mu/(m^2 \cdot h)$. Table 3.1 shows the expected muon event rates for the several parts of the detector.

Since muons, like discussed above, induce approximately 2 MeV per cm of their path length in the scintillator they can be easily distinguished from real neutrino events of some MeV. Thus the muons crossing the IV region (i.e. the muons having a great path length through the target scintillator) do not describe a dangerous background for the neutrino detection, unlike the muons crossing only the buffer region between the IV and the SSS. These muons do not induce scintillation light but only the much weaker Cherenkov

3.3 Cosmogenic Background in Borexino and CTF

Detector Regions	Muon Event Rate in μ/day
Inner Vessel (IV)	2025
Stainless Steel Sphere (SSS)	5150
Buffer Region between IV and SSS	3125
All Water Tank Region	9900

Table 3.1: Expected muon event rates for several detector regions of Borexino.[HAG 01]

light. Thus they can leave a total charge in the PMTs comparable with the charge of a neutrino event, and consequently be easily misinterpreted.

A second background source are neutrons. Neutrons underground arise from two sources, which are local radioactivity and cosmic-ray muons. Neutrons associated with local radioactivity are produced mainly via (α, n) reactions, initiated by α -particles from U/Th traces in the rock and detector elements. Neutrons from spontaneous fission of ^{238}U contribute also to the flux at low energies. The neutron yield from cosmic-ray muons depends strongly on the depth of the underground laboratory. It is obvious that suppression of the muon flux by a large thickness of rock will also reduce the neutron yield. The dependence, however, is not linear:

$$N_n(h) \propto \langle E_\mu(h) \rangle^\alpha \quad \alpha = 0.75 \quad (3.13)$$

Fig. 3.6 shows a comparison of simulated neutron yield data with experimental data in depths from 20 mwe to 5200 mwe [ARA 05].

There are several reactions which lead to neutron appearance. The main processes are:

- a) negative muon capture; this process occurs with stopping muons and plays a significant role only at shallow depth;
- b) muon-induced spallation reactions;
- c) neutron production by hadrons (and photons) in muon-induced (via photonuclear interaction) hadronic cascades;
- d) neutron production by photons in electromagnetic cascades initiated by muons.

3 Muons and Muon Induced Background in Borexino

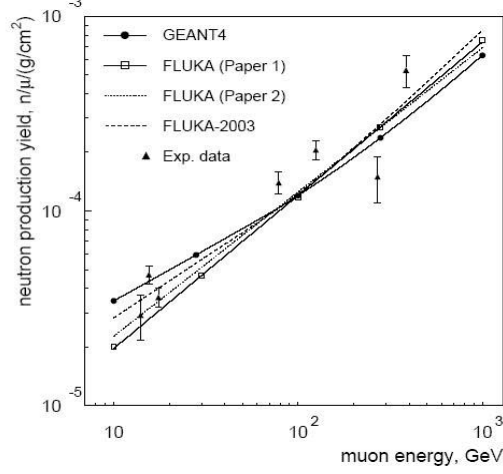


Figure 3.6: Dependence of the neutron yield per unit muon track length on muon energy for $C_{10}H_{20}$ scintillator. The experimental data represent measurements at depths varying between 20 m w.e. and 5200 m w.e. with the corresponding underground muon spectrum. Here they are plotted as a function of the mean muon energy.[ARA 05]

Most neutrons do not come directly from muon-nucleus spallation reactions, but from the muon initiated hadronic and electromagnetic cascades. The neutrons spread away from the primary muon track, thermalising slowly, and finally get captured by protons or other nuclei. Some, however, can strike a nucleus in the target volume transferring sufficient energy to be detected. Unlike charged hadrons which can be tagged by a veto detector system, neutrons can be identified by the released capture γ . In the case of Borexino the neutrons are captured in the scintillator or in the water buffer mainly by protons in the reaction.

$$n + p \rightarrow D + 2.2MeV\gamma \quad (3.14)$$

The average number of neutrons produced per muon per g/cm^2 of its path in liquid scintillator was found to be $(1.5 \pm 0.4) \cdot 10^{-4}$ neutrons/(muon event)/(g/cm²) by the LVD collaboration at the Gran Sasso underground lab [AGL 99].

From this neutron yield the muon induced neutron flux in Borexino can be estimated from:

3.3 Cosmogenic Background in Borexino and CTF

$$\langle N_n \rangle_{Borexino} = \Phi_\mu \cdot \rho_{PC} \cdot \langle L \rangle \cdot N_n(h_{LVD}) \quad (3.15)$$

whereby Φ_μ is the muon flux through the IV from table (3.1), $\langle L \rangle$ is the average path length of a muon through the scintillator and $h_{LVD} = h_{BOREXINO} = 3600 mwe$. This gives a flux of about:

$$\langle N_n \rangle_{Borexino} \approx 150 \text{ neutrons} / (d \cdot 300t) \quad (3.16)$$

which is in good agreement with data from the last CTF measurement period, as will be shown beneath.

Decay	Isotop	T _{1/2}	E _{max} (β^- , β^+)	+ E _{γ} , (BR)
β^-	¹² B	0.02 s	13.4 MeV (β^-)	
	¹¹ Be	13.80 s	11.5 MeV (β^-)	
	¹⁰ Be	1.5·10 ⁶ a	0.56 MeV (β^-)	
	¹¹ Li	0.09 s	20.8 MeV (β^-)	
	⁹ Li	0.18 s	13.6 MeV (β^-)	
	⁸ Li	0.84 s	16.0 MeV (β^-)	
	⁸ He	0.12 s	10.6 MeV (β^-)	
	⁶ He	0.81 s	3.5 MeV (β^-)	
β^+	¹¹ C	20.38 min	0.96 MeV (β^+)	+ 0.72 MeV γ , (98.53%)
	¹⁰ C	19.30 s	1.9 MeV (β^+)	
	⁹ C	0.13 s	16.0 MeV (β^+)	
	⁸ B	0.77 s	13.7 MeV (β^+)	
EC	⁷ Be	53.3 d		0.478 MeV γ , (10%)

Figure 3.7: All radioactive nuclides, which can be produced by muons or secondary particles in organic scintillator (C_nH_m)[HAG 00].

Another part of the muon induced background are the radioactive nuclides, which are produced by muons and secondary particles in the ¹²C target, which is the main component of organic scintillators. In fig. 3.7 is shown a list of all nuclides, which can be induced by high energy muons in organic scintillators.

The list includes the nuclides ⁸Li, ⁹Li, ⁸B, ¹²B and ⁹C, which have all mean lives below one second and are therefore easily taggable with the parent muon. ⁷Be is the cosmogenic radionuclide with the longest half life of

3 Muons and Muon Induced Background in Borexino

53.3 days. This radionuclide emits a γ of 0.478 MeV in an electron capture reaction with a branching ratio of 10%. This energy falls fully into the ${}^7\text{Be} - \nu$ window of 250-800 keV and is therefore, due to the long half life, an untaggable background. Also ${}^{11}\text{C}$ with its half life of 20.38 minutes does not allow identifying its decays by tagging it with the parent muon alone.

The energy deposition of the ${}^{11}\text{C}$ β^+ decay is the annihilation energy of 1 MeV plus the β^+ energy with an endpoint of 0.96 MeV. This energy falls into the pep- and CNO- ν window of 0.8 MeV - 1.4 MeV. Since the expected detection rate in this energy window is about 1 event/day, the background induced by the ${}^{11}\text{C}$ -decays might be substantial.

The inclusive cross section for the production of several cosmogenic nuclides in muon-induced cascades was measured by a target experiment on the SPS-muon beam at CERN [HAG 00]. The experiment used a liquid scintillator target. The muon showers were built up in 240 cm of concrete and 200 cm of water used as absorbers and placed in front of the ${}^{12}\text{C}$ targets. Two positively charged muon (μ^+) beams of 100 and 190 GeV were used in order to allow the determination of the energy dependence of the inclusive cross sections. By means of the cross section the muon induced background rates for the individual nuclides (see fig. 3.8) could be calculated.

The background rates of fig. 3.8 show that the contribution of ${}^7\text{Be}$ and ${}^{11}\text{Be}$ into the ${}^7\text{Be} - \nu$ detection window is negligible. However the ${}^{11}\text{C}$ rate overwhelms the expected ν -rate in the pep, CNO - ν detection window at least by a factor of 5. It becomes obvious that the intriguing measurement of the pep- ν and CNO- ν rate (see chapter 2.1) is only possible by means of a strong reduction of the muon induced ${}^{11}\text{C}$ -background. The ${}^8\text{B} - \nu$ detection window is dominated by the background from ${}^{10}\text{C}$ decays.

3.3.1 Measurement of the Muon Induced Background in the CTF III

In order to investigate the ${}^{11}\text{C}$ -background problematic the data of the before mentioned prototype detector CTF was searched for these hard taggable events. For the results of this section the last CTF data taking period of more than 600 days was used and the results are compared with the predictions of

3.3 Cosmogenic Background in Borexino and CTF

	Muon induced background rates in BOREXINO in counts/(d100t) for the relevant energy detection windows:			
Nuclides	Over-all energy region	250 keV < E < 800 keV ⁷ Be- ν region	0.8 MeV < E < 1.4 MeV pep- ν region	2.8 MeV < E < 5.5 MeV ⁸ B- ν region
¹¹ C	14.55 ± 1.49	0	7.36 ± 0.75	0
⁷ Be	0.34 ± 0.04	0.34 ± 0.04	0	0
¹¹ Be	< 0.034	$< 4.3 \cdot 10^{-4}$	$< 1.0 \cdot 10^{-4}$	< 0.01
¹⁰ C	1.95 ± 0.21	0	0	0.56 ± 0.06
⁸ Li	0.070 ± 0.017	$(2.5 \pm 0.6) \cdot 10^{-4}$	$(8.0 \pm 2.0) \cdot 10^{-4}$	0.020 ± 0.005
⁶ He	0.26 ± 0.03	0.040 ± 0.004	0.07 ± 0.01	0.011 ± 0.001
⁸ B	0.11 ± 0.02	0	$(3.3 \pm 0.6) \cdot 10^{-5}$	0.020 ± 0.004
⁹ C	0.077 ± 0.025	0	0	0.016 ± 0.005
⁹ Li+ ⁸ He	0.034 ± 0.007	$< 6.8 \cdot 10^{-4}$	$< 1.0 \cdot 10^{-3}$	< 0.014
Sum	~ 17.4	~ 0.38	~ 7.4	~ 0.65
ν -Rate (SSM)		~ 50	~ 1.5	~ 0.53

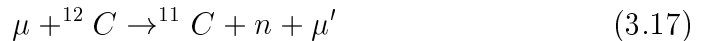
Figure 3.8: Muon induced background in count rates per day and 100t of liquid scintillator in Borexino[HAG 00].

3 Muons and Muon Induced Background in Borexino

the CERN muon beam experiment, mentioned above, and to results of the LVD experiment.

For a reliable detection of the ^{11}C -background a well understood muon veto is essential since the first tag of a ^{11}C event is the through going muon. Although being comparatively tiny (i.e. only 16 PMTs compared to 208 in Borexino) the CTF muon veto manages to exceed an 95% efficiency, which was proven in several water runs. During all the CTF campaign it was working highly reliable having only one PMT failure. Unlike Borexino the CTF detector is an open structure which has as an unavoidable result the impinging of scintillation light on the muon veto PMTs. This effect leads to a muon veto trigger probability for non muonic scintillation events, which obviously rises with the energy deposition inside the scintillator. In order not to lose efficiency it is necessary to use apart from the muon veto flag also a scintillator energy cut, which assures that the muon veto trigger was not set by an "ordinary" background event. Data analysis has shown that all registered events in the inner vessel over 4.5 MeV are fully assigned to muons. The efficiency of this cut is also very high since 4.5 MeV means as discussed before less than 3 cm muon path through the scintillator. Taking also the Cherenkov light detection in the water buffer, all muons passing the inner vessel are registered.

Muons which induce a ^{11}C nuclide in the scintillator do this by knocking off one neutron from the ^{12}C nucleus in the reaction:



The ejected neutron, which can have energies up to 10th of GeV, is moderated in the scintillator and after a certain path length (which can be up to 5m) is thermalized and captured by a hydrogen in the reaction (3.14). Being neutral the neutron is "invisible" up to the point when the 2.2 MeV γ is released. The energy deposition spectrum of the 2.2 MeV γ in the 2 diameter inner vessel is shown in fig. 3.9.

The reason why the spectrum is not only composed by a peak is the energy resolution of the detector and the escape probability of a 2.2 MeV γ , which results in a lower energy deposition inside the scintillator. The energy deposition of the 2.2 MeV γ was simulated [LEN 01] for a 1 meter radius

3.3 Cosmogenic Background in Borexino and CTF

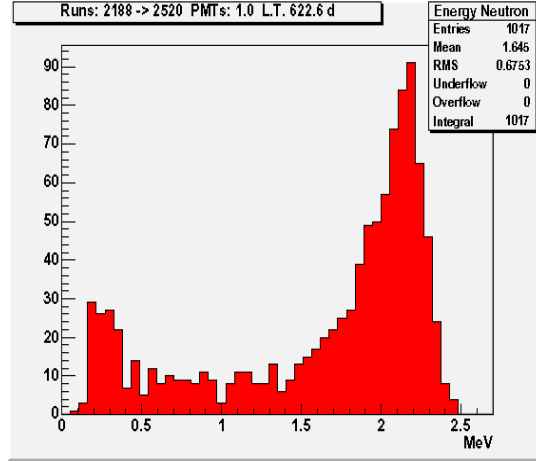


Figure 3.9: Energy distribution of the detected neutrons in 635 days of run-time of the CTF III period

spherical detector with organic scintillator. Table 3.10 shows the percentage of the energy deposition gained by the simulation as a function of the position of the n-capture.

In order to be sure not to lose any neutrons a time window of 2ms is opened after the muon tag, which corresponds to approximately 10 times the capture time of the neutron, shown in fig. 3.11, measured by the LVD collaboration [AGL 99].

A proof that the events shown in fig. 3.9 are unambiguous signs of neutron captures, gives a look at the time spectrum, see fig. 3.12 which agrees perfectly with the expected lifetime. Looking at the time between 2 and 4 ms after a muon event quantifies the random background contribution which is well below 1%. The measured neutron rate per day and 1 ton in the CTF is 0.4 events or $(1.5) \cdot 10^{-4}$ neutrons/(muon event)/(g/cm²). This is also in very good agreement with the LVD data shown above. Thus the neutron event (in fact the 2.2 MeV γ event) proved to be a reliable second tag for the ^{11}C detection.

As shown in fig. 3.7 the half-life of ^{11}C is with 20.38 min dramatically too long in order to be tagged directly in the data. The β^+ emitter with a minimum energy of 1.024 MeV and a maximum energy of 2 MeV generates the same detection signal as any background which has no fast daughter decay nuclide. The time window in wherein the search was carried out is 300

3 Muons and Muon Induced Background in Borexino

Percentage of energy deposition	Distance from center of the IV	0 cm	10 cm	20 cm	30 cm	40 cm	50 cm	60 cm	70 cm	80 cm	90 cm	100 cm
Energy deposition in keV												
0-200		1,39	1,44	1,62	2,06	2,65	3,65	5,31	8,11	13,05	22,51	42,75
201-400		0,42	0,44	0,48	0,57	0,69	0,84	1,13	1,52	2,06	2,9	4,22
401-600		0,4	0,42	0,46	0,52	0,61	0,76	0,96	1,22	1,51	1,84	1,92
601-800		0,43	0,44	0,47	0,54	0,64	0,8	0,98	1,23	1,48	1,65	1,3
801-1000		0,46	0,47	0,51	0,58	0,7	0,85	1,05	1,28	1,54	1,69	1,17
1001-1200		0,51	0,52	0,58	0,64	0,76	0,93	1,13	1,37	1,67	1,78	1,21
1201-1400		0,58	0,6	0,65	0,75	0,87	1,06	1,28	1,57	1,87	1,97	1,34
1401-1600		0,68	0,7	0,76	0,86	1,02	1,23	1,53	1,88	2,23	2,49	1,83
1601-1800		0,8	0,82	0,91	1,03	1,26	1,56	1,95	2,49	3,09	3,62	3,03
1801-2000		1,07	1,11	1,23	1,42	1,74	2,2	2,82	3,76	4,9	6,27	6,5
2001-2200		93,3	93,04	92,32	91,03	89,06	86,11	81,86	75,56	66,6	53,28	34,73

Figure 3.10: Percentage of energy deposition of a 2.2 MeV γ in a 1 meter radius detector with organic scintillator for several production distances from the center of the detector.

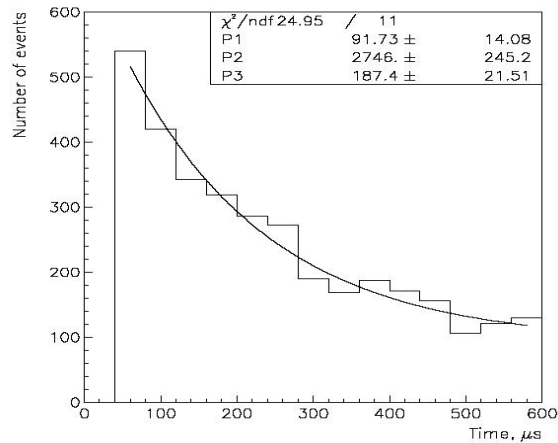


Figure 3.11: Time distribution of 2.2 MeV gammas from neutron capture by protons measured by the LVD collaboration.[AGL 99]

3.3 Cosmogenic Background in Borexino and CTF

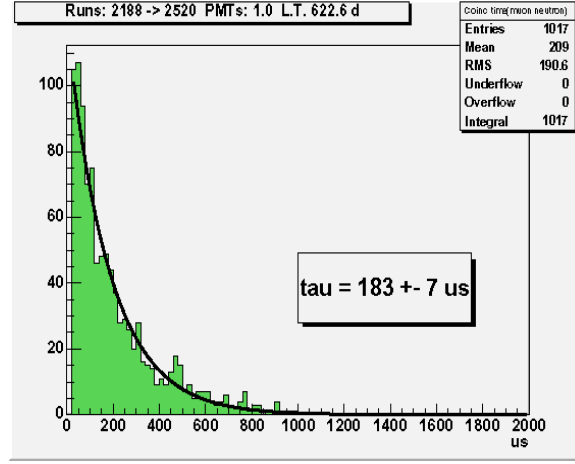


Figure 3.12: Coincidence time for the neutron capture in 635 days of run-time of the CTF III period

minutes after a reconstructed muon \rightarrow neutron event. In this energy window the amount of random spread background inside the detector is exceeding the amount of ^{11}C events by a lot. The only way to find a ^{11}C signals in the data is to analyze the time spectrum, which is shown in fig. 3.13.

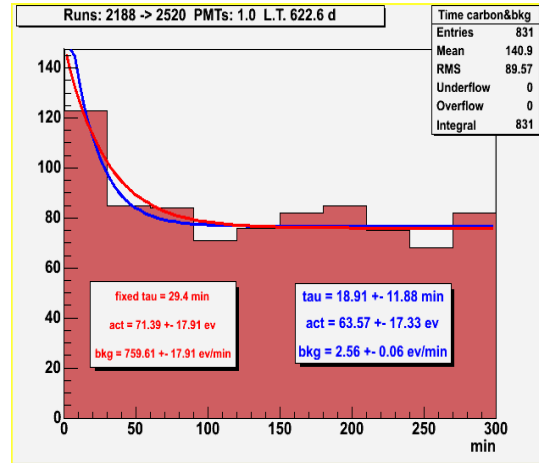


Figure 3.13: Coincidence time between neutrons and ^{11}C candidates or random background events in the inner one ton of the CTF detector

The red curve is an exponential function with the fixed mean live of the ^{11}C decay (29,4 min) plus a constant for the random background. For the blue curve the mean live τ in the exponential is let free. The result of the fit

3 Muons and Muon Induced Background in Borexino

is a τ which is smaller as the default value though it is not farther than one σ away from it.

In order to reduce the background it is possible to introduce an additional distance cut which takes into account that $\sim 20\%$ of the neutrons do not travel too far away (i.e. less than 25 cm) from their production point. A correlation between the space reconstruction point of the neutron capture and the ^{11}C candidate should reduce the randomly spread background if convection in the scintillator does not occur on the time scale of several hundreds of minutes. This assumption has already been proven to be realistic by the Kamland experiment. Fig. 3.14 shows the result of this analysis. A reduction of ^{11}C candidates of about 80% confronts a reduction of the random background close to 95%. The τ gained from the fit function corresponds well with the expected ^{11}C -lifetime. This result proves also that, like in the Kamland detector, convection in the CTF detector does not occur on the relevant time scale.

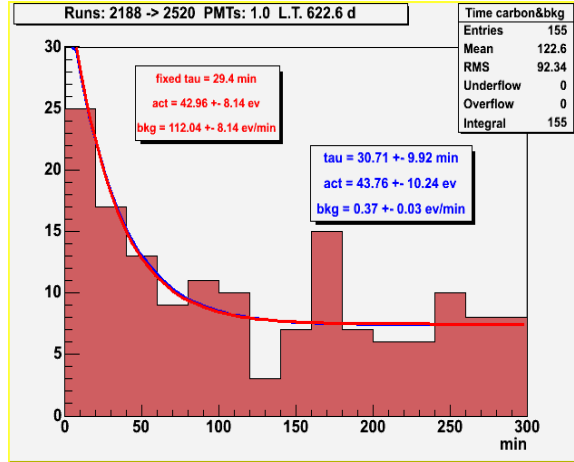


Figure 3.14: Coincidence time between neutrons and ^{11}C candidates in 1.77 tons of scintillator and 25 cm radial cut around neutron capture γ .

This three-fold analysis could clearly identify signs for muon induced ^{11}C candidates. Obviously this detection technique will be implemented in the Borexino experiment. However it is evident that a strong reduction of the ^{11}C , which is needed to have an acceptable signal to background ratio for the pep- ν measurement, is accompanied by a large introduction of dead detection volume. A method to reduce this dead detection volume will be discussed inter alia in the next chapter.

Chapter 4

Design and Simulation of a Muon Veto for Borexino

In the previous chapter the cosmogenic background was discussed and the necessity to have a system able to achieve a strong reduction of this background was pointed out. The first step in order to achieve this goal is to design a highly efficient muon veto system. Since one system alone is probably not able to reach an efficiency close to 100% a combination of three independently working systems was implemented to the Borexino detector out of which two will be presented briefly:

1. The inner muon detector

The inner muon detection system refers to the scintillator region inside the SSS. From the 2240 PMTs, which are responsible for the neutrino detection inside the IV 1866 are equipped with aluminum light concentrators [GRI 04]. These concentrators are shaped such, that they not only raise the amount of scintillation photons hitting the PMT cathode, but also accept only the light from the 300t scintillator inside the IV onto the PMT cathode. The remaining 374 PMTs are not equipped with light concentrators by what they permit also photons produced in the 1000t buffer region to be seen by the photocathode. Muons passing through the IV region produce such a big amount of light, that they are easily taggable. Unlike the muons crossing the IV region, muons passing through the buffer region produce mainly Cherenkov light since the wavelength shifter PPO is not added here. The much weaker amount of Cherenkov light can easily mimic the amount of light of a neutrino event

4 Design and Simulation of a Muon Veto for Borexino

especially when the muon path length through the SSS is short. The ratio between the light seen by the 374 PMTs without concentrators and the light seen by the 1866 PMTs with concentrators should be higher for muon events than for scintillation events.

2. The offline analysis

The offline analysis is based on a couple of detection techniques for separating offline neutrino events from muon events. The unambiguous muon evidence is the above mentioned energy cut. An other identification criteria is the average arrival time. Since β -events are quasi point like the photons arrive in a narrow time frame at the PMTs, unlike muon induced photons which are produced over a large path and thus can arrive in a time frame of up to 100 ns.

Both systems independently are able to separate muon events from β -events with an efficiency of over 95% each. Though being very efficient these systems alone still would not suppress sufficiently the muon background (3000 per day, see table 3.1) in the SSS. A third independent identification system is needed in order to reach the requested level of less than one misinterpreted muon event per day, which is equivalent to a combined efficiency of all systems above 99.99%.

4.1 Design Studies for the Outer Detector

The water buffer region outside the SSS is perfectly fulfilling the requirements of the third muon identification system. This "outer" region between the water tank wall and the SSS has an average wall to sphere distance of three meters thus providing sufficient space for the production of a large amount of muon induced Cherenkov photons. The average energy of the muons reaching the Borexino detector underground is with approximately 320 GeV by far above the threshold energy for the creation of Cherenkov photons in water ($n \sim 1.334$). The Cherenkov cone emitted by these muons has a flare angle which is given by:

$$\theta_C = \arccos\left(\frac{1}{n\beta}\right) \quad \beta \sim 1 \Rightarrow \theta_C \sim 42^\circ \quad (4.1)$$

4.1 Design Studies for the Outer Detector

The amount of Cherenkov photons emitted on a muon path length dx with the average energy of $\langle E \rangle = hc/2 \cdot \left(\frac{1}{\lambda_1} + \frac{1}{\lambda_2} \right)$ in the wavelength region of $[\lambda_1, \lambda_2]$ can be derived from:

$$\frac{dN}{dx}[\lambda_1, \lambda_2] = \int_{\lambda_1}^{\lambda_2} \frac{d^2 N}{dx d\lambda} d\lambda = 2\pi\alpha \left(\frac{1}{\lambda_1} + \frac{1}{\lambda_2} \right) \left(1 - \frac{1}{\beta^2 n^2} \right) \quad (4.2)$$

Taking into account the quantum efficiency of the PMTs, see fig. 4.1 the amount of detectable photoelectrons in the relevant wavelength window can be derived from 4.2 as $N_{pe} = 45$ pe/cm [HAG 00]. This means an amount of more than 10.000 photoelectrons per muon (for 100% coverage) which passes through the water tank and hits the SSS. Having a fixed amount of PMTs (~ 208) for the outer detector the goal is to spread these PMTs in the water tank such that they are able to detect as many photoelectrons as possible. The geometry of the Borexino water tank shown in 2.1 imposes spherical distributed PMTs around the SSS. The first approach to a muon veto design was to test several PMT positionings by means of a Fortran simulation based on the EGS simulation package.

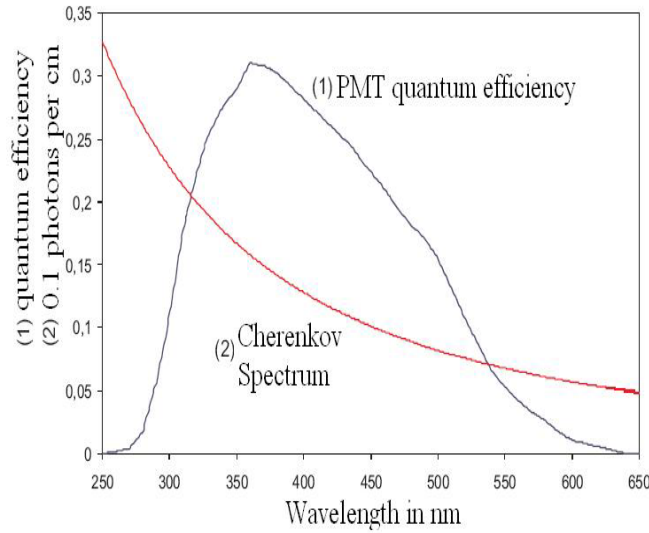


Figure 4.1: PMT quantum efficiency spectrum versus Cherenkov photon spectrum

The simulation is starting a muon at a random starting point in a random direction on the muon distribution measured by the MACRO collaboration

4 Design and Simulation of a Muon Veto for Borexino

at Gran Sasso [MIL 91]. Fig. 4.2 shows the lateral muon spectrum at the Gran Sasso laboratory.

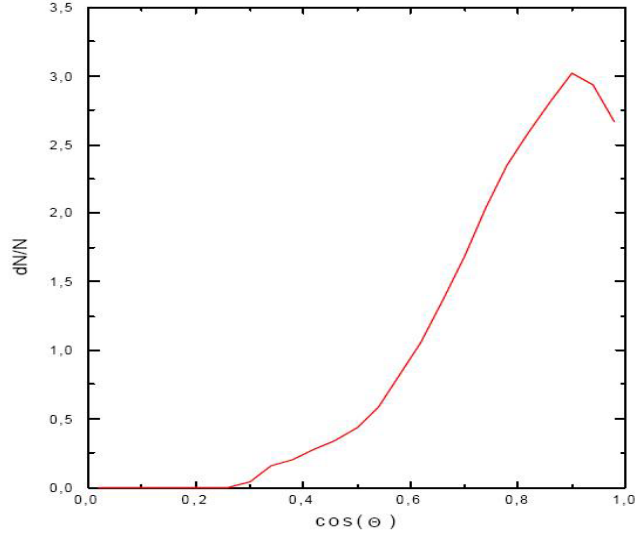


Figure 4.2: Lateral muon distribution at Gran Sasso laboratory [MIL 91]

The muon is followed inside the water tank until it leaves the water region. On every step of one cm a number of 45 photoelectrons is produced isotropic on a cone with a flare angle of 42° around the muon path. Every photon is traced until it hits a photocathode or it gets absorbed by the surfaces. The photocathode of a PMT has a surface of 0.03 m^2 thus all 208 PMTs have an overall detection surface of about 6 m^2 , which is approximately 1% of the SSS surface. The PMT positioning tested first was composed of 6 rings on the northern and on the southern SSS hemisphere respectively. The space between two rings is decreasing with the distance to the equator. The PMT distribution on the rings is shown in table 4.1.

Since the geometrical coverage of the SSS is at 1% only and thus most of the photons are absorbed before they can excite photoelectrons on the photocathode, the idea to use a reflective material inside the water tank was born. Tyvek, a white paper-like material, which was already used for the Super-Kamiokande experiment, was studied. The Tyvek material consists of $0.5\text{-}10 \text{ }\mu\text{m}$ thin polyethylene fibers, which are spun under pressure to $200 \text{ }\mu\text{m}$ thin lanes, and shows high reflectivity in the optical wavelength range (see fig. 4.3).

4.1 Design Studies for the Outer Detector

Ring number	Amount of PMTs
1	26
2	24
3	21
4	17
5	12
6	4

Table 4.1: PMT distribution of the outer detector on the rings around the northern part of the SSS. Nr. 1 is closest to the equator.

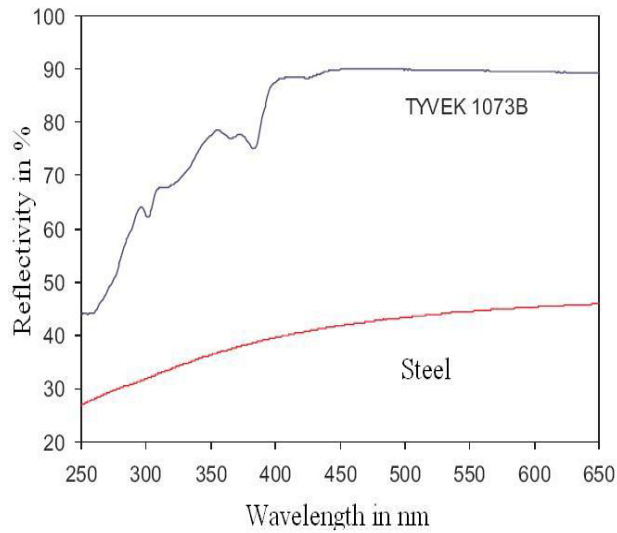


Figure 4.3: Wavelength dependent reflectivity of Tyvek and steel[HAG 01]

4 Design and Simulation of a Muon Veto for Borexino

Reflectivity in %	Detected pe	Triggered PMTs
0	64	4
20	92	20
40	129	37
60	210	64
80	445	126
90	904	185

Table 4.2: Dependence of the amount of pe and triggered PMTs per simulated muon from the surface reflectivity.

The coverage of the surfaces in the water tank breeds a significant increase of detected photoelectrons per simulated muon. The advantage of Tyvek becomes even more evident if the amount of triggered PMTs per muon is itemized like in table 4.2. This number depends strongly on the reflectivity inside the water tank. The amount of triggered PMTs per muon is the most important result, since the primary muon veto trigger depends on it (see chapter 5.2).

With an average reflectivity of 79% in the relevant wavelength window Tyvek confirms the expectation. With the use of Tyvek the muon veto efficiency is above 99%. Even in the case of over 20% broken PMTs the muon veto efficiency would not fall under 98% which is still above the request of 95%. Therefore the outer muon detector in combination with the above described inner muon veto and the muon offline analysis offers a reliable muon veto system, which is able to suppress the muon background in Borexino to less than one event per day.

4.1.1 Improvement of the Positioning

Having reached the request set for the outer muon veto, the next step is to use the simulation in order to study other features of this outer detector. Although the detector provides only a poor surface coverage it might be used for a muon tracking purpose. The idea is to find out which positioning of the PMTs is best in order to maximize the detected amount of direct Cherenkov light. Only the direct light can give a reliable information on the muon track through the water tank. In this scenario the Tyvek is interfering with the

4.1 Design Studies for the Outer Detector

tracking goal.

The lateral muon distribution in fig. 4.2 shows clearly that the muons are basically crossing the detector under a quite steep angle. Thus the best PMT positioning would be to arrange the PMTs such, that the photocathodes look mainly upward. The positioning with the spherical placed PMTs fulfill this requirement on the northern hemisphere only, while the southern hemisphere PMTs look basically downward and therefore see mainly reflected light from the Tyvek surfaces.

In order to improve the direct light yield 54 PMTs from the lowest 4 PMT rings of the southern hemisphere were placed on the water tank floor and on the wall. Fig. 4.4 shows the new PMT positioning with 4 PMT rings on the water tank floor and one ring on the water tank wall.

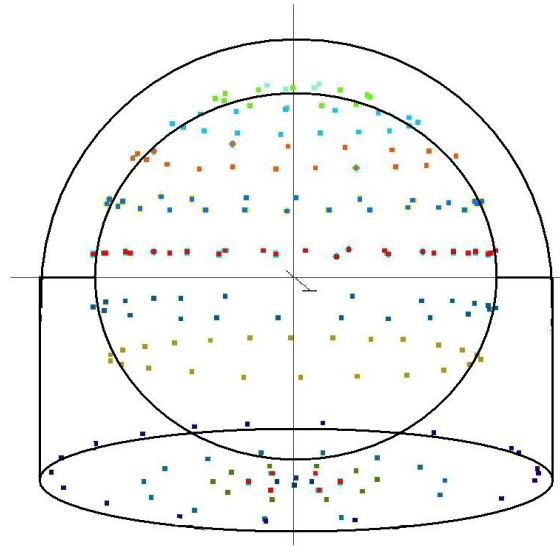


Figure 4.4: Improved PMT positioning in the water tank

Before testing the the power of the new positioning concerning muon tracking it is needed to prove the the displacement of the 54 PMTs does not degrade the muon detection efficiency. For both old and new PMT distribution a bunch of 100.000 muons were simulated and the results were compared. The results of this simulation is summarized in table 4.3.

The results have proven that the new PMT distribution reaches the same efficiency level concerning muon detection than the old one. The events

4 Design and Simulation of a Muon Veto for Borexino

	Old distribution	New distribution
mean # of pe per muon:	309.45	320.67
mean # of pmt hits per muon:	89.62	88.13
mean # of pmts in upper 8 rings:	64.55	64.49
mean # of pmts in lower 4 (5)rings:	22.97	24.39
mean # of pe in upper 8 rings:	263.28	263.18
mean # of pe in lower 4 (5) rings:	46.17	90.56
events with less than 6 PMT hits:	14	17
events with less than 10:	17	22
events with less than 20:	41	44
events with less than 10 pe:	16	21
events with less than 20 pe:	30	31

Table 4.3: Simulation results of the old and new PMT distributions

	Old distribution	New distribution
mean # of pe per muon:	81.45	120.88
mean # of pmt hits per muon:	12.62	15.29
mean # of pmts in upper 8 rings:	9.75	9.84
mean # of pmts in lower 4 (floor) rings:	3.22	5.95
mean # of pe in upper 8 rings:	76.08	76.97
mean # of pe in lower 4 (floor) rings:	5.37	43.91

Table 4.4: Simulation of both PMT distributions with surface reflectivity equal to 10%

with less than 10 PMT hits have an impact parameter which is considerably higher than the radius of the SSS, thus have only a small track length inside the OD. The amount of light seen by the PMTs distributed on the floor is considerably higher than the one seen by the PMTs distributed on the lowest 4 Rings of the SSS. The mean number of pe as well as the mean number of PMT hits increases with the new distribution.

The crucial point for the muon tracking is the direct light detection. To show the effect of the new distribution on the direct light detection, the simulation has been repeated with the Tyvek reflectivity set to only 10 % (i.e. almost no photons are reflected). Table 4.4 shows that the mean number of PMT triggered and the mean number of photoelectrons are significantly higher for the new distribution than for the old one.

4.2 Muon Track Reconstruction Study

In order to test the potential of the outer detector concerning muon tracking a GEANT4 simulation was accomplished. GEANT4 is a C++ based simulation tool, which offers the user a strong visualisation performance for testing the simulation code. The idea was to simulate the outer detector such that it agrees to the real one at a high level. Fig. 4.5 and fig.4.6 show the traces of the Cherenkov photons for two different muon tracks (muon track in red).

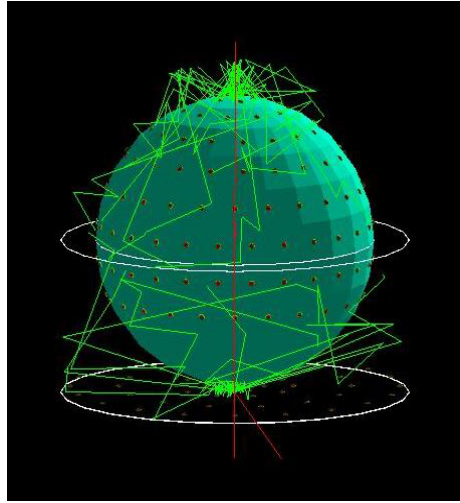


Figure 4.5: Cherenkov light for a simulated muon crossing the detector vertically through the center.

As discussed in chapter 3, the longer is the pass of the muon through the detector the more likely it is that it creates a shower and induces ^{11}C . Thus, muons with a small impact parameter (i.e. track is close to the center of the SSS) were detailed studied.

The Geant4 simulation provides information of the photon detection time (i.e. photon arrival time at the PMT), the total amount of photoelectrons for each PMT and the pe sum for each simulated muon event. All this information can be used at the reconstruction of the muon track. A precise reconstruction of the track can be used to apply a cylindrical volume around the track, which can be vetoed for several lifetimes of the ^{11}C . This cylindrical track veto can be combined with a radial veto around the reconstructed neutron capture position. In this scenario only the intersection volume needs

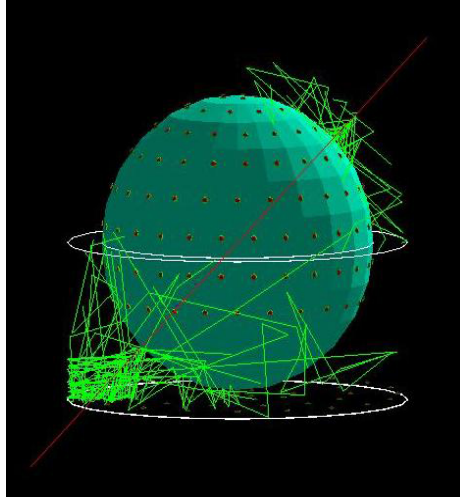


Figure 4.6: Cherenkov light for a simulated muon crossing the detector in an angle of 45° through the center.

to be vetoed. This scenario is depicted in fig. 4.7.

It becomes evident, a high precision muon track reconstruction is needed in order not to blind the detector with large veto volumes.

4.2.1 Muon Tracking Method

The analysis of the simulation information shows, that the arrival time of the first photon at the PMT is a reliable information concerning track reconstruction. In a first muon track algorithm only this information was used, since the energy information will be smeared off by electronic and calibration jitter effects. The time information is only influenced by the time jitter of the PMT, which is around 1ns. The time response of the first four triggered PMTs on the northern hemisphere and respectively on the southern hemisphere has proven to provide a reasonable good information of the muon track.

Fig. 4.8 shows the time response of the PMT nr. 3 on the northern hemisphere for two vertical muon tracks separated by 40cm. The two spectra are about 2ns apart not overlapping each other. The analysis has shown, that the track of muons, crossing the SSS, can be resolved down to 20cm.

4.2 Muon Track Reconstruction Study

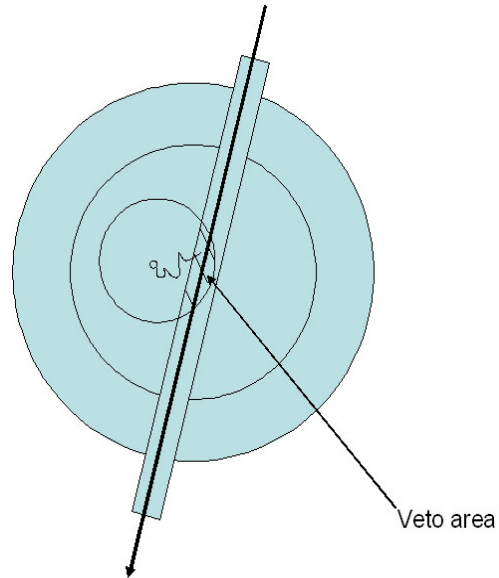


Figure 4.7: Intersection of radial neutron veto volume and cylindrical track veto.

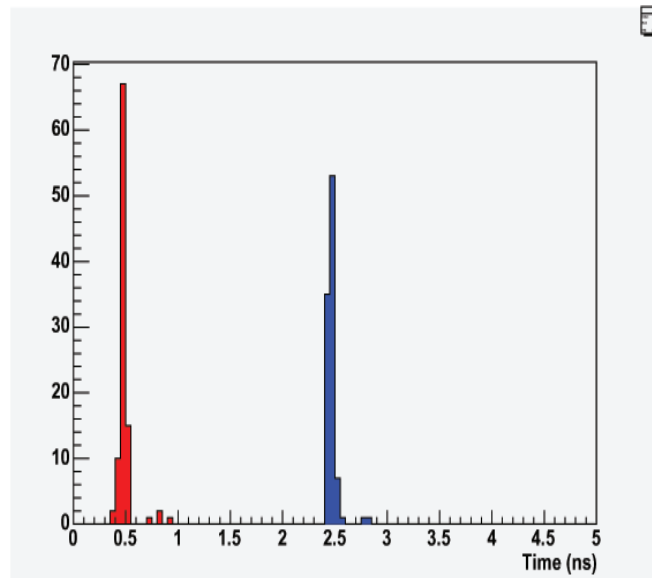


Figure 4.8: Time spectrum of the PMT nr. 3 for a muon passing vertically 10cm away from the center of the SSS (red) and 50cm away (blue)

4 Design and Simulation of a Muon Veto for Borexino

This allows to set an upper limit to the cylindrical track veto of $\sim 65\text{cm}$, which can be translated to a dead volume of $\sim 5\text{m}^3$ per tagged muon event.

Chapter 5

Achievement of the Borexino Muon Veto

After improving the muon veto simulation to a point which satisfies the muon background and tracking requirements of the Borexino experiment, a working Cherenkov detector is still a distant prospect. An enormous amount of technical questions have to be solved before even starting to install the outer detector. The installation itself is then a big organizational challenge. In this chapter the major technical attributes as well as the installation of the Borexino muon veto will be discussed. Although being designed for the Borexino experiment importance is attached to the fact that the tools and methods described in the following are suitable for future water Cherenkov detectors in general.

5.1 The PMTs and the PMT's encapsulation

The photomultiplier is an extremely sensitive light detector which acquire light through a glass or quartz window that covers a photosensitive surface, called a photocathode, which then releases electrons, due to the photoelectric effect, that are accelerated and focused onto the first dynode of an electron multiplier. Subsequently these electrons called photoelectrons are multiplied by electrodes known as metal dynodes whereby each electron on impact liberates a number of secondary electrons which are in turn, electro statically accelerated and focused onto the next dynode. The process is repeated at each subsequent dynode and the secondary electrons from the last dynode are collected at the anode. The ratio of secondary to primary electrons emitted at each dynode depends on the energy of the incident electrons as well as on the dynode surface properties and is controlled by the inter-electrode potentials. For a range up to 50 photoelectrons, the current flowing from the ground to anode is directly proportional to the photoelectron flux generated by the photocathode. The Borexino PMTs are operated in a single photoelectron mode (i.e. the operating high voltage is set such that the efficiency to measure one photoelectron emitted by the photocathode is about 60%).

There are several types of photomultiplier fulfilling different kind of detection condition, thus their attributes should be selected such that they best match the experimental requirements. The most important PMT attributes are:

- Wavelength dependent quantum efficiency of the photocathode;
- Glass radioactive background;
- Detection area;
- Dark noise;
- Transit time jitter.

For Borexino the spectrum of the scintillation light from a neutrino event is peaked around 400 nm. Low background glass is essential in order to keep the signal to background on a high level. In principal the detection

5.1 The PMTs and the PMT's encapsulation

area should be as big as possible to offer a bigger detection coverage but bigger photocathode geometries goes hand in hand with higher dark noises and higher expenses. Taking all this into account the THORN EMI 9351 photomultiplier was chosen. This PMT offers a 200 mm diameter detection area has a low background (300 kppm in K, U, Th) borosilicate glass and a bialkali photocathode sensitive in the light window from 350 to 500 nm. Several tests demonstrated the good behavior of this PMT type concerning low light condition, whereby the low transit time jitter of ~ 1 ns should be pointed out.

5.1.1 Motivation for a PMT Encapsulation

Since the Borexino PMTs are operated in scintillator and in water respectively, an encapsulation at least of the weakest parts (i.e. the electrical parts of the voltage divider) had to be designed. The PMT encapsulation design which was firstly used in the CTF I test stage comprises a stainless steel cylinder which surrounds the electrical parts of the PMT. The "Jupiter" connector which supplies the high voltage to the voltage divider exits the cylinder from one side. The other side is sealed at the neck of the PMT with a "master bond" resin. The head of the PMT with the photocathode which is at a ground level is not encapsulated at all. 100 PMTs were equipped with this encapsulation and were operated for several time under water. After one year of test period almost 50% of the PMTs were not working anymore. This devolution provoked a deep investigation concerning the weakness of the encapsulation design. The weak point was gleaned to be the connection between the under water cable and the connector, hence it was a problem of the encapsulation rather than of the PMT itself.

5 Achievement of the Borexino Muon Veto

5.1.2 Design

Unlike the encapsulation design for the inner detector the muon veto encapsulation design was commenced from a different perception. Instead of seeking weak encapsulation points one can completely encapsulate the PMT and the voltage divider. This has also the advantage, that the buoyancy force is not acting at the weak neck of the PMT, whereby the risk of PMT rupture becomes negligible. The encapsulation has to satisfy the following points:

- all connection points should be water tight;
- the encapsulation should resist a pressure of at least 2 bars (20 m water height);
- the whole photocathode area should be visible for Cherenkov photons.

In the following the encapsulation design of the muon veto PMTs will be discussed. A stainless steel cone see fig. 5.1, which contains in its lower part the voltage divider (which divides the high voltage into the different potentials for the dynodes of the PMT) and a so called B20-socket, into which the twenty pins of the PMT can be plugged, forms the main part of the encapsulation. The board with the voltage divider circuit is soldered to the opposite side of the B20-socket. A short coaxial cable connects this board to the Jupiter plug, which is lead through the wall at the bottom of the cone. The high voltage which arrives through the under water cable is provided to the PMT by this Jupiter plug, which forms the appropriate counterpart. All the parts connected to the cone like screws or the Jupiter connector are glued to the cone by a resin called MasterBond in order to guarantee water tightness. The B20-socket is held in place by filling the bottom part of the cone with polyurethane glue. All the necessary assembling steps up to here can be done without the PMT. So the risk of breaking a tube is excluded.

In order to shield the PMT against the earth magnetic field a μ -metal foil is inserted into the steel cone. After that the tube is simply plugged into the B20-socket, thus a simple replacement of the tube without destroying the encapsulation is always possible. A 3 cm layer of silicon gel is filled into the cone and acts like a redundancy material which encloses the PMT pins and

5.1 The PMTs and the PMT's encapsulation

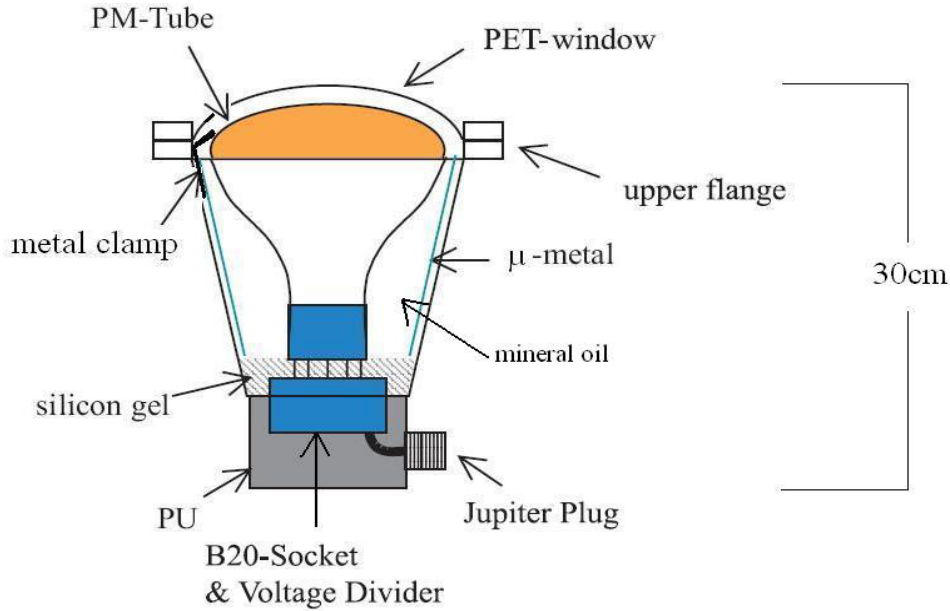


Figure 5.1: Parts and materials of the PMT encapsulation

thus ensures that, in case of water diffusing through the encapsulation, the PMT does not have a short circuit.

A polyethylene terephthalate (PET) foil forms the window of the encapsulation. The closed encapsulation is filled through a tube at its bottom with a transparent mineral oil, which acts like an optical coupling between the photocathode glass and the PET foil. This PET foil assures 4 major points:

- A water diffusion into the encapsulation, which could affect the PMT electronic is negligible;
- Acting like a membrane between the water outside and the mineral oil inside the encapsulation it compensates the outside pressure, thus the water buoyancy force acts on the whole tube and not on the weak encapsulation connections;
- It is compatible with water and organic liquids;
- It is highly transparent in the desired wavelength window crucial for the photocathode.

5 Achievement of the Borexino Muon Veto

The first and second points were proved in an extensive test discussed in the next section. The measured transparency of the PET foil is shown in fig. 5.2.

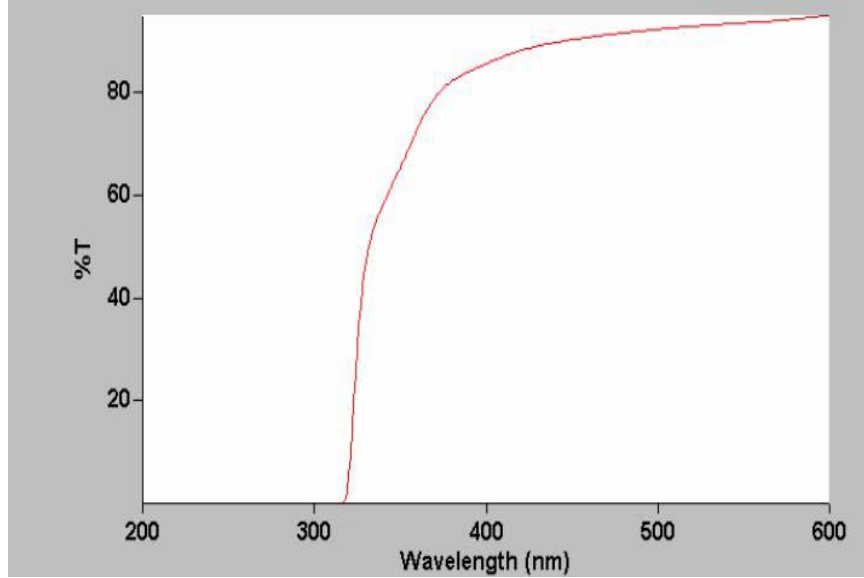


Figure 5.2: Transmission of the PET foil used for the PMT encapsulation

In the PMT relevant wavelength area the transparency of the PET foil is over 90% with an average of 92%. Moreover the PET foil acts like a wavelength shifter. The Stokes shift is the difference in wavelength between absorbed and emitted quanta. The emitted wavelength is longer (if single photons are absorbed) or equal to the incident wavelength, due to energy conservation. The difference is absorbed as heat in the atomic lattice of the material. If one conjures up the plot of the PMT quantum efficiency over the Cherenkov spectrum it becomes evident that this effect increases the effective average transparency, since the amount of Cherenkov photons decreases with the wavelength.

For having an accurate understanding of the influence of the PET foil on the PMT photoelectron efficiency a measurement was carried out by means of the calibration system of the outer detector (see chapter 5.4). The LED with a sharp wavelength window around 375 nm was sending single photons in a sub-Poisson manner (only some percent of the triggers excites a photon from the LED). The PMT has seen the photons from the LED one time without PET foil and the other time with PET foil in between the LED and the

5.1 The PMTs and the PMT's encapsulation

photocathode. Since no optical coupling medium between the photocathode and the PET foil was used reflection effects were expected. However the observed difference in photoelectrons for the two measurements for the same amount of triggers is only 7.5% which is already a hint for the wavelength shifting of the PET foil to the positive direction of the PMT quantum efficiency. Fig. 5.3 shows the measured arrival time of the photoelectrons. The time shift $\Delta t = (0.3 \pm 0.1)$ can be explained with a Stokes shift in the PET foil.

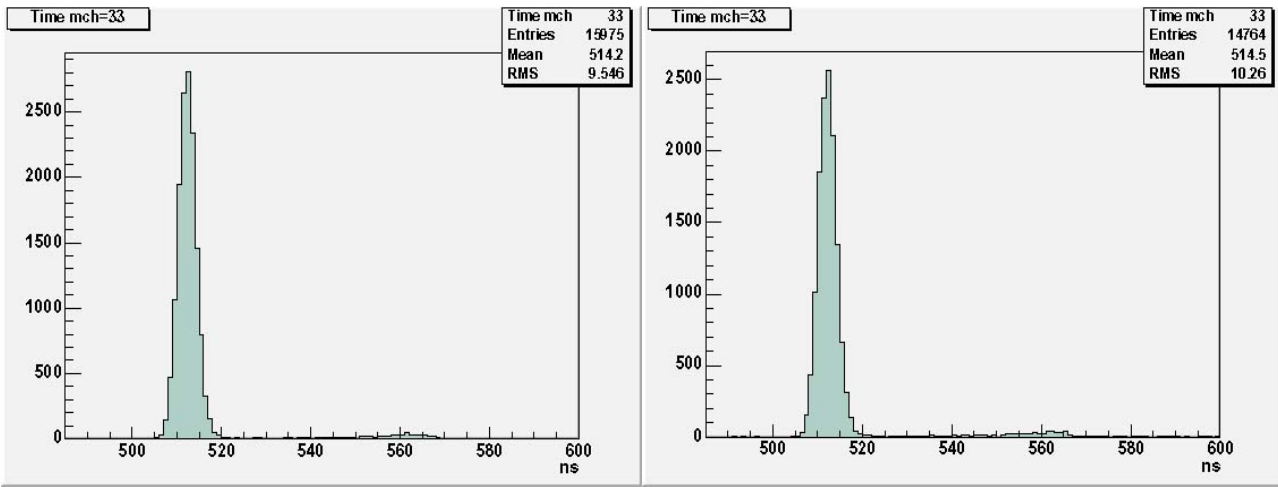


Figure 5.3: Measurement of the PET foil influence on the amount of photoelectrons (left without, right with PET foil)

Having experienced a detach of the PMT pins from the B20-socket due to buoyancy in oil during the CTF II period 3 clamps are used to create a pressure on the PMT which is enough to avoid contact breakup.

The remaining space between tube, cone and PET foil is filled with mineral oil, which is transparent in the necessary wavelength region and serves as an optical contact medium between the PET foil and the photocathode. The electric resistance of the oil is infinite, so no problem arises even if the oil had direct contact with the pins of the PMT. Since the oil filling of the encapsulation is not trivial concerning release of the air from the inside of the encapsulation, a method was applied at which the oil was filled through a small hole in the bottom of the cone. A small tube which is fixed during the gluing of the B20 socket with polyurethan serves as a filling pipe for the oil. The remaining air is released by opening one or two screws on the top flange.

5 Achievement of the Borexino Muon Veto

By this method the dimension of the air bubbles which remain inside the oil is very small, thus leading to a tiny loss of efficiency due to refractions. An accomplished encapsulated PMT is shown from the top in fig. 5.4.

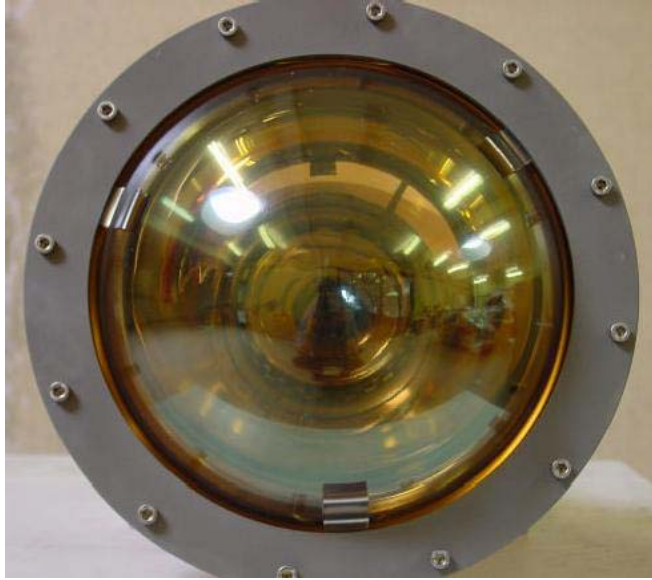


Figure 5.4: The encapsulation seen from the top

5.1.3 Testing

In order to assure the functional efficiency of the above described design, all encapsulated PMTs have been exposed to several test stages before being released for the installation in the muon veto. These can be resumed as follows:

- Each PMT arrived from ETL is connected to high voltage and tested for functionality in a dark room box;
- The resistors of each B20-socket are tested for the right values;
- After the connection of the B20-socket with the Jupiter connector the resistors are cross checked for assuring a reliable soldering;
- The accomplished encapsulation without PMT is set into a water bath in order to see air bubbles from untight encapsulation;

5.1 The PMTs and the PMT's encapsulation

- Only into the tight encapsulations the PMTs are inserted and brought to a test facility.

A test facility was produced in order to assure the water tightness and the pressure resistance of each encapsulated PMT. This test facility shown in fig. 5.5 allows the parallel test of 21 PMTs on 3 levels. After covering it with a steel dome it is filled with water and set under a pressure of over 2 bars which corresponds to the water pressure on the bottom of the Borexino water tank. The released water after the test was checked for oil residual which would have been a sign for untight encapsulations.

The PMTs are connected during this test to high voltage with the same cables used for the outer detector thus a leakage in the connection could be tested simultaneously.

For having a long term test stage the first 21 encapsulated PMTs were tested for 6 month in the pressure tank under water and with high voltage on. In this way problems connected with the encapsulation would show up yet no serious one became apparent. Thus having proved the reliability of the encapsulation design a mass test was performed whereby each PMT passed through a test period of 5 days in the test facility.

Only 12 PMTs out of 230 encapsulated didn't receive the certification for the transport to Gran Sasso due to failure reasons during the encapsulation process.

5 Achievement of the Borexino Muon Veto

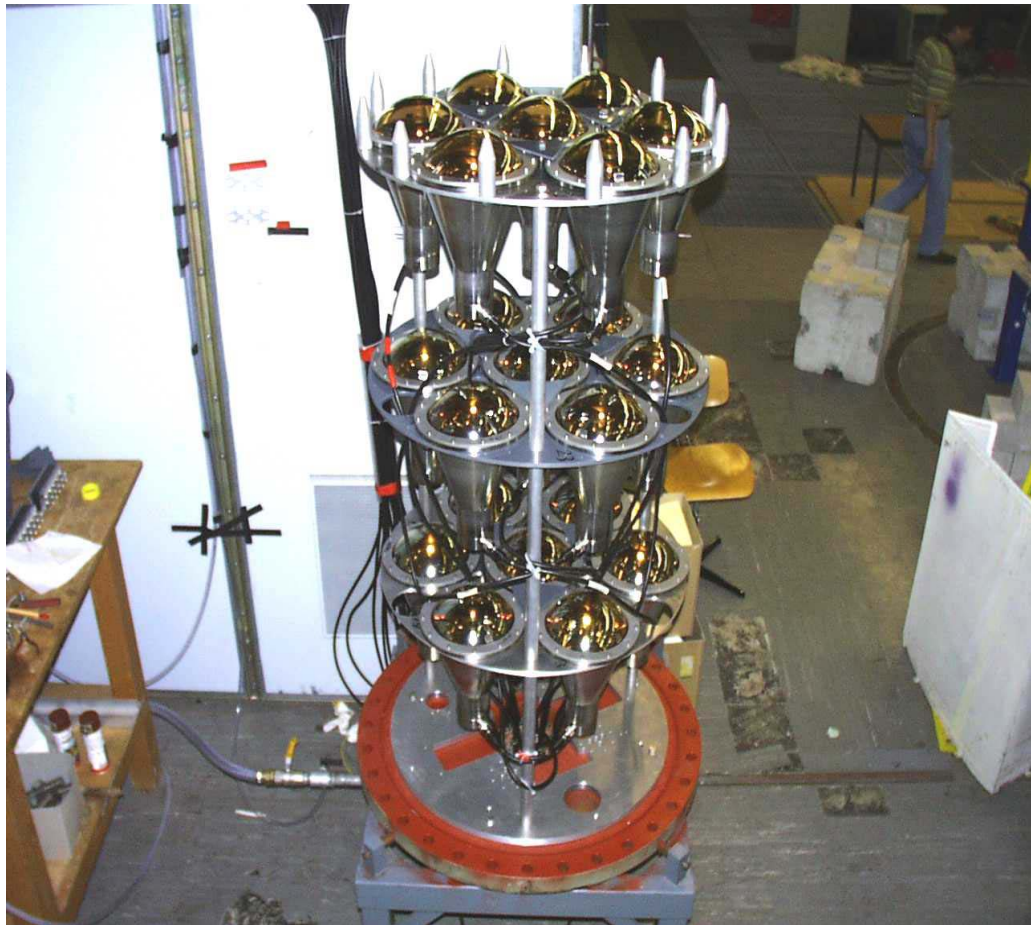


Figure 5.5: Munich PMT encapsulation test facility with 21 PMTs inside. The dome which encloses the facility tightly is not shown.

5.2 Schematic of the Muon Veto Electronics and DAQ

The electronics of the Borexino detector was briefly described in paragraph 2.3. As mentioned above the goal of the muon veto is not only providing an efficient muon veto tag for the Borexino inner detector but also enabling a muon track reconstruction. As a consequence therefore an accurate measurement of the Cherenkov photoelectrons over a larger range than for the inner detector triggered the design of an electronic unequal to the inner detector one. Since the photoelectron charge signal is integrated, as will be described below, on the QTC boards which have as one output a time signal proportional to the PMs charge, the information about the muon events comes only from the Time to Digital Converters (TDC)s.

5.2.1 Decoupling the Fast PM Pulse

Since the inner and outer PMs are supplied with high voltage through the same cable where the signal of the PMs is received a decoupling of the fast signal from the high voltage has to be carried out. Nine high voltage decoupling units (HVD) with 24 channels each serve this purpose. Each channel consists of 1 input one 1 input/output and one output line. A schematic of a HVD channel is shown in fig. 5.6.

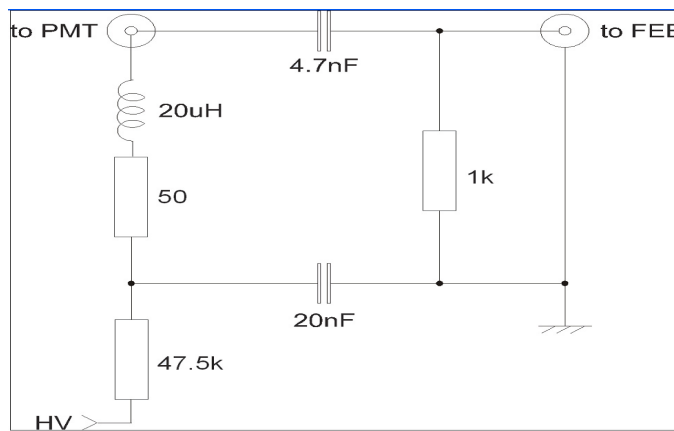


Figure 5.6: High pass circuit decoupling the PM pulse from the high voltage

5 Achievement of the Borexino Muon Veto

A high pass filter with 50 Ohm matching at all frequencies is used. The high pass filter, composed by the 4.7 nF capacity and by the 50 Ω impedance, is balanced by the parallel circuit composed by a 20 μ H inductor and a 50 Ω resistor. Two 47.5 k Ω resistors are in use: the first is connected between the HV line and the 20 nF blocking capacitor. The second (not pictured) is connected in parallel with the 50 Ω termination resistor of the HVD in order to prevent the possibility of building up a high voltage on the center conductor.

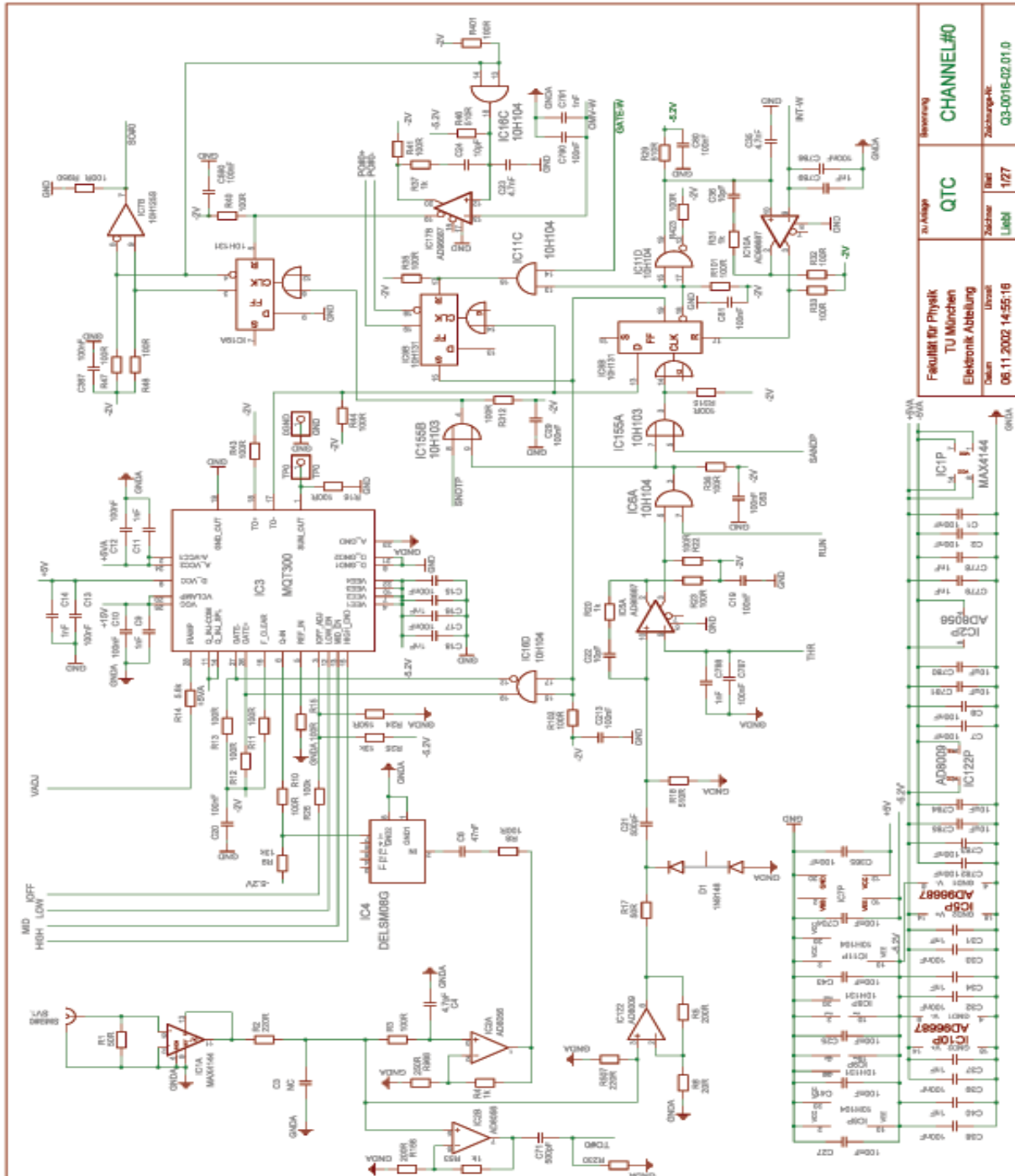
The high voltage (HV) line is an only input line. It transmits the HV generated from the CAEN SY257 HV units to the HVD. The PMT line is an input/output line. It transmits the HV from the HVD to the PMT. It also transmits the PMT fast pulses to the HVD. The signal line is a only output line. It transmits the AC decoupled fast PMT pulses to the Charge-to-Time Converter boards (QTC).

5.2.2 Charge to Time Converters (QTC)

Although the Charge-to-Time Converter boards (QTC) (see fig. 5.7) are self-made Versa Module Europe (VME) electronic boards there is no communication between them and the VME PowerPC (PPC) through the VME Bus. They receive as input the photomultiplier signals coming from the HVD boards with coaxial cables matched at 50 Ohm whereby the cables are provided with SMB connectors. Therefore the boards are equipped with 16 SMB receptacles. The PM signal is processed in 14 QTC boards with 16 input and 3 output channels each. A description of this 3 outputs is given in the next paragraphs.

The primary output (PO) of the QTC is a logic (differential ECL) pulse whose width is proportional to the charge of the input pulse. The first edge of the pulse gives the time of the arrival of the photoelectron(s). The time difference between the two edges is a sum of an offset and a part which is directly proportional to the integral of the photoelectron(s) charge. This integral is provided by a LeCroy MQT300 chip which performs a on-board charge -to-time conversion. Each channel of a QTC board has its own dedicated MQT300 chip. When a discriminator associated with a channel has fired the LeCroy MQT 300 chip is activated and the output pulse is issued,

5.2 Schematic of the Muon Veto Electronics and DAQ



03.05.2005 15:03:01 f=0.71 E:\Test\qtc5.sch (Sheet: 1/27)

Figure 5.7: A channel of the QTC board with one input channel (SMB-connector) and three output channels (PO,SO,TO)

5 Achievement of the Borexino Muon Veto

whereby the threshold for the discriminator is set able and given by a voltage reference level common to all the on-board channels and derived from the bussed line THRESHOLD. The integration gate of the MQT300 can be set in the range 60-150 ns and tuned by a voltage reference level common to all the on-board channels and derived from the bussed line INT_WIDTH. The offset has a fixed time width, corresponding to the time necessary for the MQT300 to perform the integration and any other processing of the input pulse. On the other hand, the output of the MQT300 chip is directly proportional to the charge of the input pulse. Therefore, the time width of the PO is a linear function of the input charge of the pulse. The gain of the MQT300 chip is defined as the constant slope of the linear function relating the input charge and the output pulse time width. A mass test, which was done in order to prove the linearity of this gain, showed no significant nonlinear aberration. The gain of the MQT300 is given by two voltage reference levels common to all the on-board channels, and derived from the bussed lines VADJ and IOFF. The connector used to transmit all the PO lines is a 34-pins, 4-wall, right angle header, with lock-and-eject levers. From the PO of the QTC the ECL digital pulse is forwarded to the TDC units (CAEN V673, 128 channels/unit, multihit and multievent). Two TDC units are used for the 208 PMs.

The secondary output (SO) is a logic signal going to the Muon veto Trigger Board (MTB). The logic signal is a step function of the number of channels fired in a certain time window. The step function is built with analog sums in a totally asynchronous way, no clocks being used. The height of each step is 100 mV. After the PM pulse has exceeded the threshold of the discriminator of a channel, a latched differential ECL pulse is generated by means of a network composed of a flip-flop and a comparator. The length of the latched pulse can be set in the interval 60-240 ns, and it is given by a voltage reference level common to all the on-board channels and derived from the bussed line OMV_WIDTH. Simulations have shown that a length of 150 ns achieves the requirements of this trigger pulse (i.e. 99% of all photoelectrons of one event are triggering the SO in a time window below 150 ns). All the 16 on-board latched pulses obtained are summed together in a single instance (see appendix 1). The secondary output is taken directly from the output of the summing instance.

The tertiary output (TO) is the analog sum of the PMs signals at the

5.2 Schematic of the Muon Veto Electronics and DAQ

input of the board. A copy of the signal coming from the PMs is derived after an on-line buffer and sent directly to the OMV_ASUM instance, where an analog sum of the 16 signals from the 16 channels is performed. The purpose of the tertiary output is to build a backup trigger module. Simulations have shown that muons having a very short pass through the detector (i.e. passing only very close to the water tank wall or through one of the water tank legs) often trigger only a few PMs. In case that the multiplicity coincidence of triggered PMs should be raised to a certain value (i.e. 6 PMs), it is possible to set a threshold on the total charge collected by using the TO. The TOs of all the QTC boards are added together using NIM modules. The sum is sent to a NIM discriminator, and the output of the discriminator will be sent directly to the Borexino Trigger Board (BTB). The Borexino Trigger Board can handle the two trigger signals, the one built from the SOs of the QTCs by the MTB and the one built from the TOs of the QTCs with NIM modules.

5.2.3 The Muon veto Trigger Board (MTB)

Unlike the QTC boards the MTB communicates with the PPC through the VME bus. With other modules it communicates through cable lines. It receives inputs from the QTCs boards, from the Borexino Trigger Board (BTB), from the TDCs, from the PPC and from the System Clock. It sends outputs to the BTB, to the TDCs and to the PPC. The MTB sends bussed signals to all QTC boards (i.e. the control busses of the QTC boards) in the crate to control their mode of operation. The SO (i.e. the number of channels fired in a certain coincidence time window) of the QTCs is the input of MTB. The input from the PPC is the number of channels in coincidence required to set the trigger condition for the outer muon detector (Outer Muon Trigger, OMT). The MTB sets the OMT in case of a coincidence of $\#x$ channels fired in $\#y$ nanoseconds. The number $\#x$ can be programmed on the MTB by the PPC in the span from 0 to 32, whereby $\#y$ cannot be programmed on the MTB and it is set directly on the QTCs by the voltage of the bussed line OMV_WIDTH, as described above.

The Borexino General Trigger (BGT) is defined as a general trigger for all the Borexino sub detectors (inner neutrino, outer muon), (i.e. only a BGT initiates the readout of the outer muon detector). The only board in charge

5 Achievement of the Borexino Muon Veto

of generating a BGT is the BTB (see chapter 2.3). When the BTB receives a OMT from the MTB, it always sets the BGT. After the MTB receives a BGT it sends it daisy chained to all TDCs as a common stop signal for them. The PPC is reading the data from the TDCs buffers after they have issued a VME interrupt. Data are sent then via TCP/IP to the main DAQ storage area.

Since the depth of the TDCs buffer is of 4 events, and the expected time for unloading the buffer is of the order of tens of microseconds, it is very unlikely that in any case of physical interest the TDCs buffer will be completely filled (i.e. more than 5 BTG triggers in less than 50 microseconds). Anyway, if TDC buffer is completely filled, the BGT must be vetoed up to when at least a portion the TDCs buffer is unloaded (otherwise, the synchronism between inner and outer detector will be lost). For that reason an input to the MTB is the BUSY signal which is provided by the TDC control bus, collecting the daisy chained signal from all the TDCs in use.

5.3 Dark Noise Measurement

For setting the right number $\#x$ of PMTs firing simultaneously to the MTB an accurate knowledge of the PMTs dark current rates (dark noise) is needed. The dark current is the current associated with a PMT during operation in the dark with an applied voltage. The dark noise has different origins:

1. Thermionic emission In the absence of light falling on the cathode electrons have a certain probability of being emitted due to their thermal energy. Increased temperature and applied voltage will result in increased dark current. Also, larger active areas will generally have a higher dark current.
2. Cerenkov radiation and Cosmic Rays As described above the outstanding part of the cosmic radiation at the experiment site are muons. Since these particles are relativistic they emit Cerenkov radiation on passing through the pm faceplate. This gives rise to a dark current contribution though at the experiment site being tiny.
3. Background Radio-isotopes From the glass window and the environment. (^{40}K , ^{238}U , ^{232}Th)

4. Generation of light in the photomultiplier

- i) by ionisation of residual gases
- ii) or by electrode glow

The total dark current would thus be the sum of the currents from these different sources whereby the dominant contribution is delivered by the thermionic noise.

5.3.1 Requirements

Each PMT has a slightly different dark noise behavior. Monitoring this behavior is mandatory in order to keep the detector efficiency on a high level (i.e. avoiding random coincidences though keeping the number $\#x$ of PMTs firing simultaneously as low as needed). The probability for a single PMT of random coincidences due to dark noise f_{dark} in the time window τ can be expressed by

$$p_{rndm1} = f_{dark} \cdot \tau \quad (5.1)$$

and the total amount of dark noise counts depends on the amount of triggers which for Borexino is expected to be at the order of 10^5 per day is

$$N_{rndm} = N_{trig} \cdot p_{rndm1}. \quad (5.2)$$

Thus a single PMT with a dark noise of 10 kHz has a probability of random coincidence in a time window of $\tau=150$ ns of $1.5 \cdot 10^{-3}$ (i.e. it would cause approximately 150 random triggers per day). In order to avoid these false triggers it is required to set a certain number $\#x$ of PMTs which should fire simultaneously to obtain true triggers. On the one hand the $\#x$ should be big enough to reduce the false triggers down to less than one per day but on the other hand $\#x$ should not be set to a bigger value than mandatory in order not to lose true triggers. The probability for x PMTs of random coincidences due to dark noise in the time window τ can be expressed by:

$$p_{rndx} = 1 - \sum \binom{208}{k} f_{rndm1}^k (1 - f_{rndm1})^{208-k}, \quad k = 0, 1, \dots, x \quad (5.3)$$

5 Achievement of the Borexino Muon Veto

Since the average dark noise of the muon veto PMTs is of the order of 10 kHz, setting a threshold $\#x$ of 6 PMTs out of 208, is enough to keep the number of random triggers as low as 1 per day. However it is well known that the dark noise of a PMT changes over the years. This change is usually small compared to the total dark noise of the PMT but also PMTs starting suddenly to flash (i.e. having dark currents of the order of 200 to 500 kHz) have been observed during the years of CTF measurement. One flashing PMT would raise the average dark noise of the detector from 10kHz to about 12kHz and would consequently make it necessary either to shut it down or to raise $\#x$ from 6 to 7. Therefore a repeated dark noise measurement before starting a real run is needed in order to know the "health" of the detector. Since a big amount of commercial electronic scalers would have been needed for 208 PMTs one has chosen custom-made scalers for the muon veto.

5.3.2 Dark Noise Scalers

Four custom-made Dark Noise Scalers (DNS), each comprising 64 channels, were produced by the Moscow Marathon Institute and are NIM modules each consisting of

- * one mother board,
- * four daughter boards with 16 channel ECL receivers,
- * one control/indication daughter board,
- * one power supply board,
- * two CAN-bus internal interface cables.

The basic idea was to pick up the digital ECL signals from the QTC boards without disturbing it.

The digital ECL signal of 16 PO channels from one QTC board passes to one of the 4 input connectors of the ECL receiver daughter board of the DNS. This board converts the ECL signals to TTL. Subsequently the 16 TTL signals are relayed to one of the four FPGA (Altera EPM3512A) processors which is able to count individually the incoming TTL pulses of 16 channels and to store the data in an internal buffer. The clock frequency of all four FPGAs are given by a common 20 MHz oscillator.

5.3 Dark Noise Measurement

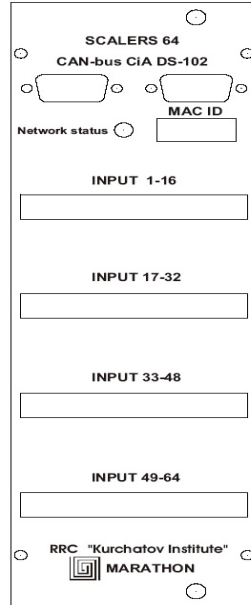


Figure 5.8: Front panel of the muon veto DNS

One of the four FPGAs generates a 20 Hz internal interrupt called (CNT_NT) to initiate the procedure of data reading from all FPGAs. The 20 Hz interrupt initiates the read out procedure of the firmware of the microcontroller (Fujitsu MB90F543 DD1). 16 channels are read out in parallel from four FPGAs one by one and the data is stored in an internal buffer. After the data is averaged per one second it becomes ready for being sent by the slave net device to the host computer via a CAN-bus line. The master net device requests data every second from each of the four DNS modules.

The MAC ID address, which defines the number of the module in the net device network is settable by a DIP switch. To watch the state of the module operation red/green LEDs are used. The DIP switch and the LED are installed on the control/indication daughter board which is soldered to the mother board.

An additional power supply board is used to convert the standard NIM crate power voltages to the voltages necessary for the mother board operation. As input from the NIM crate the power supply board has +6V, +12V, -12V which it converts to +5V, +8V, -8V.

A trigger generator module is used for testing purpose. Also the generator

5 Achievement of the Borexino Muon Veto

consists of 4 times 16 channels but unlike the DNS module the channels are ECL outputs of fixed frequencies. It uses the same kind of mother board without microcontroller and with different schematic of the FPGA.

Test efforts were done before the DNS were adopted in the muon veto electronic in order to demonstrate that the parallel pick up of the signal doesn't spoil it at all. After demonstrating this another test proved the correct counting of the dark noise signals in the scalers. A visualisation tool shown in fig 5.9 was created in order to give a fast understanding of the dark noise of every muon veto channel. The caption is illustrating the dark noise rate of each PMTs by colors whereby each channel is represented by a colored square. Two scaler modules were operated here simultaneously.

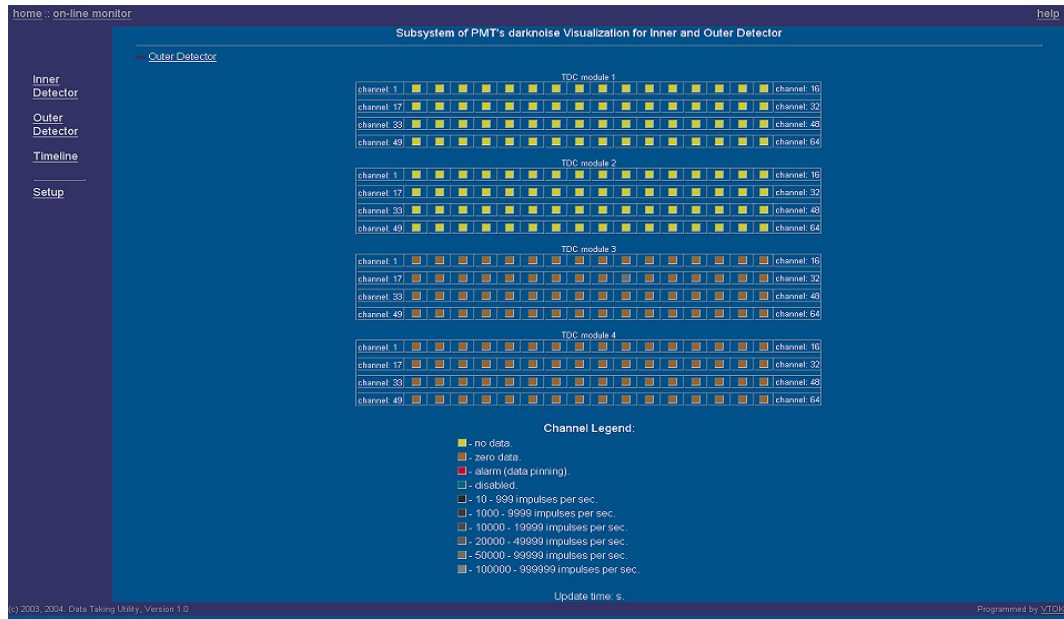


Figure 5.9: Outer Detector DNS visualisation with dark current caption

Clicking on a certain square leads to an individual outer detector channel. This is shown in fig 5.10.

The lower window shows the evolution of the dark current in time. Since the measured PMT was shortly before the run exposed to light the decreasing of dark current by time becomes apparent. The right window shows the distribution of the dark current since the beginning of the run. The same run is shown in fig. 5.11 but now reconstructed with the muon veto data ac-

5.4 The LED Calibration System

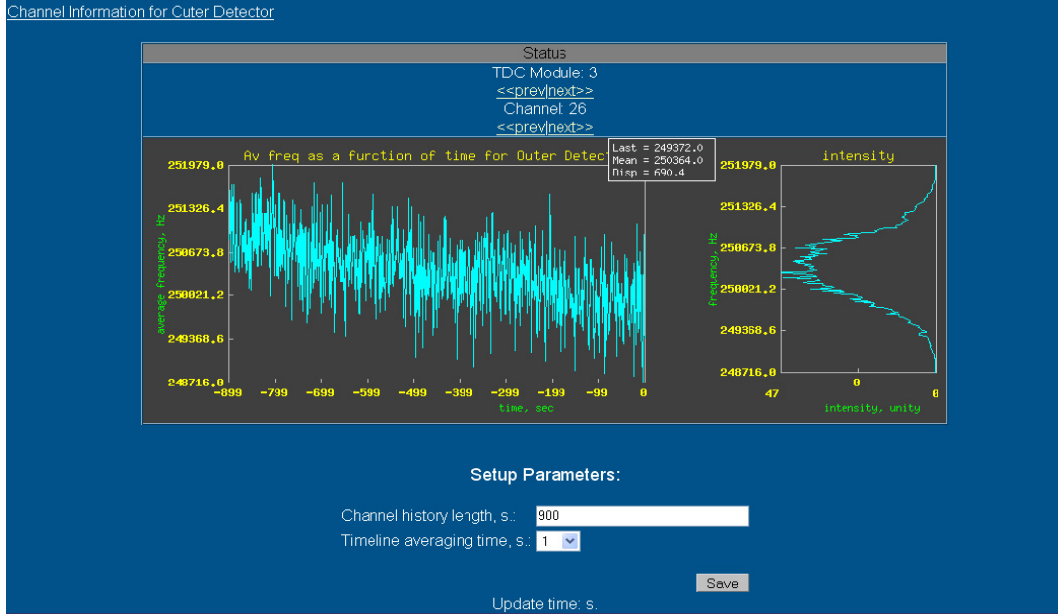


Figure 5.10: Dark noise visualisation of an individual channel during Run condition [SAB 05]

quisition system. 100.000 generated random triggers were analysed. Taking into account a trigger window of $8.533 \mu\text{s}$ the reconstructed dark noise rate is 243 kHz which matches precisely the 250 kHz of the scaler module.

The advantage of having a scaler system which works with digital input pulses is obvious. Firstly, due to the parallel pick up, it doesn't influence the signal from the QTC boards at all. Secondly it doesn't use any internal threshold thus the discriminator threshold of the QTC boards is the same as it is for the scaler modules.

5.4 The LED Calibration System

Unlike the inner detector PMTs which in average see only a fraction of photoelectron per event the outer detector PMTs have to deal with up to 1000 photoelectrons induced by the Cherenkov light of an incoming muon. As former discussed the muon veto electronic differs from the inner electronic in order to handle this condition. Thus an autonomous calibration system for the muon veto was designed, tested and established.

5 Achievement of the Borexino Muon Veto

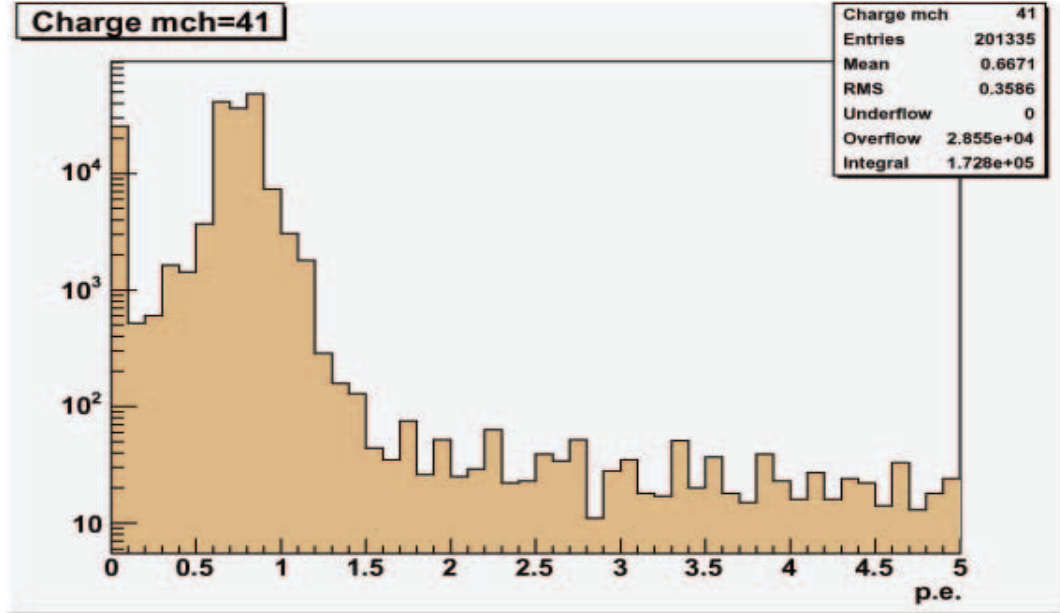


Figure 5.11: Reconstructed charge spectrum of dark noise run. 201.000 hits per 100.000 triggers

5.4.1 Motivation

Since the transit time of a PMT can differ from one another by several ns it is important to measure this time variable. The measured values are stored in a database to be later subtracted offline from the time responses of the PMTs to real events. This calibration procedure is similar to the one for the inner detector and is used to provide a calibrated time response pattern of all PMTs. Only by providing a reliable time calibration the goal, discussed in chapter 3 and 4, of having an accurate muon track reconstruction becomes feasible. Moreover a reliable knowledge of the charge of an individual PMT requires a calibration device which offers a high precision setting of the transmitted light (i.e. approximately one photon). This potential allows not to trust the linearity of the PMT response over a big range thus to have a feeling of the amount of photons it has seen but to measure and thus to know it.

5.4.2 The LED Electronic

As a first step the question for the right LED had to be risen. Since the transit time jitter of the Borexino PMTs is in the range of one ns and the jitter of the associated electronic is in the same range, the jitter of calibration LED should not exceed this range in order to provide a total jitter below 2 ns.

$$Jitter_{total} = \sqrt{Jitter_{PMT}^2 + Jitter_{electronic}^2 + Jitter_{LED}^2} \quad (5.4)$$

The Roithner Lasertechnik NSHU550 LED was found to have a very precise time response with a jitter below 0.8 ns and a total signal width of 8 ns. This offers both, a reliable time calibration and precise photon output. Moreover the LED gives out an ultra violet light signal in a narrow window around 370 nm which coincides perfectly with the maximum of the photocathode quantum efficiency.

A custom made electronic board was designed which meets the Borexino DAQ standards in order to facilitate controlling. The LED board shown in fig. 5.12 is powered by the standard VME power supply and is controlled by a PowerPC over the VME bus like most of the Borexino front end electronics.

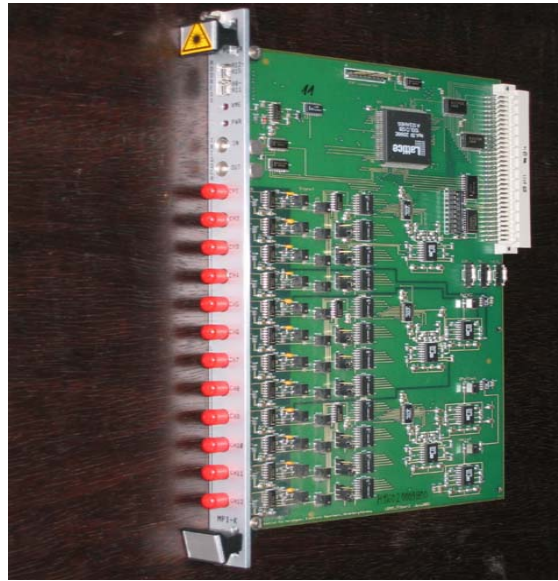


Figure 5.12: A LED board with 12 LED channels

5 Achievement of the Borexino Muon Veto

Eighteen calibration boards each comprising 12 LED channels were manufactured, tested and adopted in the muon veto electronic. The 12 channels on the board are divided in 3 identical groups of 4 channels. Every individual channel possess a 8 bit programmable delayline and a 12 bit programmable DAC. The pulse width and pulse height at the cathode of the LED is controlled by the DAC. In accordance with the set DAC value the board forms out of the positive edge of a trigger in signal a strait negative pulse at the cathode of the LED. By means of the delay line this pulse can be shifted in time up to 128 ns. This can be helpful in order to feed the system with simulated events and thus to study the response.

The signal of the LEDs is transmitted over an optical fiber to the PMTs. The LED crate with the connected optical fibers is shown in fig. 5.13.

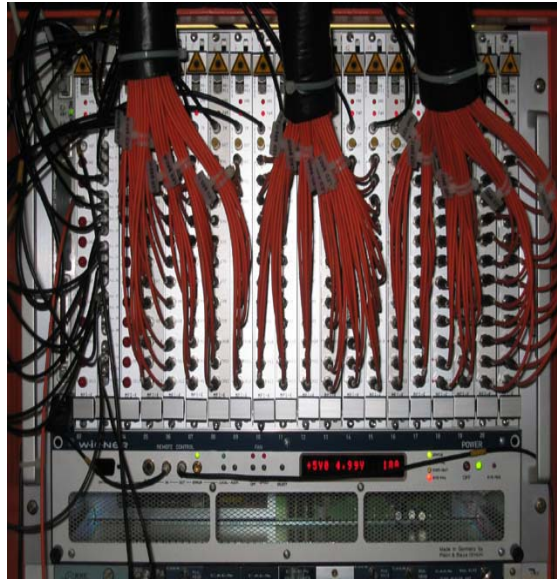


Figure 5.13: The LED crate with 208 connected optical fibers

5.4.3 The Control Software

The 12 LED boards are controlled by a software through the VME bus. This software is written in C and is a part of the Borexino online software. It is running on the PowerPC of the LED crate. The PowerPC is connected via TCP/IP to the Borexino DAQ cluster and is starting the LED software

5.4 The LED Calibration System

after every reboot. Subsequently it is waiting for commands through a socket connection. Since the boards do not comprise read access memory only basic commands are used for setting the right values to the LEDs. The values which are settable are:

- Voltage which controls the LED input voltage (from 0 to 4095)
- Delay which controls the delayline of the LED (from 0 to 255)
- "Setalldelays" which sets all delays of a board to a certain value (from 0 to 255)
- Enable trigger out (0 or 1)
- Internal trigger (0 or 1)

For supervising reason the set values are stored in an temporarily disposed array.

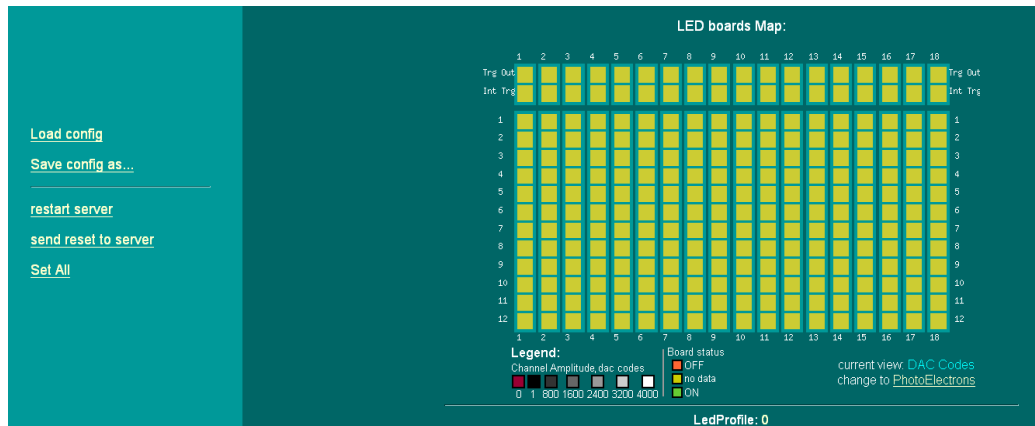


Figure 5.14: Visualisation of the 18 LED boards. Clicking on a square leads to the set channel window [SAB 05]

In order to allow the control of the calibration system also to a non practiced user a visualisation tool was developed which is shown in fig. 5.14 and 5.15. This tool communicates through a socket connection with the PowerPC and controls it by the commands of the LED software. fig. 5.14 shows the 18x12 LED channel perspicuously. The upper to rows belong to the enable trigger out and respectively to the internal trigger of the 12 boards. Clicking on a yellow square leads to fig. 5.15 where the values for voltage and delay are settable for an individual LED channel.

5 Achievement of the Borexino Muon Veto

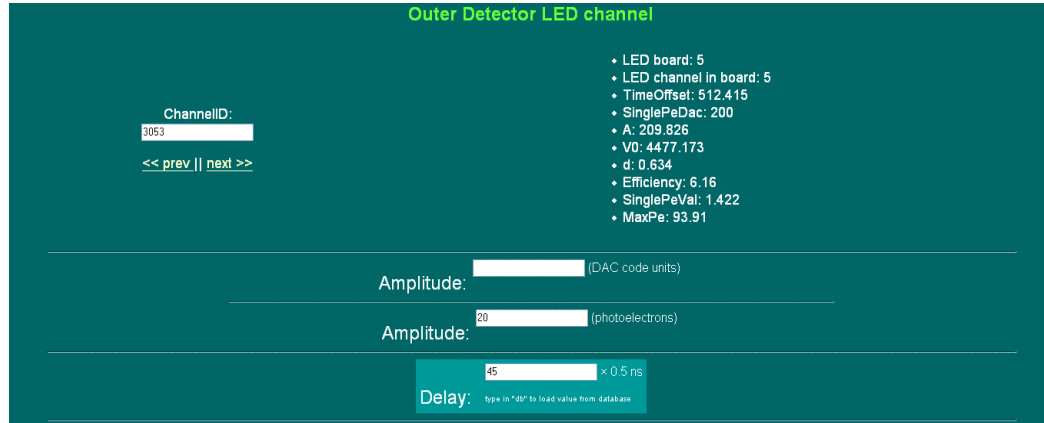


Figure 5.15: The window for setting LED intensity and delay of a channel [SAB 05]

For the calibration of the detector all LEDs are fired simultaneously in a single photoelectron mode. In order to guarantee an accurate single photoelectron response of the PMT the LED should transmit photons in a sub-Poisson statistic way (i.e. only few triggers, approximately 5% should generate photoelectrons). Every higher PMT response leads to a so called amplitude walk thus to an inaccurate time calibration. Subsequently the LEDs transmit a sequence of predefined numbers of photons in order to calibrate the charge response of the PMTs in a big range. All measured values are saved in a database which is disposed newly for every individual run and later on used for the reconstruction of the run.

5.5 The Installation of the Outer Detector



Figure 5.16: The proud muon veto installation crew inside the accomplished outer detector

During the design, preparation and testing of all the detector parts the impatience for completing the detector grew day by day. Nevertheless one of the most challenging tasks was the coordination of the installation job. Especially after the accident discussed in chapter two that delayed the completion of the detector the collaboration got pressed for time. Since the muon veto somehow "surrounds" the inner detector the completion of the main detector was inevitable for starting the installation of the outer detector. The need for parallelization arose which required sharp planning and fast troubleshooting.

5 Achievement of the Borexino Muon Veto

Thus parts of the outer detector had to be pre-installed and "sealed" for a later use.

5.5.1 Pre-installation

As a first step the high voltage cable had to be installed. The requirements for this cables are:

- profoundly water tight especially in the connector (bad experience in the CTF I revealed),
- all cables should have same length (55m) in order to avoid disparate arrival times of the PMT signals,
- good bending property in order to provide an easy installation,

Huber&Suhner Germany offered a cable which comprises all these requirements. 208 cables were installed through chimney like ducts which are on the top of the water tank above the intended water level. The outer parts of the cables were led through a cable tower into the counting room where they were connected to the high voltage decoupling stations.

Subsequently 208 optical fibers of the type Huber&Suhner H200/VJZ-D26 with 200 μm diameter were installed the same way. Since these fibers are very sensitive what concerns bending (i.e. it should be always assured that the bending radius is bigger than 15 cm) all fibers were first tested before being connected to the muon veto calibration system.

5.5.2 PMT Installation

The completion of the Borexino detector was stopped in August 2002 as a consequence of the accident mentioned in chapter two. After the access to Hall C was given free by the prosecutor the installation could continue. The inner vessel was mounted inside the SSS and subsequently the SSS door was closed. At that moment the outer detector could be accomplished. The first step was the mounting of the PMTs. All PMTs were fixed to the metal surfaces by 2 cm thick plastic holdings. First the PMTs are screwed to the holding shown in fig. 5.17. Subsequently the PMTs with the holdings are

5.5 The Installation of the Outer Detector

screwed to two stud welded bolts on the SSS and accordingly on the water tank surface.

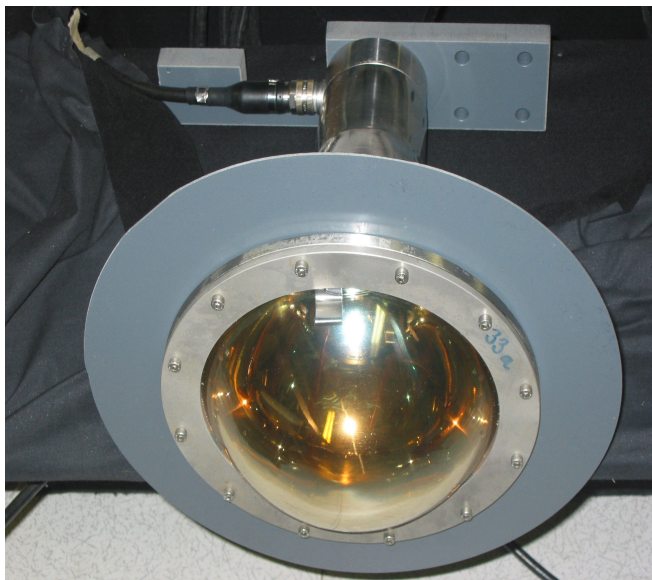


Figure 5.17: Encapsulated muon veto PMT with plastic holding

Since few installation jobs still had to be done during and after the muon veto completion the PMT installation was started on the north hemisphere. 104 PMTs were mounted in 6 rings accordingly to chapter 5.18. All PMTs were connected to the high voltage cables. For this installation the movable ladders could be used thus the job was simplified unlike the following installation on the southern hemisphere. Two traveling scaffoldings had to be used in order to reach the upper rings right below the equatorial grid in 8 meters height. 50 PMTs were installed in two rings on the lower hemisphere. At the end of the installation the remaining 54 PMTs were mounted on the water tank slope and on the floor. A precision measurement of the positioning of the PMTs was done. The result is illustrated in fig. 5.18.

5.5.3 Tyvek Installation

After having all PMTs in place the most challenging procedure was the mounting of the Tyvek. As discussed in chapter 4 the Borexino muon veto was enclosed by Tyvek sheets in order to raise the amount of photoelectrons per muon going through the outer detector.

5 Achievement of the Borexino Muon Veto

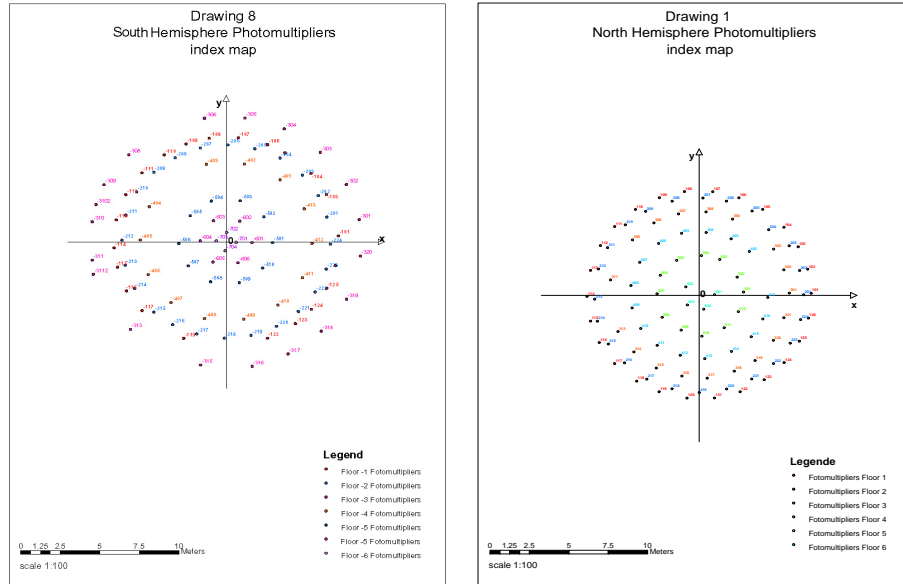


Figure 5.18: Two dimensional projection of the southern and northern hemisphere PMTs after the positioning

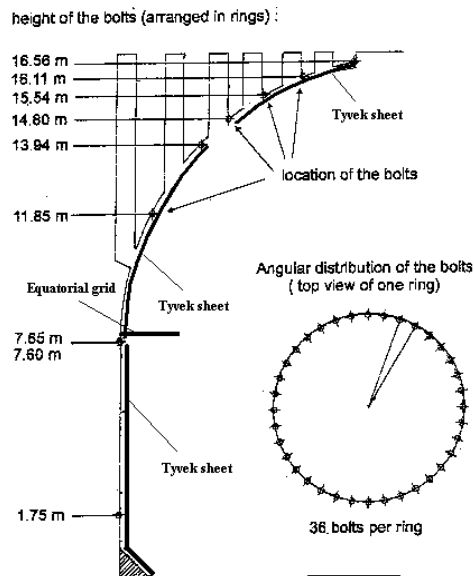


Figure 5.19: Side view of the water tank with tyvek sheets

5.5 The Installation of the Outer Detector

Enveloping of the SSS and of the water tank runs the risk to obscure the PET windows of the PMTs. It has not only to be proven that the reflectivity of Tyvek under water does not change in time but also that it's mechanical properties are not influenced by water. The Kamland muon veto uses the same method for raising the reflectivity and thus the photoelectron yield. Tyvek sheets are used there since several years without showing any aging effects. Nevertheless it was necessary to assure a reliable fixing and mounting of the approximately 120 Tyvek sheets. Bolts have been stud welded to the water tank wall in order to accept the Tyvek sheets in a reliable way. fig. 5.19 shows cross section of the water tank. The bolts are arranged circularly.

After having attached the first Tyvek sheet to the stud welded bolts the next sheets are mounted and fixed to each other by cable ties. This method assures greater closeness of the Tyvek ensemble. Unlike the lower water tank wall it was necessary to separate the northern wall in two Tyvek regions above and below the ladder carrying trail since otherwise the movable ladders would have been not longer movable.

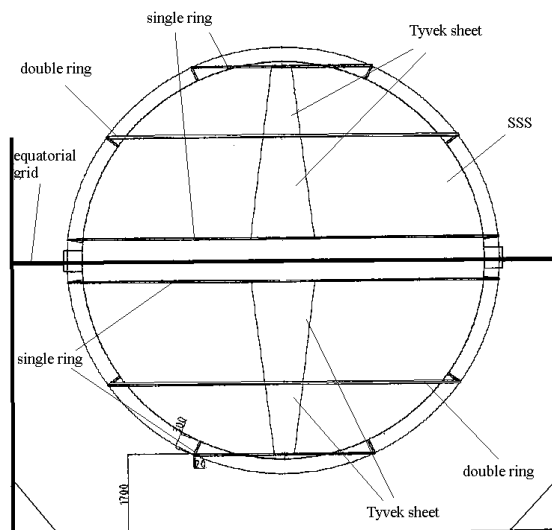


Figure 5.20: Front view of the SSS with the Tyvek rings

The Tyvek sheets on SSS, to which most of the PMTs were mounted, had to be attached by a different method. Fig. 5.20 shows the six stainless steel rings to which Tyvek sheets are fixed. Stainless steel "Z"-like devices were fixed to the PMTs on the first, third and sixth PMT rings in order to

5 Achievement of the Borexino Muon Veto

carry the Tyvek rings while stainless steel clamps and cable ties were used to fix the Tyvek to the Tyvek rings. After fixing the Tyvek sheets holes of the dimension of the PMT PET window were cut into them in order to disclose the PMT window. The Tyvek sheets are screwed to the PMTs by a white plastic ring as can be seen in fig. 5.21.

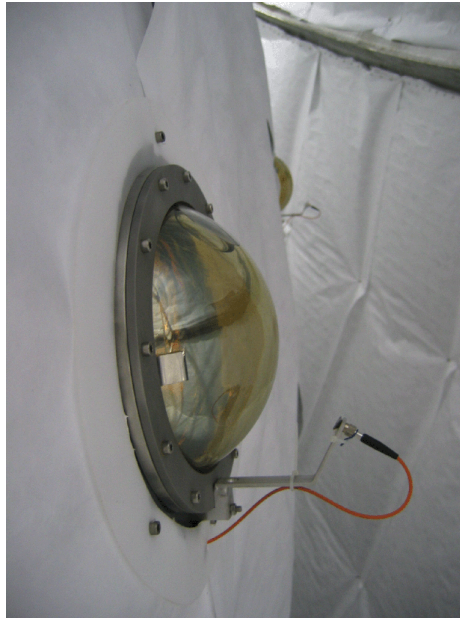


Figure 5.21: Encapsulated PMT with fiber holder after Tyvek installation

At the end of the Tyvek installation the optical fibers had to be connected to the PMT. The holder which can be seen in fig 5.21 assures that all light from the optical fiber reaches the photocathode. The stainless steel holder is screwed to the lowest edge of the encapsulation of the PMT thus it leaves only a negligible shadow on the photocathode. The fiber has on both ends smb female connectors. It is fixed to the holder by a screw with SMB thread.

Due to large cable bunches not all of the outer detector surface could be covered by Tyvek. Thus approximately 90% of the inner water tank and SSS surface was finally enclosed. The fig. 5.22 and fig. 5.23 show the northern and the southern part of the water tank respectively after the Tyvek installation. It is easy to recognize that the equatorial grid is not covered.

5.5 The Installation of the Outer Detector



Figure 5.22: View from the equatorial line to the northern part of the water tank after Tyvek installation



Figure 5.23: View from the floor of the water tank after Tyvek installation

5 Achievement of the Borexino Muon Veto

5.5.4 Monitor System

Although great efforts were done to assure a reliable and stable installation of all muon veto parts, in the course of operation time and especially during the water filling the unmeant detaching of detector parts can not be fully excluded. For instance could PMTs, obscured by detached or swimming Tyvek sheets, show an inexplainable signal. A look inside the detector by opening a flange would be excluded thus only a pre-installed monitor system could help clarifying and understanding the situation inside the detector. A monitoring system comprising 6 encapsulated standard digital cameras was designed, tested and adopted to the muon veto. Unlike the inner detector camera system which is thought mainly for calibration porposes the camera system of the outer detector has only a monitoring scope.

The digital cameras used are Canon Powershot G5 with a resolution of 5 Megapixel. For enlarging the field of vision all cameras use wide angle lenses. The encapsulation of the cameras comprises a stainless steel body with a glass window which are sealed by an annulate gasket and screwed together. An installed encapsulated camera is shown in fig. 5.24.



Figure 5.24: Side view of mounted camera encapsulation

The cameras are controlled by the standard software through the camera

5.5 The Installation of the Outer Detector

USB connection. Since the control software is running on a computer outside of the water tank (i.e. in a distance of approximately 50 meters) and USB connections can only be extended up to 10 meters the USB signal is transferred to ethernet and back. This method allows to send the signal over long distances up to 100 meters. The camera encapsulations are water tight connected by under water cables which contain the electrical power cables, the ethernet cables and a nitrogen connection. The nitrogen conduit was built in for the case that the encapsulation shows condensation of humidity when cool water is used for filling.

5.5.5 Test Run

The outer detector installation job was completed by a test run which demonstrated the operational state of the muon veto. All 208 PMTs were operated with high voltage on and the dark noise rate was measured. A calibration run was started to assure that all PMTs are connected through optical fibers to the LED calibration system.

The test has proven the reliability of the muon veto as a full system (i.e. PMTs, electronic, data acquisition, calibration system). Nevertheless it has also shown that too much light still enters the detector. Dark rates up to 100 kHz were measured even with almost all lights off in Hall C. Unfortunately these light conditions will definitely not change until the big water tank door is closed. Thus any meaningful measurements including the calibration of the PMTs is excluded.

5 Achievement of the Borexino Muon Veto

Chapter 6

Outlook

Future large liquid scintillator detectors can be seen as sequel to the Borexino and KamLAND experiments. However their great scientific potential could start a new era in neutrino physics, moving from a straight neutrino detector to a true observatory.

One of these experiments is the LENA (Low Energy Neutrino Astronomy) detector, which will be probably setup at the Center for Underground Physics in Pyhäsalmi (CUPP, Finland) at a depth of 1400 m (i.e. ~ 4060 mwe) [OBE 05]. The detector will consist of a large volume liquid scintillator with cylindrical shape, approximately 30m in diameter and 90m in length, equipped with a PMT coverage of about 30%. Fig. 6 gives a schematic view of the detector. The proposed scintillator is PXE which was investigated as an alternative scintillator in Borexino and features a high flash-point of 145° .

LENA would detect about 15,000 neutrinos and anti-neutrinos from a supernova at the center of our galaxy. The flavor specific neutrino/antineutrino detection reactions are:

$$\bar{\nu}_e + p \rightarrow e^+ + n (Q = 1.8 MeV) \quad (6.1)$$

$$\bar{\nu}_e + {}^{12}C \rightarrow e^+ + {}^{12}B (Q = 17.3 MeV) \quad (6.2)$$

$$\nu_e + {}^{12}C \rightarrow e^- + {}^{12}N (Q = 13.4 MeV) \quad (6.3)$$

6 Outlook

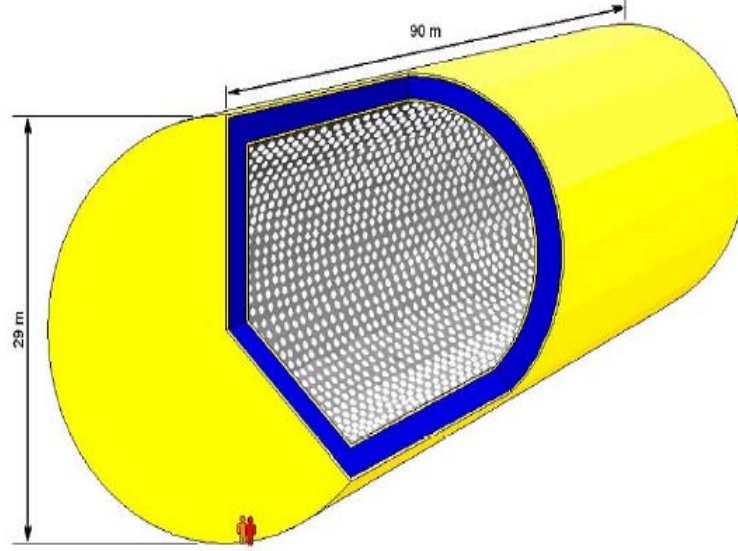


Figure 6.1: A schematic view of the LENA detector. It will use ≈ 60 kt liquid scintillator as target for neutrino detection. 12,000 PMTs provide a geometric coverage of $\approx 30\%$.

$$\nu_x + {}^{12}\text{C} \rightarrow {}^{12}\text{C}^* + \nu_x \text{ with } {}^{12}\text{C}^* \rightarrow {}^{12}\text{C}^+ \gamma (E_\gamma = 15.1 \text{ MeV}) \quad (6.4)$$

$$\nu_x + p \rightarrow \nu_x + p \quad (6.5)$$

The CC reactions (6.1) and (6.2) allow $\bar{\nu}_e$ -spectroscopy. Spectroscopy of ν_e s can be done with reaction (6.3). The NC reaction (6.4) and the elastic scattering reaction (6.5) will provide information about the total supernova ν -flux as all ν -flavors participate to this reaction.

A supernova in the center of our galaxy would leave detailed information in the LENA detector about the explosion mechanism due to time development of the specific ν -fluxes. Neutrino oscillations caused by matter effects as the supernova $\bar{\nu}_e$ cross the earth on their way to the detector would cause wiggles in the $\bar{\nu}_e$ energy spectrum. Observation of this spectral feature would give information about the neutrino oscillation parameters and the mass hierarchy.

Supernova relic neutrinos (SRN) are remnants of supernova explosions occurred during the star formation of the Universe. Measurement of the SRN-spectrum would provide valuable information on the star formation history in the Universe. The current best limit on SRN comes from the SuperKamiokande detector [SUP 03]. The sensitivity for the SRN reachable with the LENA detector should be drastically improved, as the delayed coincidence between the prompt positron and the captured neutron in the inverse beta reaction can be utilized.

Having a target which is about 200 times larger than the one of Borexino the rates of ${}^7\text{Be}$ -, pp-, pep- and CNO-neutrinos from the Sun are approximately 5400/day for ${}^7\text{Be} - \nu\text{s}$, 150/day for pep νs and 210/day for CNO- νs . From this measurement, together with the knowledge of the solar luminosity and ν -oscillation parameters, the fundamental pp-flux can be determined with an accuracy of better than 0.5% [BAH 03]. The high-statistic measurement of ${}^7\text{Be} - \nu\text{s}$ with LENA would allow researchers to test on temporal fluctuations of the solar density profile with high precision. Such temporal density fluctuations could be created by solar g-mode waves, which are not observed so far by helioseismology.

Furthermore LENA give a significant contribution to the study of proton decay. The decay mode $p \rightarrow K^+ \nu$, which is favored by SUSY models, water Cherenkov detectors are limited as the energy of the Kaon is below the Cherenkov threshold. In LENA this decay mode is visible in the following way.

The Kaon decay via $K^+ \rightarrow \mu^+ \nu_\mu$ with a branching of 63.5% can be tagged with a threefold delayed coincidence:

1. prompt mono-energetic K^+ (T=105 MeV)
2. short delayed ($\tau=12.8$ ns) mono-energetic μ^+ (T=152 MeV)
3. long delayed ($\tau=2.2$ ms) e^+ from the following μ^+ decay

The Kaon decay via $K^+ \rightarrow \pi^+ \pi_0$ with a branching of 21.2% can be tagged with a fourfold delayed coincidence:

1. prompt mono-energetic K^+ (T=105 MeV)
2. short delayed mono-energetic π^+ (T=108 MeV) accompanied by an electromagnetic shower due to the 2- γ decay of the π^0 (E=246 MeV)

6 Outlook

3. short delayed ($\tau=26$ ns) mono-energetic μ^+ with $T = 4$ MeV from the π^+ decay

4. long delayed ($\tau=2.2$ ms) e^+ from the μ^+ decay

For LENA the reachable sensitivity for the proton decay $p \rightarrow K^+ \nu$ could be close to a lifetime limit between 10^{34} and 10^{35} years after a measuring time of 10 years. The minimal SUSY SU(5) model predicts the decay mode to be dominant with a partial lifetime varying from 10^{29} to 10^{35} years [BAB 98]

Chapter 7

Conclusion

From Pauli's postulate to the results of the present neutrino experiments, the field of neutrino physics went through a rapidly rising gradient of understanding. The discoveries of the recent years not only reveal the properties of neutrinos, but also exert significant influence on the so called standard model, which forms the frame of our understanding of particle physics. Results of the solar neutrino experiment SNO show clearly flavor transitions from ν_e to $\nu_{\mu,\tau}$. The mysterious lack of solar neutrinos reported in several experiments is finally determined to be the result of neutrino oscillation. The final proof of this phenomenon was given by KamLAND, an experiment measuring anti-neutrinos emitted from nuclear reactors at large distances. In this context, the puzzle of the atmospheric anomaly discovered by the water Cherenkov experiments in the Kamioka mine, could also be explained by neutrino oscillation. The values for the oscillation parameters, amplitude and phase, have been restricted. Despite of the pathbreaking progress, the understanding of neutrino physics has by far not reached a point of complete satisfaction. Among the issues, which still need to be studied, the measurement of the low energy solar neutrino flux from ${}^7\text{Be}$ -, pp-, pep- and CNO-neutrinos is needed in order to confirm the LMA solution, since low energy neutrinos (≤ 2 MeV) do not undergo matter oscillations in the sun.

On the other hand low energy solar neutrinos could be used as probes of the thermonuclear reactions in the sun, thus of the theoretical predictions of the standard solar model. The measurement of the ${}^7\text{Be}$ -neutrino flux with a 10% precision will improve the current error on the ${}^7\text{Be}$ neutrino flux signif-

7 Conclusion

icant. Together with the solar luminosity constraint it will also improve the determination of the pp-neutrinos flux from the Gallium experiments, which have significant contributions both from the pp- and the ${}^7\text{Be}$ -neutrinos. The pp-neutrino flux will be determined experimentally with a precision below 1%, thus testing the 1% theoretical prediction of the SSM.

Borexino, an organic liquid scintillator detector is one of the experiments aimed at measuring in real time low energy (≤ 1 MeV) solar neutrinos, but is not limited at this. It's rich scientific program exceeds the measurement of solar neutrinos and ranges from the test of the LMA solution by means of reactor anti-neutrinos, to the detection of geophysical anti-neutrinos and to the measurement of supernova neutrinos. In order to reach this ambitious goals, high emphasis is set on the background reduction, especially of the noble-gases ${}^{85}\text{Kr}$, ${}^{39}\text{Ar}$, ${}^{222}\text{Rn}$ and the ${}^{210}\text{Pb}$ isotope from the ${}^{238}\text{U}$ -chain. A prototype CTF was setup in order to test detector components and several purification methods.

High energy muons are the remnants of the air showers produced in the atmosphere by collisions of high energy cosmic ray nuclei with air nuclei. Apart from neutrinos high energetic muons are the only particles, which reach deep underground experiments. In the Gran Sasso underground laboratory, at a depth of 3600 mwe, muons appear with a rate of $1.16/(m^2h)$ and an average energy of 320 GeV. About 10000 muons per day are passing the Borexino detector making it necessary to study fundamentally this cosmogenic background, particularly due to the fact, that the muon induced ${}^{11}\text{C}$ background rate in the detector target overlays the expected neutrino signal from pep- and CNO-neutrinos by far. The data of the CTFIII campaign has shown clear evidence of this background and allowed a prediction of the muon induced background rate in Borexino.

Driven by the goal of reducing the cosmogenic background significantly, a detector was designed, which uses the Borexino water shielding as an active Cherenkov detector. Simulations have proven the high efficiency of this outer detector concerning muon detection. An improved PMT positioning offers even additional information about the track of the muon, which passes through the detector. This information will allow to veto a cylindrical volume around the reconstructed track, which reduces the muon induced background down to a level where the detection of pep- and CNO-neutrinos is possible.

In order to setup a detector, which fulfills the muon detection requirements and furthermore works in a reliable and stable way, all hardware components were designed and setup appropriately. High attention was given to the PMT encapsulation, the PMT calibration and the electronics of the detector. Before reaching the goal of an accomplished detector, several steps were taken from testing of PMTs to planing the installation. In a final step the outer detector was installed and tested. The good test results and the constancy of the CTF muon veto gives great confidence in the reliability of the Borexino outer detector.

The new LENA project demonstrates the potentials of future large liquid scintillation detectors. It aims at using neutrinos as probes to address topics in astrophysics, cosmology, geophysics and particle physics. It could study solar, atmospheric and geo-neutrinos, supernova and supernova relic neutrinos as well as accelerator neutrinos. Moreover, it could be used to study proton decay.

7 Conclusion

Bibliography

- [AAL 02-1] C. E. Aalseth *et al.* [IGEX Collaboration], “The IGEX Ge-76 neutrinoless double-beta decay experiment: Prospects for next generation experiments”, Phys. Rev. D 65 (2002) 092007 [arXiv:hep-ex/0202026].
- [AAL 05] C. E. Aalseth *et al.* [Majorana Collaboration], “The proposed Majorana Ge-76 double-beta decay experiment,” Nucl. Phys. Proc. Suppl. **138**, 217 (2005).
- [ABD 99] J. N. Abdurashitov *et al.* [SAGE Collaboration], “Measurement of the solar neutrino capture rate with gallium metal”, Phys. Rev. C 60 (1999) 055801 [arXiv:astro-ph/9907113].
- [ABT 04] I. Abt *et al.*, “A new Ge-76 double beta decay experiment at LNGS”, arXiv:hep-ex/0404039.
- [AGL 99] M. Aglietta *et al.* [LVD Collaboration], “Measurement of the neutron flux produced by cosmic-ray muons with LVD at Gran Sasso,” arXiv:hep-ex/9905047.
- [AGU 01] A. Aguilar *et al.* [LSND Collaboration], “Evidence for neutrino oscillations from the observation of anti- ν_e appearance in a anti- ν_μ/μ beam”, Phys. Rev. D 64 (2001) 112007 [arXiv:hep-ex/0104049].
- [AHM 02] Q.R. Ahmad *et al.*, Phys. Rev. Lett. 87 (2001) 071301; 89 (2002) 011301; and 89 (2002) 011302.
- [ALI 02] Science and Technology of Borexino: A Real Time Detector for Low Energy Solar Neutrinos, G. Alimonti *et al.*, Borexino Collaboration, Astroparticle Physics 16 (2002) p.205

BIBLIOGRAPHY

- [ALL 96] W. W. M. Allison *et al.*, “Measurement of the atmospheric neutrino flavour composition in Soudan-2”, Phys. Lett. B 391 (1997) 491 [arXiv:hep-ex/9611007].
- [ALL 99] W. W. M. Allison *et al.* [Soudan-2 Collaboration], “The atmospheric neutrino flavor ratio from a 3.9 fiducial kiloton-year exposure of Soudan 2”, Phys. Lett. B 449 (1999) 137 [arXiv:hep-ex/9901024].
- [AMB 98] M. Ambrosio *et al.* [MACRO Collaboration], “Measurement of the atmospheric neutrino-induced upgoing muon flux using MACRO”, Phys. Lett. B 434 (1998) 451.
- [ANS 92] P. Anselmann *et al.* [GALLEX Collaboration], “Solar neutrinos observed by GALLEX at Gran Sasso”, Phys. Lett. B 285 (1992) 376.
- [ARA 05] H. M. Araujo, V. A. Kudryavtsev, N. J. C. Spooner and T. J. Sumner, “Muon-induced neutron production and detection with GEANT4 and FLUKA,” arXiv:hep-ex/0411026.
- [ARA 04] T. Araki *et al.* [KamLAND Collaboration], “Measurement of neutrino oscillation with KamLAND: Evidence of spectral distortion”, arXiv:hep-ex/0406035.
- [ATH 96] C. Athanassopoulos *et al.* [LSND Collaboration], “Evidence for anti- $\nu/\mu \rightarrow$ anti- ν/e oscillation from the LSND experiment at the Los Alamos Meson Physics Facility”, Phys. Rev. Lett. 77 (1996) 3082 [arXiv:nucl-ex/9605003].
- [ATH 97] C. Athanassopoulos *et al.* [LSND Collaboration], “Evidence for $\nu/\mu \rightarrow \nu/e$ neutrino oscillations from LSND”, Phys. Rev. Lett. 81 (1998) 1774 [arXiv:nucl-ex/9709006].
- [AUT 05] D. Autiero [OPERA Collaboration], “Status of the OPERA experiment (CNGS1),” Nucl. Phys. Proc. Suppl. **143** (2005) 257.
- [BAB 98] K.S. Babu, J.C. Pati, F. Wilczek, Phys. Lett. B 423 (1998) 337.
- [BAH 01] J. N. Bahcall, M. H. Pinsonneault and S. Basu, “Solar models: Current epoch and time dependences, neutrinos, and helioseismological properties”, Astrophys. J. 555 (2001) 990 [arXiv:astro-ph/0010346].

BIBLIOGRAPHY

- [BAH 03] J.N. Bahcall and C. Pena-Garay, JHEP 311 (2003), p. 0004 (hep-ph/0305159).
- [BAH 04] J.N. Bahcall, M.C. Gonzalez-Garcia and C. Pena-Garay, Solar neutrinos before and after Neutrino 2004, JHEP **0408**, 016 (2004), arXiv:hep-ph/0406294.
- [BAR 03] V. Barger, D. Marfatia, K. Whisnant, Int. J. Mod. Phys. E12, 569 (2003).
- [BAR 03-3] V. Barger, J. P. Kneller, H. S. Lee, D. Marfatia and G. Steigman, “Effective number of neutrinos and baryon asymmetry from BBN and WMAP”, Phys. Lett. B 566 (2003) 8 [arXiv:hep-ph/0305075].
- [BET 34] H.A. Bethe and R.E. Peierls, Nature 133, 532 (1934).
- [BOG 99] J. Boger *et al.* [SNO Collaboration], “The Sudbury Neutrino Observatory”, Nucl. Instrum. Meth. A **449** (2000) 172 [arXiv:nucl-ex/9910016].
- [BRI 05] S.J. Brice [MiniBooNE Collaboration], MiniBooNE, Nucl. Phys. Proc. Suppl. **143**, 115 (2005).
- [BRO 47] I. Broser, H. Kallmann, Z. f. Naturf. 2a, 439; 642 (1947)
- [BUE 05] A. Bueno [ICARUS Collaboration], “The ICARUS project,” Nucl. Phys. Proc. Suppl. **143** (2005) 262.
- [CAD 02] L. Cadonati, F. Calaprice and M. Chen, Astropart. Phys. 16 (2002), p. 361.
- [CHA 32] J. Chadwick, Nature 129, 312(1932); Proc. R. Soc. (Lond.) A 136, 692 (1932).
- [CHI 04] D. Chirkin and W. Rhode, Muon Monte Carlo: A high-precision tool for muon propagation through matter, arXiv:hep-ph/0407075.
- [CHO 98] M. Apollonio *et al.*, Chooz Collaboration, “Initial Results From The Chooz Long Baseline Reactor Neutrino Oscillation Experiment”, Phys. Lett. B420 397 (1998).
- [CHO 99] M. Apollonio *et al.*, Chooz Collaboration, “Limits on Neutrino Oscillations from the Chooz Experiment”, Phys. Lett. B466 415 (1999).

BIBLIOGRAPHY

- [CHO 00] M. Apollonio *et al.*, Chooz Collaboration, “Determination of neutrino incoming direction in the Chooz experiment and Supernova explosion location by scintillator detectors”, Phys. Rev. D61 012001 (2000).
- [CHO 03] M. Apollonio *et al.*, Chooz Collaboration, “Search for neutrino oscillations on a long base-line at the CHOOZ nuclear power station”, Phys. Eur. Phys. J. C27 331 (2003).
- [CLE 98] B.T. Cleveland *et al.*, Ap. J. 496 (1998) 505.
- [DAV 68] R. J. Davis, D. S. Harmer and K. C. Hoffman, “Search For Neutrinos From The Sun,” Phys. Rev. Lett. **20**, 1205 (1968).
- [DAV 96] R. Davis, Nucl. Phys. B (Proc. Suppl.) 48 (1996) 284.
- [DAN 05] Davide D Angelo, Background in Borexino, 2005.
- [FER 34] E. Fermi, Z. Phys. 88, 161 (1934), translated in F. L. Wilson, Am. J. Phys. 36, 1150 (1960).
- [FIO 05] E. Fiorini [CUORICINO Collaboration], “Results from CUORICINO and perspectives for CUORE,” Nucl. Phys. Proc. Suppl. **143**, 225 (2005).
- [FUK 96] Y. Fukuda *et al.* [Kamiokande Collaboration], “Solar neutrino data covering solar cycle 22”, Phys. Rev. Lett. 77 (1996) 1683.
- [FUK 02] S. Fukuda *et al.*, Phys. Rev. Lett. 86 (2001) 5651; and Phys. Lett. B539 (2002) 179.
- [GAI 90] T.K. Gaisser, “Cosmic Rays and Particle Physics”, Cambridge University Press, (1990)
- [GAV 89] V. N. Gavrin *et al.* [SAGE Collaboration], “The Baksan Gallium Solar Neutrino Experiment”, Nucl. Phys. Proc. Suppl. 16 (1990) 483.
- [GAV 03] V.N. Gavrin *et al.*, Nucl. Phys. B118 (2003) 39; and talk presented at the 8th Int. Conf. on Topics in Astroparticle and Underground Physics, Seattle, Sept. 2003.
- [GIN 64] The Origin of Cosmic Rays, V.L. Ginzburg and S.I. Syrovatskii, Pergamon Press 1964

BIBLIOGRAPHY

- [GOL 58] M. Goldhaber, L. Grodzins and A. W. Sunyar, “Helicity Of Neutrinos”, Phys. Rev. 109 (1958) 1015.
- [GON 04] M. C. Gonzalez-Garcia, Global analysis of neutrino data, arXiv:hep-ph/0410030.
- [GRI 04] C. Grieb, Future Neutrino Detectors and their Impact on Particle- and Astrophysics, 2004.
- [GUN 97] M. Gunther *et al.*, “Heidelberg - Moscow beta beta experiment with Ge-76: Full setup with five detectors,” Phys. Rev. D 55 (1997) 54.
- [Hae 95] H. Haensel. W. Neumann. Atome. Atomkerne. Elementarteilchen - Chapters 11-15, Spektrum Akademischer Verlag Heidelberg. Berlin. Oxford. 1995
- [HAG 00] T. Hagner *et al.*, Muon-induced production of radioactive isotopes in scintillation detectors, Astroparticle Physics 14 (2000) 33.
- [HAG 01] T. Hagner, Messung und Untersuchung zuzr Bestimmung des kosmogenen Untergrunds im solaren Neutrinoexperiment Borexino, 2001,
- [HAG 02] K. Hagiwara *et al.* [Particle Data Group Collaboration], “Review of particle physics”, Phys. Rev. D 66 (2002) 010001.
- [HAL 03] C. Hall [EXO Collaboration], “EXO: A Next generation double beta decay experiment,” SLAC-PUB-10826
- [HAM 96] W. Hampel *et al.* [GALLEX Collaboration], “GALLEX solar neutrino observations: Results for GALLEX III”, Phys. Lett. B 388 (1996) 384.
- [HAM 98] W. Hampel *et al.* [GALLEX Collaboration], “GALLEX solar neutrino observations: Results for GALLEX IV”, Phys. Lett. B 447 (1999) 127.
- [HAX 05] W. C. Haxton, P. D. Parker and C. E. Rolfs, “Solar hydrogen burning and neutrinos,” arXiv:nucl-th/0501020.
- [HIR 88] K. S. Hirata *et al.* [KAMIOKANDE-II Collaboration], “Experimental Study Of The Atmospheric Neutrino Flux”, Phys. Lett. B 205 (1988) 416.

BIBLIOGRAPHY

- [HIR 92] K. S. Hirata *et al.* [Kamiokande-II Collaboration], “Observation of a small atmospheric ν_μ/ν_e ratio in Kamiokande”, Phys. Lett. B 280 (1992) 146.
- [HOL 04] P.C. de Holand and A.Yu. Smirnov, Phys. Rev. D 69 (2004), p. 113002 (astro-ph/0307266).
- [KAR 02] W. Kretschmer [KARMEN Collaboration], “Neutrino physics with KARMEN,” Acta Phys. Polon. B **33**, 1775 (2002).
- [KEA 04] E. Kearns (Super-Kamiokande Collaboration), “Atmospheric neutrino results from SuperKamiokande, 2004.”, Neutrino 2004, 13-19 June 2004, Paris, France.
- [KIR 03] T. Kirsten et al., Nucl. Phys. B118 (2003) 33; E. Bellotti, talk presented at the 8th Int. Conf. on Topics in Astroparticle and Underground Physics, Seattle, Sept. 2003.
- [KLA 04] H. Klapdor-Kleingrothaus [HEIDELBERG-MOSCOW and GENIUS Collaborations], “First 10-kg of naked germanium detectors installed in liquid nitrogen in GENIUS Test-Facility in GRAN-SASSO,” Eur. Phys. J. C **33**, S962 (2004).
- [KOB 73] M. Kobayashi and T. Maskawa, Prog. Theor. Phys. 49, 652 (1973).
- [KOD 00] K. Kodama *et al.* [DONUT Collaboration], “Observation of tau-neutrino interactions”,
- [KOS 92] M. Koshiba, “Observational neutrino astrophysics”, Phys. Rept. 220 (1992) 229.
- [LAS 04] T. Lasserre, “Double-Chooz: A search for $\theta(13)$,” arXiv:hep-ex/0409060.
- [LEE 57] T. D. Lee and C. N. Yang, Phys. Rev. 105, 1671 (1957).
- [LEN 01] C. Lendvai, ” Photomultiplier-Einkapselung fr das Myon-Veto des Borexino-Experiments und Messung myoninduzierter Neutronen in der CTF II ”, 2001.

BIBLIOGRAPHY

- [LOB 01] V. M. Lobashev *et al.*, “Direct search for neutrino mass and anomaly in the tritium beta-spectrum: Status of ‘Troitsk neutrino mass’ experiment”, Nucl. Phys. Proc. Suppl. 91 (2001) 280.
- [LOB 02] V. M. Lobashev, “Study of the tritium beta-spectrum in experiment ‘Troitsk nu-mass’ ”, Prog. Part. Nucl. Phys. 48 (2002) 123.
- [NIE 05] L. Niedermeier, High efficiency purification of liquid scintillators for the solar neutrino experiment Borexino, 2005.
- [LUN 04] A. Formicola *et al.*, “Astrophysical S-factor of $^{14}\text{N}(p,g)^{15}\text{O}$,” Phys. Lett. B **591**, 61 (2004 [arXiv:nucl-ex/0312015]).
- [MAK 62] Z. Maki, M. Nakagawa and S. Sakata, “Remarks On The Unified Model Of Elementary Particles,” Prog. Theor. Phys. **28**, 870 (1962).
- [MIK 85] S.P. Mikheev and A.Yu. Smirnov, “Resonant amplification of neutrino oscillations in matter and spectroscopy of solar neutrinos”, Yad. Fiz. 42:1441-1448, (1985) [Sov.J. Nucl. Phys. 42:913-917, (1985).]
- [MIK 86] S.P. Mikheev and A.Yu. Smirnov, “Resonant amplification of neutrino oscillations in matter and solar neutrino spectroscopy”, Nuovo Cim. C9:17-26, 1986.
- [MIL 91] L. Miller [MACRO Collaboration], “Muon astronomy results from MACRO,”
- [MOR 03] S. Moriyama [XMASS Collaboration], “XMASS experiment,”
- [OBE 05] L. Oberauer, F. von Feilitzsch and W. Potzel, “A large liquid scintillator detector for low-energy neutrino astronomy,” Nucl. Phys. Proc. Suppl. **138**, 108 (2005).
- [OSI 01] A. Osipowicz *et al.* [KATRIN Collaboration], “KATRIN: A next generation tritium beta decay experiment with sub-eV sensitivity for the electron neutrino mass”, arXiv:hep-ex/0109033.
- [PAS 05] S.Pascoli, S.T.Petcov and T.Schwetz, The absolute neutrino mass scale, neutrino mass spectrum, Majorana CP-violation and neutrinoless double-beta decay, arXiv:hep-ph/0505226.

BIBLIOGRAPHY

- [PAU 30] W. Pauli, letter to Tübingen Conference, December 4, 1930, translated in L.M. Brown, Phys. Today 23, Sept. 1978.
- [PAU 78] W. Pauli, transl. in L. M. Brown, Phys. Today, Sept. 1978, 23.
- [PER 97] D. Perkins, "Gargamelle and the discovery of neutral currents", in the risk of the Standard Model
- [PER 75] M. Perl et al., Phys Rev. Lett. 35, 1489 (1975) Phys. Lett. B 504 (2001) 218 [arXiv:hep-ex/0012035].
- [PIE 01] A. Piepke [KamLAND Collaboration], "KamLAND: A reactor neutrino experiment testing the solar neutrino anomaly", Nucl. Phys. Proc. Suppl. 91 (2001) 99.
- [PON 68] B. Pontecorvo, "Neutrino experiments and the question of leptonic-charge conservation", Sov. Phys. JETP 26 (1968), 984.
- [REI 57] F. Reines and C. L. Cowan, "Neutrino Physics", Phys. Today 10N8 (1957) 12.
- [REI 60] F. Reines, C. L. Cowan, F. B. Harrison, A. D. McGuire and H. W. Kruse, "Detection Of The Free Anti-Neutrino", Phys. Rev. 117 (1960) 159.
- [REI 95] F. Reines, "The Neutrino: From Poltergeist to Particle", Nobel Lectures, Physics 1991-1995, World Scientific Publishing Co., Singapore, 1997
- [SAA 04] R. Saakian [MINOS Collaboration], "Status and prospects of the MINOS experiment," Phys. Atom. Nucl. **67**, 1084 (2004) [Yad. Fiz. **67**, 1112 (2004)].
- [SAB 05] A. Sabelnikov, private communications during 2000 and 2005.
- [SCH 89] M. Schwartz, Rev. Mod. Phys. 61, 527 (1989)
- [SMI 04] A. Y. Smirnov, "The MSW effect and matter effects in neutrino oscillations," arXiv:hep-ph/0412391.
- [SUP 03] SuperKamiokande Coll., Phys. Rev. Lett. 90 (2003), p. 061101.

BIBLIOGRAPHY

- [VOG 89] P.Vogel and J.Engel, Neutrino Electromagnetic Form-Factors, Phys. Rev. D **39**, 3378 (1989).
- [WEI 02] C. Weinheimer, “Direct neutrino mass search”, arXiv:hep-ex/0210050.
- [WOL 78] L. Wolfenstein, “Neutrino Oscillations in Matter”, Phys. Rev. D **17** (1978) 2369.
- [WON 04] H.T.Wong, Neutrino magnetic moments: Status and prospects, Nucl. Phys. Proc. Suppl. **143**, 205 (2005), arXiv:hep-ex/0409003.

Acknowledgment

Als erstes möchte ich mich bei meinem Doktorvater Franz v. Feilitzsch für die Möglichkeit auf diesem interessanten Gebiet der Physik tätig zu werden bedanken. Sie waren für mich immer ein geduldiger und interessierter Zuhörer für sämtliche Probleme verbunden mit meiner Arbeit. Die Erfahrung, die ich an diesem Lehrstuhl sammeln konnte, haben meine Erwartungen übertroffen und werden das Gerüst meiner zukünftigen Laufbahn sein.

Lothar Oberauer möchte ich für das immense Vertrauen, dass er mir immer entgegengebracht hat danken. Die Zusammenarbeit hat sich im Laufe der Jahre zu einer freundschaftlichen Arbeitsatmosphäre erweitert. Nicht mehr jemanden zu haben, auf dem man sich hundertprozentig verlassen kann, wird wohl die grösste Hürde sein, die ich jetzt nehmen muss.

Caren Hagner möchte ich danken, dass sie mir immer geholfen hat, wenn ich mal wieder in letzter Minute etwas gebraucht habe.

Marianne Goeger möchte ich danken, dass sie mir bei vielen anstehenden Arbeiten geholfen hat. Ich hoffe, meine ständige Neugierde bezüglich des Nachwuchses hat sie nicht zur Verzweiflung getrieben.

Meinen Kollegen Davide d'Angelo, Christian Grieb, Jean-Come Lanfranchi und Ludwig Niedermeier möchte ich danken, dass sie mir gezeigt haben, wie wertvoll es ist Freunde zu haben, die immer für einen da sind.

Den Institutssekretärinnen Beatrice van Bellen und Alexandra Földner für ihre aussergewöhnliche Bereitschaft mir aus jeder Notlage zu helfen, was bei mir an der Tagesordnung war.

Den Mitarbeitern in unserer Werkstatt, Harald Hess, Erich Seitz und Thomas Richter für ihre äusserst kompetente technische Unterstützung.

Allen anderen Kollegen von E15 für die freundliche Arbeitsatmosphäre.

Thanks a lot Andrew, George, Laszlo and Yura for having you as friends around me. We had always great time together. I hope this will never end.

Ein besonderer Dank geht an meine Frau Nicole, die sehr viel Geduld mit mir hat und mich immer unterstützt.